



SAPIENZA
UNIVERSITÀ DI ROMA

Self Injection of High Brightness electron beams via Wakefield Ionization in beam-driven Plasma Acceleration

PhD course in Accelerator Physics

Dottorato di Ricerca in Fisica degli Acceleratori – XXX Ciclo

Candidate

Francesco Mira

ID number 1194309

Thesis Advisor

Prof. Stefano Atzeni

Co-Advisor

Dr. Alberto Marocchino

A thesis submitted in partial fulfillment of the requirements
for the degree of Doctor of Philosophy in Physics

October 2017

Thesis not yet defended

Self Injection of High Brightness electron beams via Wakefield Ionization in beam-driven Plasma Acceleration

Ph.D. thesis. Sapienza – University of Rome

© 2017 Francesco Mira. All rights reserved

This thesis has been typeset by L^AT_EX and the Sapthesis class.

Author's email: francesco.mira@uniroma1.it

*Dedicated to
my brothers*

Abstract

Plasma acceleration is a promising accelerating technique for delivering high brightness, GeV energies beams with table-top size devices. Theoretical works, simulations and experiments have demonstrated the possibility to inject and accelerate electron bunches in a plasma wave, driven either by a laser or a relativistic charged beam. However, the beam properties, such as emittance and energy spread, are still poor with respect to RF accelerators. Novel schemes or approaches have to be foreseen to retain bunch quality over the whole acceleration length.

A possible approach to retain the accelerated bunch quality is to use the *external-injection* technique. The external injection employs a conventional photoinjector technology to extract the electron bunch from a photo-injector and pre-accelerate it, while the plasma is used as an extremely high gradient section. The power of this approach is based on the great reliability that photoinjector technology has reached. Besides, the requirement of a pre-accelerating structure determines a partial loss in terms of compactness. Conversely, *internal-injection* techniques relies on the trapping of electrons from the plasma background in the accelerating and focusing phase of the plasma wave. The pre-accelerating structure is no longer required, but the characteristics of internally-injected electron beams strongly and non-linearly depend on both the driver (Laser, electron, or positron beam) and the plasma wake properties.

Several schemes have been proposed (magnetically assisted injection, density transition injection, ionization injection) to reduce the number of independent variables and therefore to improve the control on the internally-injected beam quality. In the approach called beam driven Wake-Field Ionization Injection the choice of a dopant element with high ionization potential, confined in a small region of a pre-ionized

background plasma, removes the direct driver contribute. Nevertheless, the driver space charge must be intense enough to expel the plasma electrons from its wake, determining the so called *blowout regime*. The high ionization potential of the dopant gas ensures that it does not get ionized by the radial field of the driver, but only by the much more intense (~ 10 times) fields in the wake; besides, the freed electrons are trapped in the accelerating and focusing phase of the plasma wave, yielding high brightness electron beams.

In this thesis I studied how the blowout regime characteristics affect the internally-injected beam quality. A volume inside the blowout region was defined where both ionization and trapping of freed electrons occur, and it was discussed how it is related to the blowout regime characteristics (blowout geometry, electric field magnitude) and to the nature of the dopant element. I will refer to this volume with the name *injection volume*. The ionization-injected electron dynamics in a non-evolving plasma wakefield was divided in two main timescales: a fast transient between the ionization and the trapping process, and a steady state condition, corresponding to the trapped electron co-propagating at the velocity of the plasma wave. The transient was studied via a particle tracking code I have developed: it employs the electromagnetic fields obtained via PIC simulations and treats the moving electrons as test particles. In the space-charge-force-free regime I have investigated, it was determined how the geometry of the injection volume influences the dynamics of a representative group of ionization-injected electrons. The beam length, spot size, mean energy, emittance and energy spread were defined and compared the results to a series of PIC simulations, performed with the full 3D PIC code ALaDyn.

In these simulations, the effect of the dopant gas density distribution and volume was studied for a few hundreds of micron propagation distances, for a single driver beam set of characteristics (10 kA, 1 GeV, resonant length). The driver beam properties

were chosen to obtain low emittance, low energy spread, and high current self-injected beams able to drive a new generation light source. The results were compared in terms of injected charge, beam emittance and energy spread for different dopant elements: pre-ionized Nitrogen, pre-ionized Argon, ground state and pre-ionized Neon. Similar results were obtained for these set of dopant elements, with a slightly better case for the pre-ionized Nitrogen, since the injection volumes, the geometry of which essentially depends on the ionization potential, for the three choices was found to be very similar. Finally, I compared the results for pre-ionized Neon and ground state Neon, which instead present completely different injection volumes: the higher ionization potential of the pre-ionized Neon determines a smaller injection volume than the ground state Neon. As a consequence, the injected beam charge, spot size and duration are smaller than the ground state Neon case, but both the energy spread, and the beam emittance were found to be comparable, possibly due to nonlinear effects such as beam loading.

Ringraziamenti

Dodo, Pippo, Tommi

Mamma, Papà

Bob, Fabio, Teo

Frank, Alberto, Pasquale

Familia

Patati

Ale & Fabrizio

SPARC_LAB

The Zoo

Prof. Atzeni

...

...

...

grazie.

Contents

1	Introduction	1
2	Plasma acceleration: an introduction	11
2.1	The Vlasov Equation	11
2.2	The cold fluid approximation	14
2.2.1	Linear regime	19
2.2.2	Breakdown of the linear regime	25
2.2.3	Non-linear regime	29
2.3	Wave breaking and particle trapping	42
3	Numerical tools	49
3.1	Numerical Plasma and Particle In Cell method	49
3.1.1	Particle-grid connection	53
3.1.2	FDTD Yee module in PIC numerical integration	58
3.1.3	PIC numerical integration of particle and field equation	60
3.2	The ALaDyn Code	65
4	Electron trapping via ionization	67
4.1	Wake-Field Ionization Injection	67
4.1.1	Ionization model	69

4.1.2	Ionization injection trapping condition	73
4.1.3	Dynamics of wake-field ionized electrons	77
4.2	Chapter 4 Summary	85
5	Beam properties analysis	87
5.1	Self-injected Beam characteristics	87
5.1.1	Beam spot size and emittance	88
5.1.2	Beam length and energy spread	92
5.1.3	Beam Charge	96
5.2	Numerical experiment layout	97
5.3	Simulation results	100
5.4	Chapter 5 Summary	107
6	Conclusion	109
A	Linear regime full derivation	115
B	Wave breaking and trajectory crossing	125
C	Boris pusher algorithm	133
D	Anisotropic wave propagation mitigation for FDTD-Yee lattice	137

Chapter 1

Introduction

More than one hundred years have passed, since for the first time an instrument able to accelerate charged particle was used to investigate the properties of the matter. In 1897, J. J. Thomson discovered the electron by studying the deflection in a magnetic field of a beam accelerated by an electrostatic potential between two electrodes.

Accelerators have since become an indispensable tool to investigate nature at smaller and smaller scales: although they have become bigger and much more complex, we could roughly say that they still operate with the same principle used in Thomson's device, i.e. an electric field accelerating charged particles.

Accelerator technology is nowadays widely used in different areas of applied physics. The synchrotron radiation facilities provide the high brilliance and coherent light necessary to investigate phenomena on the time-scale of the picoseconds, and the future X-rays Free Electron Laser laboratories will improve the output up to the time-scale of the femtosecond and beyond.

The Paul Scherrer Institute in Switzerland, the CNAO in Italy, the GSI in Germany and others all over the world, are facilities in which hadron accelerators are used to treat hardly removable tumours of thousands of patients per year. Besides, X-rays machines are used in radiotherapy and radiology instead of long life radionuclides.

The Accelerator Driven Sub-critical (ADS) reactor is one other promising potential uses of particle accelerator providing spallation neutrons to both sustain the nuclear fission processes in power plants and to transmute long life radionuclides in less dangerous isotopes. Finally, particle accelerators are also used to implant ions in semiconductor materials, to sterilize air, food, and other commercial products and as a security tool to characterize nuclear waste.

In considering the evolution of accelerator and collider technology for particle physics, we usually think first of the available energy such tools provide. Even if it is not the only variable of remarkable importance, the requirement of higher and higher beam energy has mainly influenced the development of accelerators.

The maximum energy ever achieved was detected at the Large Hardon Collider at CERN for the ATLAS and CNS experiments, to detect the mass of Higgs boson and to compare it with the theoretical value of $120 \text{ MeV} < m < 200 \text{ MeV}$. Two proton beams were made to collide and an energy of 8 TeV was reached in the reference frame of the centre of mass.

Further enhancements of the performances for this generation of particle accelerators, seem however infeasible: the rupture of the accelerating device structure (radio-frequency copper or super-conductive alloy cavities) as the electric field reaches the so called *breakdown limit*, limits the maximum achievable accelerating gradient to values about tens of MV/m.

The solution to the accelerating field limit has never been achieved, and the construction of larger and larger facilities could only partially solve the above-mentioned problem. Two questions could therefore spontaneously arise: how big can accelerators become, either for electrons and positrons, or for protons, and how expansive? Is there any other possibility to reach better performances, in terms of accelerating gradients and energies, rather than by building larger structures? The first answer

is depicted in the next Tabs 1.1 1.2 (from [1] [2] [3] [4] [5]), where we report performances, dimensions and cost either of the existing facilities and the future designs (the Superconductive Super Collider-SSC project was abandoned in the early nineties due to its excessive cost):

The second answer could be: we are working on it. Considerable interest has been

Table 1.1. Current technology RF accelerators and future developments

	Centre of mass Energy	Dimensions	Accelerated particles
SLAC	~ 50 GeV	~ 3 km	leptons
LHC	~ 8 TeV	~ 27 km	hadrons
CLIC	~ 3 TeV	~ 50 km	leptons
ILC	~ 200 GeV	~ 22 km	leptons
SSC	~ 20 TeV	~ 90 km	hadrons

Table 1.2. Current technology RF accelerators and future developments

	Accelerating Gradient	Costs	Current state
SLAC	40 MV/m	~ 10^8 dollars	upgrading
LHC	~ 10 MV/m	~ $5 \cdot 10^9$ dollars	upgrading
CLIC	100 MV/m	~ 50 GCHF	project
ILC	31.5 MV/m	~ $20 \cdot 10^9$ dollars	project
SSC	~ 6 MV/m	> 10^{10} dollars	abandoned

indeed shown in the past decades in new accelerating technologies, to enhance the performances and to overcome the breakdown limit of the conventional accelerators, therefore reducing the size and the cost of the structures that high energy beams require. Among the developing technologies, the one which employs a plasma as an accelerating system, is of great interest.

In plasma acceleration, a high-power source determines the displacement of the electrons of a ionized gas, while the heavier ions approximately stay still in the timescale of electron motion. The space charge field developed draws back the electrons, that start to oscillate with a characteristic frequency, depending to the plasma density.

A very high both focusing and accelerating electric field develops behind the power source, in a way roughly similar to a wake in the sea developed behind a boat (a very frequent analogy used to picture plasma acceleration): this high intensity wake-field is therefore used to focus and accelerate an electron bunch coming from the plasma itself (*internal injection* scheme) or from the outside (*external injection* scheme), previously accelerated by a conventional accelerator structure (Fig. (1.1)).

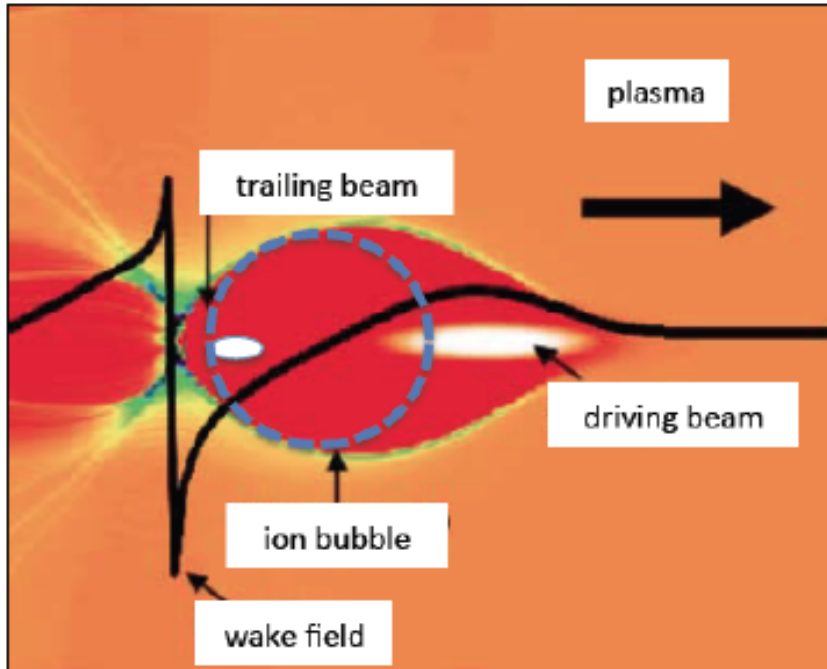


Figure 1.1. Schematic representation of the longitudinal wake field (black line) and ion distribution (red area) behind a driving laser or particle beam

A plasma can sustain electric fields of extremely high magnitude: it is indeed a highly

ionized gas and therefore is not affected by metallic cavities structural breakdown issues. One might even say that is the breaking of plasma equilibrium structure itself that seeds the electric field.

The only limit with respect to high achievable gradients is given by the maximum electron density that can be perturbed: if we suppose to completely deplete the perturbed region, determining the so called *blowout regime*, the electric field might reach the value given by the expression of the so called *Dawson Limit* [6], or *1D Wave-breaking Limit*:

$$E_{max}[\text{V/cm}] = \frac{mc\omega_p}{e} \cong 0.96\sqrt{n_0[\text{cm}^{-3}]} \quad (1.1)$$

where $\omega_p = \sqrt{n_{e,0}e^2/m_e\varepsilon_0}$ is the so called *plasma frequency*, related to the unperturbed electron density $n_{e,0}$ and the electron charge e and mass m_e .

Therefore, for typical plasma acceleration density values of $\sim 10^{16} - 10^{18}\text{cm}^{-3}$, the electric field reaches $\sim 10 - 100 \text{ GV/m}$, a value three order of magnitude higher than the maximum intensities achievable in RF accelerating structures (25 MV/m at DESY [7], 40 MV/m at SLAC [1]).

Although plasma accelerators are referred to be a new generation of particle accelerators, the related research field has no recent beginning. Two different areas of research historically developed, differing in terms of the high-power source choice. The so called *Laser Wake – Field Acceleration* is based on the excitation of the electron background by a very intense laser pulse, and the *Plasma Wake – Field Acceleration*, which employs an ultra-relativistic electron bunch as high-power source. First rigorously studied by Tajima and Dawson in the seventies [8], plasma acceleration has been proved until nowadays for both the branches. While in 1985 Clayton et al. measured the laser beat-wave (two laser pulses of close frequencies

instead of only one to enhance the intensity) excitation of GV/m unloaded relativistic plasma wave [9], in 1988 Rosenzweig experimentally proved interactions between a 21 MeV driving electron beam and the 5 MV/m Wake-Field [10].

As lasers became more powerful in the early 2000s reaching multi TW level, it became possible to excite plasma waves in high accelerating regime by using a single short pulse: Leemans et al. in 2006 reported an output energy increase of 1 GeV in a cm-scale capillary plasma [11].

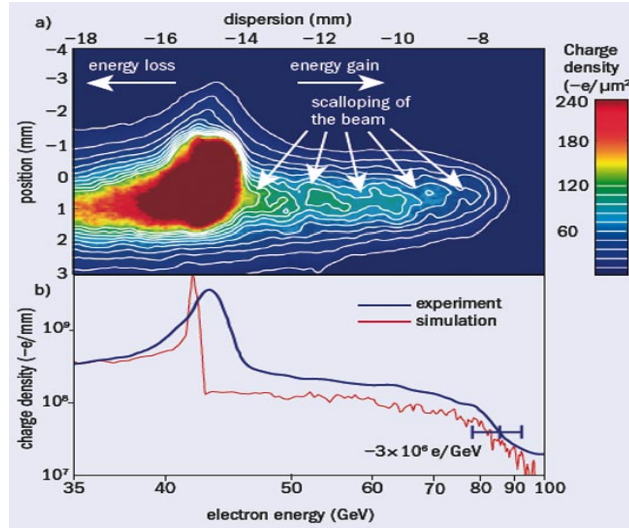


Figure 1.2. **a**, Energy spectrum of the electrons in the 35/100 GeV range. **b**, Projection of the image in **a** shown in blue. The simulated energy spectrum is shown in red. Image from [12]

This last record-breaking result for laser-driven accelerators also brought forth the main issue with these schemes, i.e. the fact that laser pulses do not propagate focused over long distances due to diffraction. It is still nowadays challenging to extend these acceleration techniques to the meter-scale, or even several cm-s, plasmas that are required for light source or high energy physics experiments. For these length scales the beam-driven scheme does not suffer from diffraction, since a relativistic

electron beam is ‘stiffer’ and propagates without evidently modifying its structure for many betatron wavelengths.

Such scheme development brought in 2007 to the experiment at SLAC where Blumenfeld et al. measured a doubling in the energy of a 42 GeV electron bunch in a meter scale plasma [12]. On the other hand, the experiment results also proved the main problem experienced so far with plasma acceleration, i.e. a beam quality still not comparable with the one produced by conventional accelerator (Fig(1.2)).

The studies performed for this thesis focus indeed on this very aspect: to develop a few cm-s plasma device able to provide high brightness electron beams matching the requirements of new generation light sources. We chose a beam driven scheme since around the cm length-scale it ensures higher stability than a laser driven one. The regime we have investigated is the blowout regime, which is characterized by features allowing both to accelerate to GeV energies in the cm length and to provide beam quality preserving transport along the accelerating structure. Given the high sensitivity of the scheme to beam positioning in the accelerating phase of the plasma wave, and thus the extreme precision (< fs synchronization) required for external injection, we decided to rely on a internal-injection scheme which employs the ionization of a high Z element mixed with a hydrogen plasma, provided by the wake-fields themselves. As we will present later in details, this ionization-injection scheme provides inherently low emittance, high energy, and high current internally-injected beams.

The thesis is organized in two introductory chapters, where is presented a review of the PWFA physics and the numerical methods employed to study it, and two final chapters where we show and discuss our original work. In more details:

- in Chapter 2 we will show some analytical approaches to plasma acceleration theory. We will give a brief description of what a plasma is and why we need

to introduce and to study the evolution of the distribution function in the 6D phase space. The Vlasov Equation and its moments will be introduced, and the so called cold fluid model will be presented. A linear 3D model coupling the cold fluid description of a plasma and the Maxwell equations will be derived, and we will show both the advantages and limits of considering a plasma as a linear continuum medium at equilibrium conditions. The breakdown of this approximation is therefore introduced, and an analytical simplified model developed to reproduce some of the features of the non-linear regime will be discussed. We will discuss how it is possible to bypass the external injection via the process called *self-injection*, where background plasma electrons having longitudinal velocity higher than the phase velocity of the plasma wave get trapped and are strongly and efficiently accelerated by the plasma wake-field. This phenomenon employs the breaking of the plasma wave, and we will show some of its characteristics;

- in Chapter 3 we will summarize the main algorithms and the overall computational structure of the Particle In Cell codes. To date, numerical investigations of plasma based accelerators heavily relies on Particle in Cell (PIC) method, which can be considered the-state-of-the-art in the field. Other approaches, like a direct integration of Eulerian-Vlasov equation in six-dimensional phase space requires huge amounts of computational resources, well outside present computer capabilities. Reduced approaches, like cold fluid approximations, can be considered auxiliary tools to be used only in specific conditions or as ingredient of hybrid schemes, where essential physical aspects like electron beam propagation, ionization and bunch acceleration in wake-fields have necessarily to be computed using direct fully kinetic PIC schemes, anyway. Finally, we will summarize the features of the PIC code ALaDyn, which has widely used

in the present thesis;

- in Chapter 4 we will present and discuss a scheme that has been proposed to provide self-injection in a beam driven wake-field, via trapping of ionized electrons stripped from a high Z layer directly in the bubble volume. Such scheme is called Wake-Field Ionization Injection. A qualitative analysis is also presented, performed via a Particle Tracker code we have developed, to understand the dynamics of the self-injected electrons and to relate it to the beam properties;
- in Chapter 5 we will present and discuss the results we have obtained in the characterization of the Wake-Field Ionization Injection scheme. We performed our analysis via numerical simulations using the PIC Code ALaDyn and compared the results to the theory and the qualitative studies performed with the particle tracker to relate the self-injected beam properties to the blowout and ionization characteristics.

We will present the numerical experiment set-up we have employed, in order to reduce at minimum the beam quality degradation both along the injection and the transport processes. Finally, we will show the results of the simulations using different dopant gases (Ar, N, Ne) as active ionization elements, comparing the self-injected beam properties and their evolution over the injection distance.

Chapter 2

Plasma acceleration: an introduction

2.1 The Vlasov Equation

A plasma is a collection of N_s charged particles, with species (*electron, ion*), $s = (e, i)$, particle charges $q_s = [-e, Ze]$ and particle masses $m_s = [m_e, Am_p]$, where (Z, A) indicate the ion charge and atomic mass numbers, respectively, which interact each other via electromagnetic forces [15][16]. For typical laboratory conditions, the plasma density we are dealing with is in a range $[10^{15} - 10^{20}] \text{ cm}^{-3}$, and at a first sight it seems really infeasible to follow the dynamics of every single particle, since the computational cost of solving the equations of motion for N particles scales roughly as N^2 .

We accept therefore to lose some information about the single particle dynamics via following the evolution of a particle sampling instead [16], that is the average number of particles in an infinitesimally small volume in the phase space $d\mathbf{r}d\mathbf{p}$, named the *distribution function* $f(\mathbf{r}, \mathbf{p}, t)$:

$$N(t) = \int_{V_{6D}} f(\mathbf{r}, \mathbf{p}, t) d\mathbf{r} d\mathbf{p}, \quad (2.1)$$

where V_{6D} is the phase space volume and $N(t)$ the number of particles in V_{6D} , in the limit $N_s \rightarrow \infty$ in such a way the total charge Q_s , mass M_s and charge to mass ratio Q_s/M_s remain finite, the same as in a real plasma, and we can consider $f(\mathbf{r}, \mathbf{p}, t)$ as a continuous function.

Assuming that the number of particles in the 6D volume is conserved, we write the total derivative of f as:

$$\frac{D}{Dt} f(\mathbf{r}, \mathbf{p}, t) = \frac{\partial}{\partial t} f(\mathbf{r}, \mathbf{p}, t) + \nabla \left(\frac{\partial \mathbf{r}}{\partial t} \cdot f(\mathbf{r}, \mathbf{p}, t) \right) + \nabla_{\mathbf{p}} \left(\frac{\partial \mathbf{p}}{\partial t} \cdot f(\mathbf{r}, \mathbf{p}, t) \right) = 0, \quad (2.2)$$

where $\nabla_{\mathbf{p}}$ is the vector of partial derivatives with respect of the components of the momentum (p_x, p_y, p_z) and $\partial \mathbf{p}/\partial t = \mathbf{F}$ represents the resulting force acting on the particles. In the case of charged particles in a plasma, the acceleration is produced solely via the Lorentz force (collisions are neglected in low density plasmas studied for particle acceleration). We obtain the so called relativistic *Vlasov Equation* (V.E.) [13]:

$$\frac{\partial}{\partial t} f(\mathbf{r}, \mathbf{p}, t) + \frac{\mathbf{p}}{m\gamma} \cdot \nabla f(\mathbf{r}, \mathbf{p}, t) + \frac{\mathbf{F}_L}{m} \cdot \nabla_{\mathbf{p}} f(\mathbf{r}, \mathbf{p}, t) = 0, \quad (2.3)$$

where momentum \mathbf{p} and acceleration \mathbf{a} have been carried out of the gradients because in the kinetic description they do not depend each other and:

$$\mathbf{F}_L = q(\mathbf{E}(\mathbf{r}, t) + \frac{\mathbf{p}}{m\gamma} \times \mathbf{B}(\mathbf{r}, t)), \quad (2.4)$$

is the Lorentz Force for both external or self-consistent electromagnetic fields (\mathbf{E}, \mathbf{B}) and $\gamma = \sqrt{1 + \frac{|p|^2}{(mc)^2}}$ is the Lorentz factor.

For a multi-species plasma, each species is represented by a correspondent $f_s(\mathbf{r}, \mathbf{p}, t)$ distribution function and q_s/m_s charge to mass ratio.

In real plasmas, for finite even if large number of particle N_s , collisionless conditions and hence the V.E. applies only as an approximation, depending on the plasma properties. The reference physical parameters of a neutral plasma in thermal equilibrium with the mean electron density n_0 and temperature T , are given by the electron plasma frequency ω_p , and the *Debye length*:

$$\lambda_D = \frac{V_{th}}{\omega_p}, \quad (2.5)$$

where $V_{th} = \sqrt{k_B T/m_e}$ is the thermal velocity and k_B is the Boltzmann constant.

A related physical parameter is the *electron skin-depth* $k_p = c/\omega_p \gg \lambda_D$.

These parameters are clearly invariant in the Vlasov limit $N_s \rightarrow \infty, (q_s, m_s) \rightarrow 0$ since the (q_s/m_s) ratio , the total charge, and mass for each species remain finite.

For finite number of particles, the electron density provides a measure of the mean inter-particle distance $l = n_0^{-3}$ and hence of the possible role of the two-body Coulombian interaction. A useful parameter to characterize the plasma conditions is given by the *Kubo number* Λ , representing the number of particles in a Debye sphere:

$$\Lambda = \frac{4\pi}{3} n_0 \lambda_D^3 \sim (\lambda_D/l)^3. \quad (2.6)$$

For sufficiently large Kubo number $\Lambda \gg 1$, that is for inter-particle distance much smaller than the Debye length, collisionless conditions and hence the dominance of collective effects over two body interactions are then applicable.

For laboratory conditions we have mentioned earlier the collisionless condition is

satisfied, since $l = [10^{-5} - 10^{-7}] \text{ cm}$, and therefore $l \ll \lambda_D$.

The analytical solution of the V.E. is generally impossible, and even the numerical solution is computationally expensive because of the number of the independent variables of (three positions, three momenta and time in Eq. (2.3)). Besides, V.E. is only linear in $f(\mathbf{r}, \mathbf{p}, t)$ if the electromagnetic fields are external fields superimposed on the plasma. If instead the electromagnetic fields are produced by the plasma itself, they have to be computed via the Maxwell's equations, and the source terms (charge and current density), depend on the evolution of $f(\mathbf{r}, \mathbf{p}, t)$.

In some symmetric configurations, where the number of independent variables is reduced [14], we are able to directly solve Eq. (2.3), but it is still extremely difficult to compare theoretical results to experimental results. As a matter of fact, we should measure the velocities of N particles, their modulus and directions in a spatial volume. This task is actually feasible only if the number of particles is not too large (e.g. for the solar wind, whose $f(\mathbf{r}, \mathbf{p}, t)$ is measured by spatial probes). In typical laboratory plasmas to perform such measurements seems infeasible.

However, if we renounce to some information about the momentum distribution, via averaging the distribution function over the momentum space, we obtain a simplified model which still gives useful information about the configuration space, developing the so called *Fluid Models*.

2.2 The cold fluid approximation

In the previous sections we defined the distribution function f and briefly derived the equation which rules its evolution (i.e. the Vlasov Equation), assuming electromagnetic forces and no collisions between plasma particles. We also explained the difficulties in dealing with the V.E. and defined the fluid approach as a possible

solution to a simplified version.

In deriving the fluid equations we start by the definition of fluid number density and momentum as the 0^{th} and 1^{st} order moments of the distribution function in the momentum space:

$$n(\mathbf{r}, t) = \int_{V_p} f(\mathbf{r}, \mathbf{p}, t) d\mathbf{p}, \quad (2.7)$$

$$\mathbf{P}(\mathbf{r}, t) = \frac{1}{n(\mathbf{r}, t)} \int_{V_p} \mathbf{p} f(\mathbf{r}, \mathbf{p}, t) d\mathbf{p}, \quad (2.8)$$

where V_p is the volume in momentum space, $n(\mathbf{r}, t)$ is the number density and $\mathbf{P}(\mathbf{r}, t)$ is the fluid momentum, i.e. the average momentum of the N particles in \mathbf{r} .

We similarly define the charge density ρ and the current density \mathbf{j} considering the distribution functions of both ions (f_i) and electrons (f_e) the plasma is composed by:

$$\rho(\mathbf{r}, t) = e \int_{V_p} [Z f_i(\mathbf{r}, \mathbf{p}, t) - f_e(\mathbf{r}, \mathbf{p}, t)] d\mathbf{p} \quad (2.9)$$

$$\mathbf{j}(\mathbf{r}, t) = e \int_{V_p} \mathbf{v} [Z f_i(\mathbf{r}, \mathbf{p}, t) - f_e(\mathbf{r}, \mathbf{p}, t)] d\mathbf{p} \quad (2.10)$$

where e is the electron charge and Z is the ionic atomic number and $\mathbf{v} = \mathbf{p}/mc\gamma$. In order to derive the evolution equations for the fluid quantities we have just defined, we start by taking the 0^{th} order moment in the momentum space of the V.E.:

$$\int_{V_p} \frac{\partial}{\partial t} f(\mathbf{r}, \mathbf{p}, t) d\mathbf{p} + \int_{V_p} \frac{\mathbf{p}}{mc\gamma} \cdot \nabla f(\mathbf{r}, \mathbf{p}, t) d\mathbf{p} + \int_{V_p} \frac{\mathbf{F}_L}{m} \cdot \nabla_{\mathbf{p}} f(\mathbf{r}, \mathbf{p}, t) d\mathbf{p} = 0. \quad (2.11)$$

The first integral on the LHS leads to the partial derivative of the number density.

If we take the spatial gradient outside the second integral, we obtain the flux of the fluid particles. The third integral leads to:

$$\int_{V_p} \frac{\mathbf{F}_L}{m} \cdot \nabla_{\mathbf{p}} f(\mathbf{r}, \mathbf{p}, t) d\mathbf{p} = q \int_{V_p} \frac{\mathbf{E}}{m} \cdot \nabla_{\mathbf{p}} f(\mathbf{r}, \mathbf{p}, t) d\mathbf{p} + q \int_{V_p} \frac{\mathbf{v} \times \mathbf{B}}{m} \cdot \nabla_{\mathbf{p}} f(\mathbf{r}, \mathbf{p}, t) d\mathbf{p}. \quad (2.12)$$

We apply the divergence theorem on the first integral after taking the electric field inside the momentum gradient (\mathbf{E} does not depend on the momentum), and integrate on the momentum space. The integral is zero, because the distribution function has to be limited over the whole momentum space.

The second integral is also zero. We prove it using the inverse chain rule on the momentum gradient and the cross product, leading to:

$$\int_{V_p} \frac{\mathbf{v} \times \mathbf{B}}{m} \cdot \nabla_{\mathbf{p}} f(\mathbf{r}, \mathbf{p}, t) d\mathbf{p} = \int_{V_p} \cdot \nabla_{\mathbf{p}} \cdot (f(\mathbf{r}, \mathbf{p}, t) \frac{\mathbf{v} \times \mathbf{B}}{m}) d\mathbf{p} - \int_{V_p} f(\mathbf{r}, \mathbf{p}, t) \nabla_{\mathbf{p}} \left(\frac{\mathbf{v} \times \mathbf{B}}{m} \right) d\mathbf{p}. \quad (2.13)$$

The first term is zero for the same reason of the term concerning the Electric field. The second term is also zero because the i -th derivative of the gradient is applied to a vector component which only contains j -th and k -th components.

We eventually obtain the *continuity equation*:

$$\frac{\partial}{\partial t} n(\mathbf{r}, t) + \nabla \cdot (n(\mathbf{r}, t) \mathbf{u}(\mathbf{r}, t)) = 0, \quad (2.14)$$

where:

$$\mathbf{u}(\mathbf{r}, t) \equiv \frac{1}{n(\mathbf{r}, t)} \int \mathbf{v} f(\mathbf{r}, \mathbf{p}, t) d\mathbf{p}, \quad (2.15)$$

is defined as *fluid velocity*.

In the non-relativistic limit $\gamma = 1$, \mathbf{u} can be identified with the momentum per unit mass \mathbf{P} , and the continuity equation has a closed form. This is not true in the relativistic case, since the gamma factor involves higher order moments.

It is straightforward to notice that via taking the 0^{th} order moment of the V.E. we introduced a 1^{st} order moment term, i.e. the last term on the LHS of Eq. 2.14. As a matter of fact, all n^{th} moments of the distributions function depends on higher $(n+1)^{th}$ moments, and for collisionless systems it is no possible, at least in principle, to reduce the kinetic V.E. to a closed set of fluid dynamical equations, since there is no physical principle allowing to truncate the moments sequence.

On the other hand for example, collisional plasma contains an added constraint assured by the entropy law:

$$S(t) = -k_B \int_{V_{6D}} [f \log f] d\mathbf{r} d\mathbf{p}, \quad \frac{dS}{dt} \geq 0. \quad (2.16)$$

A closure to second order moments has been presented [17] based on the $\gamma(\mathbf{p})$ expansion around $\mathbf{p} = \mathbf{P}$. If, as usual, phase space momentum is split in the form $\mathbf{p} = \mathbf{P} + \delta\mathbf{p}$, under the natural assumption $|\delta\mathbf{p}| \ll \mathbf{P}$, the gamma factor can be expanded in the form:

$$\gamma = \gamma_0 + \frac{\mathbf{P} \cdot \delta\mathbf{p}}{(mc)^2 \gamma_0} + \frac{(\mathbf{P} \cdot \delta\mathbf{p})^2}{((mc)^2 \gamma_0)^2} + o((\mathbf{P} \cdot \delta\mathbf{p})^3), \quad (2.17)$$

where the lowest order term is given by $\gamma_0 = \sqrt{1 + \frac{\mathbf{P} \cdot \mathbf{P}}{(mc)^2}}$. When integrated in the momentum space, linear terms disappear by definition:

$$\int_{V_p} \delta \mathbf{p} f(\mathbf{r}, \mathbf{p}, t) d\mathbf{p} = 0, \quad (2.18)$$

and quadratic terms carry informations on the thermal content of the plasma via the *pressure tensor*:

$$p_{i,j} = \frac{\Pi_{i,j}}{\gamma_0^2}, \quad (2.19)$$

where

$$\Pi_{i,j} = \int_{V_p} f(\mathbf{r}, \mathbf{p}, t) \delta p_i \delta p_j d\mathbf{p}. \quad (2.20)$$

The lowest order approximation corresponds to the *cold fluid limit* $|\Pi/\gamma_0^2| \rightarrow 0$, providing a closure of the fluid dynamic system to the first order moment:

$$\frac{\partial}{\partial t} \mathbf{u}(\mathbf{r}, t) + \nabla \cdot (\mathbf{u}(\mathbf{r}, t) \mathbf{U}(\mathbf{r}, t)) = n(\mathbf{r}, t) \mathbf{F}_L(\mathbf{r}, t), \quad (2.21)$$

where $\mathbf{U} = n\mathbf{P}$, and the Lorentz force is now expressed by:

$$\mathbf{F}_L = \frac{q}{m} \left[\mathbf{E}(\mathbf{r}, t) + \frac{\mathbf{U}(\mathbf{r}, t)}{mc\gamma} \times \mathbf{B}(\mathbf{r}, t) \right], \quad (2.22)$$

depending only on field variables. We can neglect thermal effects since for plasma acceleration schemes the thermal motion of the plasma particles is negligible with respect of the collective motion, which sustains the propagation of plasma waves. The electrons oscillating in the wake of the driver are typically relativistic, while the

temperature inside the plasma chamber hardly reaches a few eV.

By taking into account the continuity equation, the momentum equation 2.21 can be expressed in a non-conservative form, by:

$$\frac{\partial \mathbf{P}}{\partial t} = \nabla \cdot [\mathbf{u}\mathbf{P}] = \mathbf{F}_L(\mathbf{r}, t), \quad (2.23)$$

which is clearly density independent.

The *energy conservation equation* (i.e. the 2nd order moment of V.E.) is identically satisfied, and we are able to close the set of equations given by Eqs. 2.14, 2.21, the Maxwell's equations, and the definition of charge and current density Eqs. 2.9.

2.2.1 Linear regime

The set of equations we have derived so far completely describes both the plasma dynamics and the electromagnetic field evolution. The fluid approach for the evolution of the distribution function evaluation allows us to relate the spatial configuration of a plasma to the accelerating and focusing fields we are interested in for particle acceleration.

Nevertheless, a closed solution of this set of equations is still analytically infeasible, because of the non-linearity in the momentum equation and because of the non-linear coupling between the source terms of the Maxwell's equations and the plasma equations. Numerical solutions instead are rather straightforward to obtain via computer simulations with the so-called fluid codes, or with the hybrid codes, where kinetic and fluid approaches combine.

However, a closed model is possible to obtain if we consider several assumptions on plasma behaviour (small perturbations) and assume a certain degree of symmetry of

dynamics and fields, leading to the so called *linear regime* of plasma acceleration [18][19][20][21]. The complete derivation of the equations will be presented in Appendix A, following [23].

We start from the continuity equation Eq. 2.14 and the momentum equation Eq. 2.21, coupled with the wave equation for the electric field (for the magnetic field the procedure is the same):

$$\left(\nabla^2 - \frac{1}{c^2} \frac{\partial^2}{\partial t^2}\right) \mathbf{E}(\mathbf{r}, t) = \frac{1}{\varepsilon_0} \left(\nabla \rho(\mathbf{r}, t) + \frac{1}{c^2} \frac{\partial \mathbf{j}}{\partial t}\right), \quad (2.24)$$

where the plasma contribution appears in the charge and current density definitions. The scope of the model is to find a relation between the plasma density perturbation induced by an electron beam and the electromagnetic field developed in its wake. For small plasma perturbations we perform a first order expansion of Eqs. 2.14, 2.21, and 2.24 around the initial unperturbed conditions, corresponding to globally neutral and stationary plasma, such that $\rho_{0i} + \rho_{0e} = 0$ and $u_{0e} = 0$. If the density perturbation ρ_1 is small with respect to the unperturbed value, the second order terms of the expanded equations are negligible. We then obtain a linearized version of the wave equations for both electric and the magnetic field:

$$\left(\nabla^2 - k_p^2 - \frac{1}{c^2} \frac{\partial^2}{\partial t^2}\right) \mathbf{E}(\mathbf{r}, t) = \frac{1}{\varepsilon_0} \nabla(\rho_1 + \rho_b) + \frac{1}{\varepsilon_0 c^2} \frac{\partial \mathbf{j}_b}{\partial t}, \quad (2.25)$$

$$\left(\nabla^2 - k_p^2 - \frac{1}{c^2} \frac{\partial^2}{\partial t^2}\right) \mathbf{B}(\mathbf{r}, t) = -\frac{1}{\varepsilon_0 c^2} (\nabla \times \mathbf{j}_b), \quad (2.26)$$

where k_p is the plasma wave-number, and we assumed that the driver is an ultra-relativistic electron beam with charge density ρ_b and current density \mathbf{j}_b .

If the electromagnetic fields do not separately depend on time t and propagation

distance z , but only on the co-moving variable $\xi = v_\phi t - z$, where v_ϕ is the phase velocity of the plasma wave, related to the driver velocity, we obtain the following equations for the fields in cylindrical symmetry:

$$\left(\nabla_\perp^2 - k_p^2 - \frac{\partial^2}{\partial \xi^2} \right) \mathbf{E}(\mathbf{r}, \xi) = \frac{\hat{r}}{\varepsilon_0} - \frac{\hat{z}}{\varepsilon_0} \frac{\partial}{\partial \xi} \left(\frac{\rho_b}{\gamma^2} + \rho_1 \right), \quad (2.27)$$

$$\left(\nabla_\perp^2 - k_p^2 - \frac{\partial^2}{\partial \xi^2} \right) \mathbf{B}(\mathbf{r}, \xi) = \hat{\phi} \frac{\beta}{\varepsilon_0 c} \frac{\partial}{\partial r} \rho_b, \quad (2.28)$$

where $\beta = v_\phi/c$ and γ is the related Lorentz factor. Assuming the ion motion to be negligible ($m_i \gg m_e$) and combining the linearized Eqs. 2.14 and 2.21 with Gauss's law we obtain:

$$\left(\frac{\partial^2}{\partial \xi^2} + \frac{k_p^2}{\beta^2} \right) \rho_1 = -\frac{k_p^2}{\beta^2} \rho_1, \quad (2.29)$$

which is simply the 1D inhomogeneous Helmholtz wave equation.

We solve Eqs. 2.27, 2.28, and 2.29 in the Fourier space and finally obtain the set of integral equations for the electromagnetic fields:

$$E_z(r, \xi) = \frac{k_p^2}{\varepsilon_0} \int I_0(k_p r_<) K_0(k_p r_>) r' dr' \int_\xi^\infty \rho_b(r', \xi') \cos[k_p(\xi - \xi')] d\xi, \quad (2.30)$$

$$E_r(r, \xi) = -\frac{k_p}{\varepsilon_0} \int I_1(k_p r_<) K_1(k_p r_>) r' dr' \int_\xi^\infty \frac{\partial}{\partial r'} \rho_b(r', \xi') \sin[k_p(\xi - \xi')] d\xi, \quad (2.31)$$

$$B_\phi(r, \xi) = -\frac{\beta}{c\varepsilon_0} \int I_1(k_p r_<) K_1(k_p r_>) \frac{\partial}{\partial r'} \rho_b(r', \xi') r' dr', \quad (2.32)$$

where I_m and K_m are the modified Bessel functions of order m .

The forces acting on the witness beam are defined as the *longitudinal wake – field* $W_{\parallel}(\mathbf{r}, \xi) = E_z(\mathbf{r}, \xi)$, responsible for the accelerating regime, the energy spread, the energy transfer efficiency from the plasma wave to the witness beam, and the *transverse wake – field* $W_{\perp}(\mathbf{r}, \xi) = E_r(\mathbf{r}, \xi) - cB_{\phi}(\mathbf{r}, \xi)$, responsible of the focusing regime, the emittance and beam spot size evolution. We notice that the transverse $W_{\perp}(\mathbf{r}, \xi)$ and longitudinal $W_{\parallel}(\mathbf{r}, \xi)$ wake-fields are sinusoidal-like functions of ξ , out of phase by 90° degrees. This condition limits the maximum useful accelerating field to just a fraction of the real maximum, and inevitably induces correlated energy spread in the witness beam, as seen in Fig. 2.1.

The transverse forces are close to be linear only at for $r \sim 0$, meaning that the transverse dimension of the witness beam should be as narrow as possible to preserve the emittance. As a first order approximation, the transverse dimension is fixed for a given plasma density and energy of the witness beam: the so called *matching condition* for a plasma accelerator, which ensures that the beam spot size is conserved along the transport inside the plasma. Assuming that the transverse field is linear along the beam transverse rms length we have [24] $\sigma_r = \sqrt[4]{\frac{3}{\gamma}} \sqrt{\frac{\varepsilon_n}{k_p}}$, where ε_n is the given initial normalized emittance of the beam and γ_b the beam Lorentz factor. For a typical plasma acceleration set-up in the linear regime ($n_p \sim 10^{16} \text{ cm}^{-3}$), $\varepsilon_n \sim 1 \mu\text{m}$ and a few hundred MeV beam, the matched transverse beam size is lower than 10 μm . Besides, the length of the beam must be kept as short as possible, in order to avoid a strong difference in the accelerating gradient for different longitudinal portions of the beam, which would induce a large energy spread. Although these conditions are mandatory if the scope of the acceleration is to seed a new generation light source or an electron collider, it appears to be extremely difficult to generate such narrow and short beam while providing the charge required for the aforementioned applications.

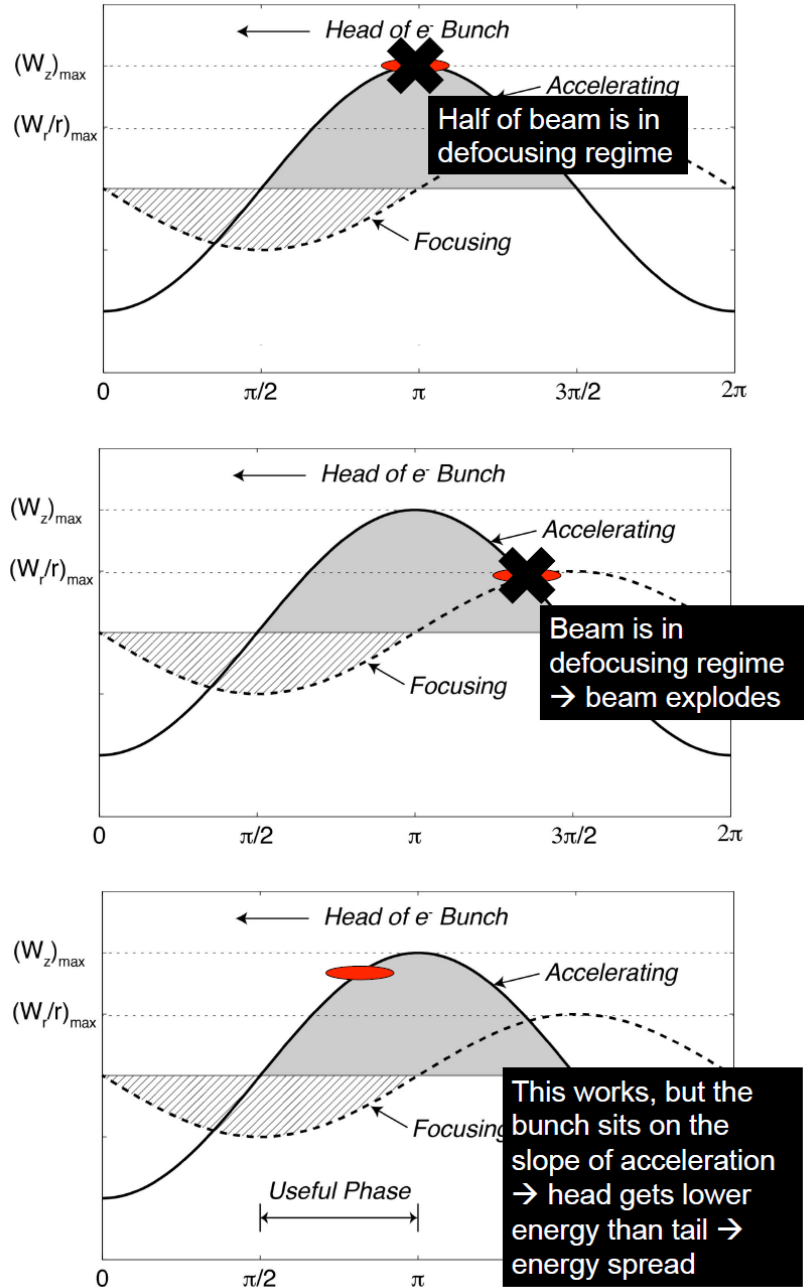


Figure 2.1. Different possible injection phases of a witness beam with respect of the accelerating and focusing wake-fields [25]

Nevertheless, the equations we obtained so far are particularly interesting in order to investigate dependencies and obtain simple scaling laws that, curiously [26], also ap-

ply to non-linear regime. It is useful for instance to evaluate the maximum achievable accelerating field, given a particular beam density distribution. For a bi-Gaussian density profile $\rho_b(r, \xi) = \frac{Q}{(2\pi)^{3/2}\sigma_r^2\sigma_z} e^{-r^2/2\sigma_r^2} e^{-\xi^2/2\sigma_z^2}$ where Q is the beam charge, we can analytically calculate the maximum accelerating field on axis $E_z(0, \xi)$ far from the driver beam ($\xi \gg \sigma_z$) if we assume the driver to be wide with respect of the plasma skin depth, i.e. $\sigma_r k_p \gg 1$ [27][28].

Given these assumptions, the radial integral goes to 1, and we can extend the longitudinal integration above the whole space. With few manipulations of Eq. 2.30 we obtain:

$$E_z(\xi \gg \sigma_z) = \left(\frac{e}{4\pi\varepsilon_0} \right) \left(\frac{2N}{\sigma_r^2} \right) e^{-\frac{(k_p\sigma_z)^2}{2}} \cos(k_p\xi), \quad (2.33)$$

where $N = Q/e$, or in normalized units:

$$\frac{E_z(\xi \gg \sigma_z)}{\frac{mc^2 k_p}{e}} = 2\pi \left(\frac{n_b}{n_0} \right) (k_p\sigma_z) e^{-\frac{(k_p\sigma_z)^2}{2}} \cos(k_p\xi), \quad (2.34)$$

where n_b, n_0 are the number densities of the beam and of the plasma background respectively. We can easily find that, in order to maximize the accelerating field, the choice for the length of a driver beam whose should be $k_p\sigma_z = \sqrt{2}$, the so called *resonant length*, for a fixed density perturbation n_b/n_0 . For a given beam geometry, both equations obviously suggest using a driver beam denser than the plasma background, i.e. $n_b/n_0 \gg 1$. Finally and oddly, even with the assumption of wide driver beam the model tells us to reduce as much as possible the transverse dimension of the driver beam.

Another interesting figure of merit that has been widely studied in the linear regime is the so called *transformer ratio*. As we have already mentioned in the introduc-

tion, the scope of the plasma as an accelerating and focusing device is to transfer the energy deposited by the driver beam to the witness beam. In addition to the energy transfer between the driver and the plasma, another crucial aspect is the ratio between the energy loss of the driver and the energy gain of the witness. As a matter of fact, this ratio influences the accelerating regime determining the useful accelerating length.

It has been proved, [19][20] that the maximum transformer ratio achievable in the linear regime is $R = |E_{max}^+ / E_{max}^-| = 2$, provided the wake excitation is produced by a longitudinally symmetric driver beam. Considerable effort [29][30][31][32] have been made out to overcome this limit, i.e. to use non-symmetric bunches or train of bunches with a rising charge, however raising at the same time the technological difficulties of the scheme.

Instead, in the non-linear regime transformer ratios higher than 10 are achievable, and because of this last reason and other that we will explain later, we relied on the non-linear regime to perform our studies on injection and acceleration.

2.2.2 Breakdown of the linear regime

In the previous section we developed the linearized set of equations for plasma acceleration and we presented a few simple applications of these results. For instance, we noticed how the maximum accelerating field scales with the driver beam density (Eq. 2.34) in the limit of wide $k_p \sigma_r \gg 1$ beam. We now want to generalize this result for any beam transverse size and to show how the linear model breaks when the normalized beam density approaches unity.

It is convenient to write, for a bi-Gaussian beam, the density distribution as the product of the longitudinal and transverse distributions, $\rho_b(r, \xi) = \rho_{b\parallel}(\xi)\rho_{b\perp}(r, \xi)$.

One can prove[21][27], that for the longitudinal electric field described by Eq. 2.30 the relation $E_z(r, \xi) = Z'(\xi)R(r)$ holds, with:

$$Z'(\xi) = \int_{\xi}^{\infty} \rho_{b\parallel}(\xi') \cos[k_p(\xi - \xi')] d\xi, \quad (2.35)$$

$$R(r) = \frac{k_p^2}{\varepsilon_0} \int_0^{\infty} I_0(k_p r_{<}) K_0(k_p r_{>}) \rho_{b\perp}(r') r' dr', \quad (2.36)$$

where we split the accelerating field in two uncorrelated functions, respectively of the longitudinal and transverse dimension. The equation for the maximum accelerating field, without the assumption of wide beam, changes because of the dependence Eq. 2.36 on the transverse dimension of the driving beam. As a matter of fact, it can be proved [28] that the on axis value of the transverse component of the accelerating field is:

$$R(0) \simeq \begin{cases} k_p^2 \sigma_r^2 [0.05797 - \ln(k_p \sigma_r)] & , k_p \sigma_r < 0.5 \\ \left(\frac{k_p^2 \sigma_r^2}{2}\right) e^{\frac{k_p^2 \sigma_r^2}{2}} \Gamma\left(0, \frac{k_p^2 \sigma_r^2}{2}\right) & , \forall k_p \sigma_r \\ 1 & , k_p \sigma_r \gg 1 \end{cases} \quad (2.37)$$

where $\Gamma(0, s) = \int_b^{\infty} \frac{e^{-t}}{t} dt$ is the gamma function.

Notice that Eq. 2.34 was only a particular case of the more general result:

$$\frac{eE_z(r=0, \xi \gg \sigma_z)}{mc^2 k_p} = 2\pi \left(\frac{n_b}{n_0}\right) \left(k_p \sigma_z e^{-\frac{k_p \sigma_z^2}{2}}\right) \left(\frac{k_p^2 \sigma_r^2}{2} e^{\frac{k_p^2 \sigma_r^2}{2}}\right) \Gamma\left(0, \frac{k_p^2 \sigma_r^2}{2}\right) \cos(k_p \xi), \quad (2.38)$$

where we have explicitly written the longitudinal field components.

We are interested in studying the linear plasma response in the regime corresponding

to narrow beam, $k_p\sigma_r \ll 1$, in order to define the limit of validity of the linear regime while the density of the driving beam rises. For narrow beams the transverse component of the accelerating field in Eq. 2.38 can be asymptotically expanded as the logarithmic function in Eq. 2.37, leading to:

$$\frac{eE_z(r = 0, \xi \gg \sigma_z)}{mc^2 k_p} = 2\pi \left(\frac{n_b}{n_0} \right) \left(k_p \sigma_z e^{-\frac{k_p \sigma_z^2}{2}} \right) k_p^2 \sigma_r^2 [0.05797 - \ln(k_p \sigma_r)] \cos(k_p \xi), \quad (2.39)$$

where, with the assumption $k_p\sigma_r \ll 1$, the constant term in the logarithm can be neglected, and appears rather clearly how the accelerating field diverges as the transverse dimension is reduced, while keeping every other parameter constant.

This aspect of the linear regime is clearly non-physical, and it shows the limit of the linear theory of plasma acceleration. It has been proved [28] how the linear model breaks for a normalized beam density close to $n_b/n_0 \sim 10$. The investigation has been carried out via comparison with PIC simulations performed varying the transverse dimension of the driver beam for various beam longitudinal densities $\Lambda = (n_b/n_0)k_p^2 \sigma_r^2 = \int (n_b(r', \xi)/n_0)r' dr'$, related to the beam current. We report a few results of this study in Fig. 2.2, in order to understand the details of the linear theory breaking, and to introduce the non-linear theory that will be covered in the next section.

Linear theory has been developed assuming a small density perturbation, namely $n_1 \ll n_0$, to neglect the contribution of the non-linear terms in the plasma equations. The condition on plasma perturbation reflects immediately on the source of the plasma perturbation, i.e. the beam density. For a beam with very small charge [a) in Fig. 2.2], the transverse momentum that plasma electrons achieve via the beam space charge forces is limited, and a collective harmonic oscillation of the

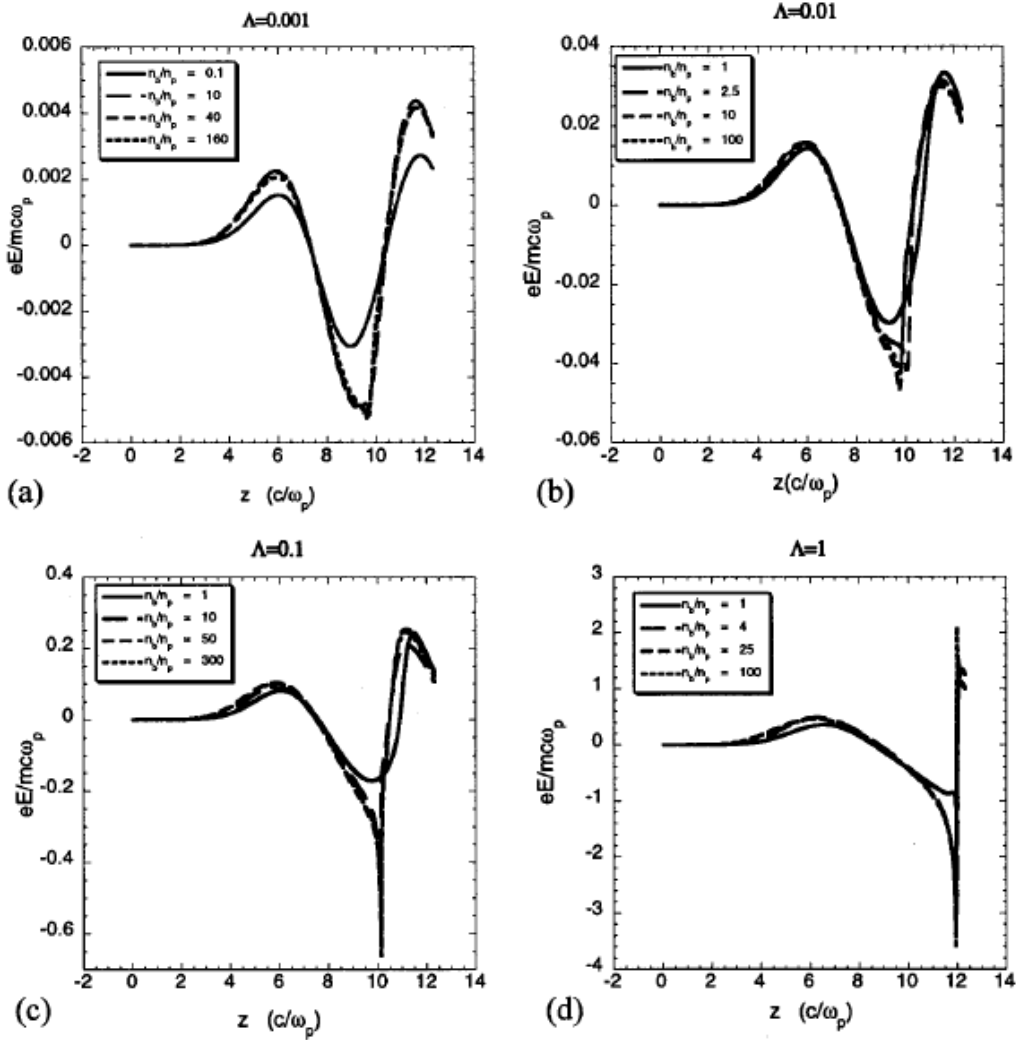


Figure 2.2. The accelerating field obtained varying in four different beam current scenarios the beam width: a) $\Lambda = 0.001$ and b) $\Lambda = 0.01$, where the sinusoidal like shape is kept even with very narrow beam $n_b/n_0 > 100$, c) $\Lambda = 0.1$ where the slope of the field steepen but is still below the 1D Wave-breaking limit, d) $\Lambda = 1$ where even for lower densities than the other cases the electric field rises up to values higher than the 1D Wave-breaking limit, showing full non-linear behaviour[28]

electrons in the transverse plane takes place, even for very narrow beams. If we raise the current of the beam [b), [c) in Fig. 2.2] the non-linearity starts to occur at normalized densities close to 10, until [d) in Fig. 2.2] trajectory crossing of the

electrons and an-harmonic oscillations take place, and the so called *full blowout* occurs even at $n_b/n_0 \sim 1$.

A simple analysis of the dependence of non-linearity and trajectory crossing to the beam current Λ is presented in Appendix B. Here it interesting to notice that for a given beam length and charge ($k_p\sigma_z \sim \sqrt{2}$, $\Lambda = \text{cost}$), if the transverse dimension of the beam is reduced the transverse kick felt by a background electron gets automatically larger, being $E_{r,max} \sim 0.45 \frac{\Lambda}{k_p\sigma_r}$. Besides, the radial position corresponding to the maximum radial electric field moves towards the beam axis, being $r_{max} \sim 1.5\sigma_r$. We eventually get such a transverse field in a position so close to the axis that a large amount of plasma electrons with initial position $r_0 < r_{max}$ will cross plasma electrons with $r_0 > r_{max}$.

As clearly seen from Fig. 2.2, if we raise the beam current, the blowout is likely to appear even for larger beam spot sizes.

2.2.3 Non-linear regime

So far, we have discussed the equations ruling plasma acceleration in the linear regime. We can derive Eqs. 2.30, 2.31 and 2.32 only if the density perturbation, related to the beam density distribution, is small compared with the equilibrium plasma density $n_b \ll n_p$. Given this assumption, we were able to perform a first order expansion neglecting the higher order terms, and we self-consistently closed the set of equations.

In the previous section we showed the limits of the linear model, presenting the studies on the accelerating field on axis behaviour as the beam width its density are changed. When the beam density is close to $n_b/n_p > 10$, the linear fluid model breaks showing an unphysical divergent trend, basically because the plasma electrons

receive such a high transverse momentum that the trajectories start to cross each other.

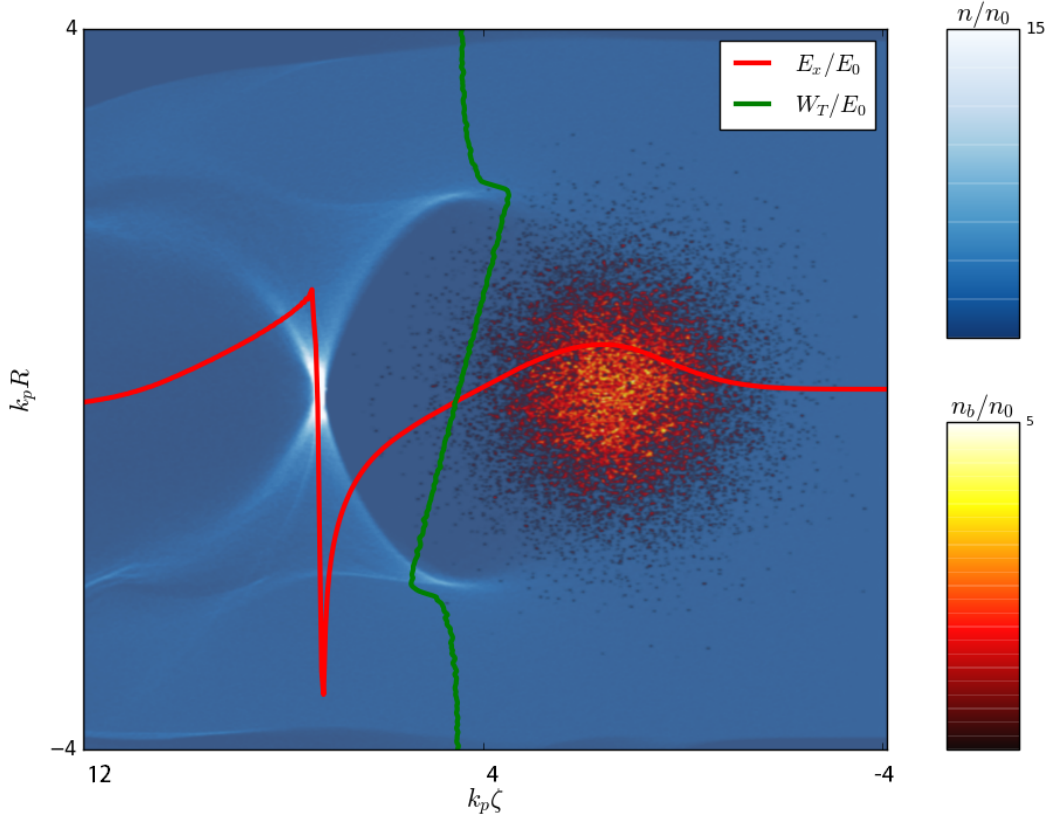


Figure 2.3. The longitudinal electric field (red curve) and transverse field (green curve) superimposed on a contour plot of the bunch+background density in the blowout regime, taken from 3D PIC simulation with the PIC Code ALaDyn. The field and the density are taken in dimensionless units where $E_0 = mc^2k_p/e$ is the 1D Wave-breaking limit

A high-density perturbation is induced and the *blowout regime* develops. The blowout regime is also typically called *bubble regime* [33][34], because of the quasi spherical shape of density perturbation behind the driver. The force the beam exerts on the background plasma electrons is so intense that no electron is left in the wake of the driver, and a uniform positive charged ion cavity is left.

The bubble regime shows very interesting features, with respect to particle accelera-

tion and transport. As we have already mentioned, a relevant parameter regarding efficient acceleration is the transformer ratio, defined in Section 2.2.1 as the ratio between the maximum accelerating field felt by the witness beam (i.e. the energy gain), and the maximum decelerating field felt by the driving beam (i.e. the energy loss). For longitudinally symmetric drivers in the linear regime this parameter has a maximum achievable value $R = 2$, and only complicated technological schemes can increase this value. On the other hand in the bubble regime there is no such limitation, and it R easily reaches values higher than 10.

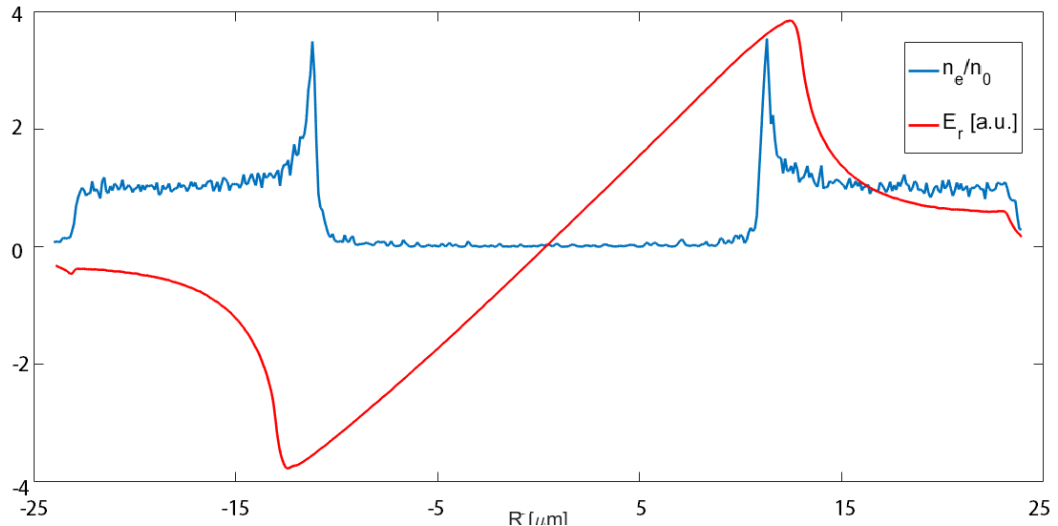


Figure 2.4. The line-out of the linear transverse force $W_{\perp} = E_r - cB_{\phi}$ superimposed onto the line-out of the background plasma density, taken from 3D PIC simulation with the PIC Code ALaDyn.

Besides, for the applications of particle accelerators the accelerating regime is not the only important feature. High brightness, high luminosity beams are required to drive new generation of light sources or particle colliders. An efficient transport is therefore a mandatory task to take care of. In the linear regime of plasma acceleration the transverse electric field has a non-linear dependence on the radius, because of the

incomplete blowout of the electrons in the wake of the driver beam. On the other hand in the bubble regime the wake consists simply in an ion cavity with uniform density, determining linear transverse forces (Fig. 2.4) which preserve the emittance of the witness beam.

Both high transformer ratios and emittance preserving transport are achieved thanks to the high-density perturbation typical of the blowout regime. Unfortunately, we cannot perform a linearization of the equations, because the assumption $n_1 \ll n_0$ does not hold anymore. Consequently, a complete and self-consistent analytical model for the blowout regime does not exist, and therefore numerical simulations are used as the main method of investigation for such regime.

Nevertheless it is interesting to present the derivation of the equations of the blowout regime following the model developed by Wei Lu [35][36], and to compare its results with PIC simulations performed with the 3D PIC Code ALaDyn [37][38]. We start from the Maxwell's equations for the potentials ϕ and \mathbf{A} in the Lorentz gauge

$$\frac{1}{c} \frac{\partial}{\partial t} \phi + \nabla \cdot \mathbf{A} = 0:$$

$$\left(\frac{1}{c^2} \frac{\partial^2}{\partial t^2} - \nabla^2 \right) \phi = \frac{\rho}{\varepsilon_0}, \quad (2.40)$$

$$\left(\frac{1}{c^2} \frac{\partial^2}{\partial t^2} - \nabla^2 \right) \mathbf{A} = \mu_0 \mathbf{J}, \quad (2.41)$$

where the current density \mathbf{J} and the charge density ρ satisfy the charge conservation equation $\frac{\partial \rho}{\partial t} + \nabla \cdot \mathbf{J} = 0$. As we have already shown in section 2.2.1, if we perform a change of variable $\xi = ct - z$, the wave equations simplify in:

$$-\nabla_{\perp}^2 \phi = \frac{\rho}{\varepsilon_0}, \quad (2.42)$$

$$\nabla_{\perp}^2 \mathbf{A} = -\mu_0 \frac{\mathbf{J}}{c}, \quad (2.43)$$

and one Poisson-like equation for the *pseudo-potential* $\psi = \phi - A_z/c$:

$$-\nabla_{\perp}^2 \psi = \left(\frac{\rho}{\varepsilon_0} - \mu_0 \frac{J_z}{c} \right). \quad (2.44)$$

To evaluate the charge density and current density of the plasma we couple Eq. 2.44 to the momentum equation, written in the co-moving variable:

$$\frac{d}{dt} \mathbf{p} = \frac{d}{d\xi} \frac{d\xi}{dt} \mathbf{p} = \quad (2.45)$$

$$= (c - v_z) \frac{d}{d\xi} \mathbf{p} = q (\mathbf{E} + \mathbf{u} \times \mathbf{B}), \quad (2.46)$$

where $v_z = dz/dt$ is the longitudinal velocity of the plasma electrons. In the blowout regime we are not allowed to neglect relativistic effects as we did in the linear regime, because the intensity of the beam field can radially accelerate background plasma electrons up to relativistic velocities.

If potentials and fields do not separately depend on space and time but only via the co-moving variable, there exists a constant of motion for a charged particle, namely $H - cP_z = \text{cost}$ (Section 2.3). The existence of this constant of motion leads to a direct relation between the longitudinal momentum of a charged particle, the transverse momentum, and the pseudo-potential ψ :

$$\frac{p_z}{mc} = \frac{1 + (\frac{p_{\perp}}{mc}) - \left(1 + \frac{q\psi}{mc^2}\right)^2}{2 \left(1 + \frac{q\psi}{mc^2}\right)}, \quad (2.47)$$

$$\gamma = \frac{1 + p_{\perp}^2 + (1 + \psi)^2}{2(1 + \psi)}. \quad (2.48)$$

These relations allow us to just focus on evaluating the transverse component of the

momentum and the pseudo potential, in order to completely solve the dynamics of the plasma electrons and reconstruct accelerating and focusing fields. We assume cylindrical symmetry and use normalized quantities, where time is normalized to ω_p^{-1} , velocity to the speed of light c , mass to the electron mass and charge to e .

The transverse force is therefore $F_\perp = -(E_r - v_z B_\phi)$, and we can easily relate the electric and magnetic fields to the scalar and vector potential, as:

$$E_r = -\frac{\partial}{\partial r}\phi - \frac{\partial}{\partial \xi}A_r, \quad (2.49)$$

$$B_\phi = -\frac{\partial}{\partial r}A_z - \frac{\partial}{\partial \xi}A_r. \quad (2.50)$$

Therefore the transverse force becomes:

$$F_r = \frac{\partial}{\partial r}\phi - v_z \frac{\partial}{\partial r}A_z + (1 - v_z) \frac{\partial}{\partial \xi}A_r, \quad (2.51)$$

and we only have to find a self-consistent way to express the potential components. If we assume to be inside the ion bubble, i.e. for electrons having transverse position $r \leq r_b$ and $r \gg \sigma_r$, where r_b is the bubble radius and σ_r is the transverse rms dimension of the beam, created by a bi-Gaussian electron beam with density $n_b = n_{b0}e^{-r^2/2\sigma_r^2}e^{-\xi^2/2\sigma_z^2}$, the source terms for Eq. 2.40 and Eq. 2.41 are respectively $\rho = 1 - n_b$ and $J_z = -n_b$, where in the first term only appear the normalized ion density and the normalized beam density, and in the second term only the beam current. We solve the Poisson-like equations 2.42, 2.44 to get:

$$\phi = \phi_0(\xi) - \frac{r^2}{4} + \int_0^r n_b r' dr = \phi_0 - \frac{r^2}{4} + \ln r \lambda(\xi), \quad (2.52)$$

$$A_z = A_{z0}(\xi) + \ln r \lambda(\xi), \quad (2.53)$$

$$\psi = \psi_0 - \frac{r^2}{4}, \quad (2.54)$$

where $\phi_0(\xi)$ and $A_{z0}(\xi)$ are the on-axis values respectively of the scalar potential and of the z-component of the vector potential. We obtain the radial component of the vector potential via the gauge condition expressed in the co-moving variable $\frac{A_r}{r} = -\frac{1}{2} \frac{d\psi_0}{d\xi}$. The transverse force then becomes:

$$F_\perp = -\frac{r}{2} + (1 - v_z) \frac{\lambda(\xi)}{r} - \frac{1}{2} (1 - v_z) \frac{d^2 \psi_0}{d\xi^2} r \quad (2.55)$$

We can now express the ξ derivative of the transverse momentum via the expression of γ in Eq. 2.48 as a differential equation for the bubble radius, i.e. the trajectory of the innermost electron:

$$\begin{aligned} (1 - v_z) \frac{d}{d\xi} p_\perp &= \frac{1 + \psi}{\gamma} \frac{d}{d\xi} (\gamma v_\perp) = \\ &= \frac{1 + \psi}{\gamma} \frac{d}{d\xi} (\gamma \frac{d}{dt} r_\perp) = \\ &= \frac{1 + \psi}{\gamma} \frac{d}{d\xi} (\gamma \frac{1 + \psi}{\gamma} \frac{d}{d\xi} r_\perp) = \\ &= \frac{2(1 + \psi)^2}{1 + (1 + \psi)^2 (\frac{d}{d\xi} r_b)^2 + (1 + \psi)^2} \frac{d}{d\xi} ((1 + \psi) \frac{d}{d\xi} r_b), \end{aligned} \quad (2.56)$$

where we called $r_\perp = r_b$ the bubble radius and used $dp_\perp/d\xi = d/d\xi(\gamma/dr_\perp/dt)$.

The momentum equation is now written in such a way it reproduces the trajectory

of the innermost electron inside the ion cavity that feels the force in Eq. 2.55: combining it with Eq. 2.56 we get:

$$\frac{2(1+\psi)^2}{1+(1+\psi)^2(\frac{d}{d\xi}r_b)^2+(1+\psi)^2}\frac{d}{d\xi}((1+\psi)\frac{d}{d\xi}r_b) = -\frac{r}{2} + (1-v_z)\frac{\lambda(\xi)}{r} - \frac{1}{2}(1-v_z)\frac{d^2\psi_0}{d\xi^2}r \quad (2.57)$$

The pseudo-potential ψ obeys to the Poisson-like equation Eq. 2.44, and we can solve it to find an expression to plug into Eq. 2.57. We start from the explicit form of Eq. 2.44:

$$-\frac{1}{r}\frac{\partial}{\partial r}(r\frac{\partial}{\partial r}\psi) = \rho - J_z = (n_i(r,\xi) - n_e(r,\xi)) - (-n_e(r,\xi)v_z(r,\xi)), \quad (2.58)$$

where the ion density is a unitary constant $n_i(r,\xi) = 1 \forall r,\xi$, while the electron density is an unknown function of r and ξ . The source term for Eq. 2.58 can be written as a function of the radius as:

$$\rho - J_z = \begin{cases} 1, & r < r_b \\ 1 - n_e(r,\xi)(1 - v_z(r,\xi)), & r_b \leq r \leq r_b + \Delta \\ -1, & r \rightarrow \infty \end{cases} \quad (2.59)$$

where we defined three main regions: the ion cavity ($r < r_b$), that we assume to be empty of electrons, a narrow sheet ($r_b \leq r \leq r_b + \Delta$) where the blowout electrons accumulate to shield the positive charge of the ions, and the unperturbed region, where the plasma is globally neutral.

The solution of Eq. 2.58 can be found via the Green's function method, leading to the integral function:

$$\begin{aligned}\psi(r, \xi) &= \ln r \int_0^r r' \{n_e(r', \xi)[1 - v_z(r', \xi)] - 1\} dr' + \\ &+ \int_r \infty r' \ln r' \{n_e(r', \xi)[1 - v_z(r', \xi)] - 1\} dr'.\end{aligned}\quad (2.60)$$

We know from the continuity equation written in the co-moving variable that $\frac{\partial}{\partial \xi} \int r(\rho - J_z) dr = 0$, because no radial electron current flows inside the ion cavity.

We use this general condition to derive a model for the source term $\rho - J_z$ inside the electron sheet. As proposed in [35][36] and shown in Fig. 2.5, we assume it to be constant along the radial direction:

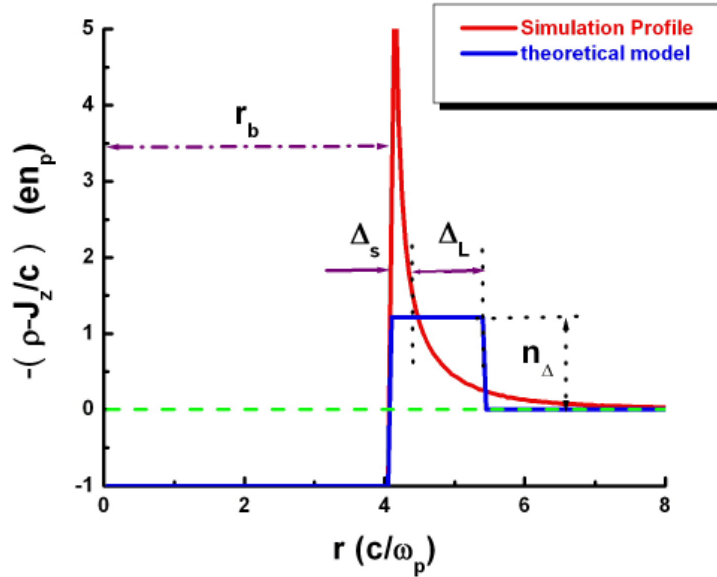


Figure 2.5. The radial profile of the source term $\rho - \alpha e_z$ for the pseudo potential $\psi(r, \xi)$, with the analytical approximated model in blue and the PIC simulation profile in red. [35][36]

This assumption is strictly valid only in the region where $\Delta \ll r_b$, so it reliably approximates the density profile for every ξ but the head and the back of the ion

cavity, where $\Delta \sim r_b$. We have:

$$\int_0^{r_b} r(-1)dr + \int_{r_b}^{r_b+\Delta} rn_\Delta = 0 \rightarrow n_\Delta = \frac{r_b^2}{(r_b + \Delta)^2 - r_b^2} \quad (2.61)$$

We insert n_Δ into Eq. 2.60, solve the integrals and then apply the continuity condition between the particular solution of pseudo-potential inside the ion cavity Eq. 2.54 and the general solution Eq. 2.60. We finally find an expression for the on-axis value of the pseudo-potential ψ_0 :

$$\psi_0 = \frac{r_b^2}{4} \frac{(1 + \alpha)^2}{(1 + \alpha)^2 - 1} \ln(1 + \alpha)^2, \quad (2.62)$$

where $\alpha = \frac{\Delta}{r_b}$. We eventually obtain the full equation for the pseudo-potential, with the assumption of constant source term over the electron sheet:

$$\psi(r, \xi) = \frac{r_b^2}{4} (\beta(r_b(\xi)) + 1) - \frac{r^2}{4}, \quad (2.63)$$

where $\beta = \frac{(1 + \alpha)^2}{(1 + \alpha)^2 - 1} \ln(1 + \alpha)^2 - 1$. Now we just have to insert Eq. 2.63 into Eq. 2.57 in order to get a full description of the trajectory of the innermost electron, which is related to the ion cavity geometry and therefore to the accelerating and focusing forces developed inside of it.

A great simplification of the derivation is provided if we assume the width of the electron sheet to be constant also along the longitudinal direction, i.e. $\Delta(\xi) \simeq \text{const}$. As we already mentioned, this assumption is strictly valid only in the region far from the head and the back of the ion cavity, but still it provides an elegant and compact differential equation for the trajectory of the innermost electron and the accelerating field:

$$A(r_b) \frac{d^2 r_b}{d\xi^2} + B(r_b) r_b \left(\frac{dr_b}{d\xi} \right)^2 + C(r_b) r_b = \frac{\lambda(\xi)}{r_b}, \quad (2.64)$$

$$E_z(r_b, \xi) = \frac{d\psi_0}{d\xi} = \frac{d}{d\xi} \left\{ \frac{1}{4} r_b^2 \{ \beta(r_b, \xi) + 1 \} \right\}, \quad (2.65)$$

where the coefficients depending on the bubble radius $r_b(\xi)$ are:

$$A(r_b) = 1 + \left(\frac{1}{4} + \frac{\beta}{2} + \frac{1}{8} r_b \frac{d\beta}{d\xi} \right) r_b^2, \quad (2.66)$$

$$B(r_b) = \frac{1}{2} + \frac{3}{4} \beta + \frac{3}{4} r_b \frac{d\beta}{dr_b} + \frac{1}{8} r_b^2 \frac{d\beta}{dr_b^2}, \quad (2.67)$$

$$C(r_b) = \frac{1}{4} \left(1 + \frac{1}{\left(1 + \frac{\beta}{4} r_b^2 \right)} \right). \quad (2.68)$$

Equations 2.64 and 2.65 can be numerically integrated, and in Fig.2.6 we show the comparison between the results and a PIC simulation, where we used a driver bunch with $k_p \sigma_z = \sqrt{2}$, a plasma density $n_0 \sim 10^{18} \text{ cm}^{-3}$ with charge 550pC.

The model we have presented so far is very close to PIC simulation results as long as the assumptions we have made are observed, i.e. $\Delta \ll r_b$ and $\Delta(\xi) = \text{cost}$. The bubble profile is very well reproduced ($r_{max} \sim 2.5 \sqrt{n_{b0} \sigma_r}$, as we will show on Appendix B), with just a small discrepancy at the rear side of the bubble, while the electric field deviates much more in the same region. The reason of this deviation resides in the fact that E_z is a highly non-linear function of r_b , and even a little deviation of the theoretical r_b from the simulation value determines a great deviation in E_z .

Nevertheless, the model allows to numerically derive the shape of the blowout region, and the accelerating field it reproduces has been used for its simplicity to derive a

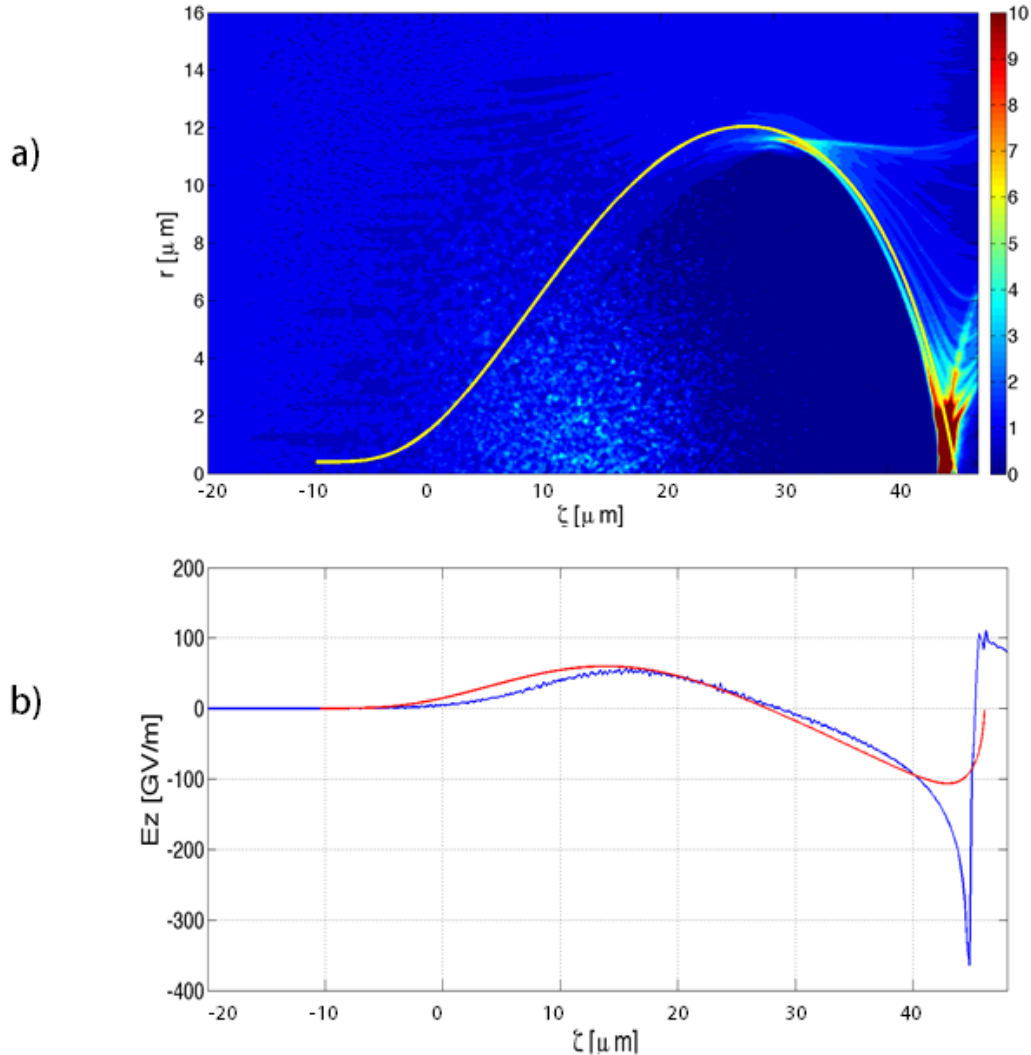


Figure 2.6. Comparison between the theoretical prediction and the result of PIC simulation performed with the PIC code ALaDyn. a) shows the $r_b(\xi)$ curve in yellow and the 2D contour plot of bubble density profile from ALaDyn: the bubble profile is perfectly represented, but a small deviation in the rear side of the bubble where the assumption $\Delta \ll r_b$ falls, as expected. b) shows in the red curve the $E_z(r = 0, \xi)$ and in the blue curve the line-out of the accelerating field from ALaDyn: the difference between PIC code and theory is here more pronounced as we approach the back of the bubble, where the assumption of $\Delta(\xi) = \text{const}$ is no longer valid.

non-linear theory for beam loading for an external injection scheme [41]. Besides, in the assumption of ultra-relativistic blowout regime, i.e. $\alpha, \beta \ll 1$, it is possible to obtain scaling laws for both the longitudinal field and the transverse force.

In the ultra-relativistic blowout regime Eq. 2.64 becomes:

$$r_b \frac{d^2 r_b}{d\xi^2} + 2 \left(\frac{dr_b}{d\xi} \right) + 1 = \frac{4\lambda(\xi)}{r_b}, \quad (2.69)$$

which is close to the equation for the surface of a sphere but the mid-term of the Left-Hand-Side, which is doubled, meaning an extra bending of the trajectory downward as $\frac{dr_b}{d\xi}$ increases. With the assumption of short beam, most of the trajectory of the innermost electron is insensitive to the space charge force of the driving beam, therefore we can neglect $\lambda(\xi)$. We rewrite the LHS of Eq. 2.69 as:

$$\frac{d}{d\xi} \left(\frac{1}{2} r_b \frac{dr_b}{d\xi} \right) = -\frac{1}{2} - \frac{1}{2} \left(\frac{dr_b}{d\xi} \right)^2, \quad (2.70)$$

and we compare it with the ξ derivative of Eq. 2.65. At the centre of the ion column, i.e. where $r_b = r_{max}$, the slope of the accelerating field is $dE_z/d\xi = -1/2$, and increases as the $dr_b/d\xi$ increases.

Besides, in the relativistic blowout regime the transverse force on a relativistic charge far from the driver $v_z \sim c$ can be written as:

$$E_r - B\phi = -\frac{\partial(\phi - A_z)}{\partial r} = \frac{\partial\psi}{\partial r}, \quad (2.71)$$

where only the contribute of the ion charge is left, since the radial plasma current terms $\partial A_r / \partial \xi$ cancel out. The pseudo-potential expression Eq. 2.63 simplifies as $\psi(r, \xi) = (r_b^2 - r^2)/4$, and we obtain the already mentioned linear focusing force

$$E_r - B_\phi = r/2.$$

There exist other theoretical models that cover the features of the non-linear regime[42][43][44], but none of them offer such a complete and simple description of the non-linear plasma dynamics and field generation as the one we have presented so far. In fact, the assumptions used to derive this model limit the addressable physics to the volume of the bubble where trajectory crossing does not occur and therefore it does not consider the phenomenon of wave breaking, which will be addressed in the next section.

2.3 Wave breaking and particle trapping

In the main introduction we presented the so called non-relativistic 1D cold Wave-breaking limit as a fundamental parameter widely used as a scale of the electric field developed in the fully depleted bubble. A more detailed derivation of this parameter and the analysis of its relationship with the onset non-linear behaviour is presented in the Appendix B. When the density perturbation becomes comparable to the unperturbed density, relativistic effects become relevant and the result is no longer valid, even though it is still frequently used as a figure of merit for the intensity of the electric field in the bubble. In our discussion, we do not claim to fully cover the *Wave – breaking* phenomenon, as we will restrict ourselves to its connection to particle trapping, in order to introduce the internal-injection concept.

A more refined model to evaluate the wave-breaking limit even for relativistic regimes has been presented in various works [45][46] each following the derivation of undriven non-linear plasma waves presented by Akhiezer and Polovin [47].

For a cold, unmagnetized plasma in planar geometry, it can be proved that the density perturbation and the electric field are given by the equations:

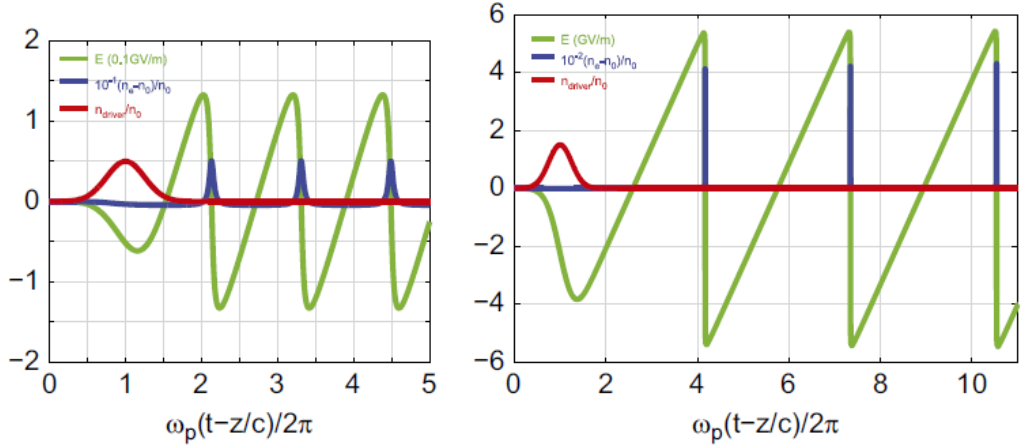


Figure 2.7. Steepening of the Electric field and singularity of the density perturbation when the fluid velocity, induced by the driver space charge force, approaches the phase velocity of the wave

$$n_e = \frac{n_0}{1 - u_x/v_{phi}}, \quad (2.72)$$

$$E(\xi) = \frac{m\omega_p c}{e} \sqrt{2(\gamma_m - \gamma[u_x(\xi)])}, \quad (2.73)$$

where u_x is the fluid velocity and γ_m is the maximum Lorentz factor of the plasma wave.

The numerical solution for a beam driven plasma wake are shown in Fig. 2.7, where the dependence of the fluid velocity to the beam driver density is made clear. As the fluid velocity approaches the phase wave velocity, the density perturbation shows a spiked behaviour with a simultaneous lengthening of the plasma period by a factor γ . The electric field assumes a sawtooth shape, with zeros at the density spikes.

When the fluid velocity equals the wave phase velocity, the density distribution exhibits a singularity. The trajectories of the particles intersect each other, which means the fluid velocity is not a single-valued function, and the fluid model does

not hold anymore. The periodic behaviour of the model is lost and the wave is said to break. In this rather simple 1D model the onset of trajectory crossing directly relates to wave-breaking, and one can calculate the maximum value of electric field sustainable by a relativistic plasma wave, corresponding to the inversion position of the 1D motion, where $u_x = 0$:

$$\max(E_x) = \frac{m\omega_p c}{e} \sqrt{2(\gamma_\phi - 1)} = E_{rel.wb}. \quad (2.74)$$

We can also relate the energy of a trapped particle with the potential inside the wave via simple energy conservation [48]: in the frame moving at the phase velocity of the wave, if the potential well is deep enough to accelerate background plasma electrons up to the kinetic energy of the wave. We have:

$$-e\Delta\phi' \geq \Delta K = (\gamma_\phi - 1)mc^2, \quad (2.75)$$

where K is the kinetic energy of an initially stationary electron and ϕ' is the electrostatic potential inside the bubble. If we go back to the laboratory frame we obtain:

$$\frac{e}{mc^2}\Delta\phi \leq \frac{1}{\gamma_\phi} - 1 \quad (2.76)$$

This condition is only valid in 1D geometry, and does not consider transverse dynamics which is in fact crucial for electron trapping in multidimensional plasma wakes. To derive a more general trapping condition [49][50], which takes into account both the transverse and longitudinal motion in a general electromagnetic wave, we start from the momentum equation written in the potential form:

$$\frac{d\mathbf{p}}{dt} = q \left(-\nabla\phi - \frac{\partial\mathbf{A}}{\partial t} + \mathbf{v}_\phi \times \nabla \times \mathbf{A} \right). \quad (2.77)$$

We write the triple product in Feynman notation as $\mathbf{v} \times \nabla \times \mathbf{A} = \nabla_A (\mathbf{A} \cdot \mathbf{v}_\phi) (\frac{\mathbf{v}_\phi}{c} \cdot \nabla) \mathbf{A}$, where the subscript of the gradient means the derivatives only apply to \mathbf{A} . Rearranging, we obtain an evolution equation for the generalized momentum:

$$\frac{d(\mathbf{p} + q\mathbf{A})}{dt} = -q\nabla\phi + q(\mathbf{v}_\phi \cdot \nabla) \mathbf{A}. \quad (2.78)$$

We now perform the change of variable $\xi = v_\phi t - z$ and separate the transverse component from the longitudinal component of the equation of motion, and obtain:

$$\left(\mathbf{v}_\perp \cdot \nabla_\perp + (v_\phi - v_z) \frac{\partial}{\partial \xi} \right) (\mathbf{p}_\perp + q\mathbf{A}_\perp) = -q\nabla_\perp \phi + q\nabla_{\perp,A} (\mathbf{A} \cdot \mathbf{v}), \quad (2.79)$$

$$\left(\mathbf{v}_\perp \cdot \nabla_\perp + (v_\phi - v_z) \frac{\partial}{\partial \xi} \right) (p_z + qA_z) = -q \frac{\partial\phi}{\partial\xi} - q\mathbf{v} \cdot \frac{\partial\mathbf{A}}{\partial\xi}. \quad (2.80)$$

We apply the same change of variable to the energy equation:

$$\begin{aligned} \frac{d}{dt}(\gamma mc^2) &= q\mathbf{v} \cdot \left(\nabla\phi + \frac{\partial\mathbf{A}}{\partial t} \right) \rightarrow \\ &\rightarrow \left(\mathbf{v}_\perp \cdot \nabla_\perp + (v_\phi - v_z) \frac{\partial}{\partial \xi} \right) (\gamma mc^2) = -q \left(\frac{\partial\phi}{\partial\xi} + \mathbf{v}_\perp \cdot \nabla_\perp \right) - q\mathbf{v} \cdot \frac{\partial\mathbf{A}}{\partial\xi}. \end{aligned} \quad (2.81)$$

Taking the scalar potential to the LHS and subtracting Eq. 2.81 from Eq. 2.79 we find that in the co-moving frame that the quantity:

$$\gamma mc^2 - v_\phi p_z + q(\phi - v_\phi A_z) = \mathcal{H} - v_\phi \mathcal{P}_z = \text{cost}, \quad (2.82)$$

is a constant of motion. Here the \mathcal{H} is the Hamiltonian of the charged particle and \mathcal{P}_z is the canonical momentum. Now we move to dimensionless quantities and define $\lambda = \gamma_0 - v_\phi p_{x0}$ and $\psi_0 = -(\phi - v_\phi A_z)$ as electron's initial condition for the momentum and the potentials, and look for a solution for the longitudinal momentum. Rearranging and squaring both sides of Eq. 2.82 we obtain

$$[1 - v_\phi^2]p_z^2 - 2v_\phi[\lambda + \delta\psi]p_z + [1 + p_\perp^2 - (\lambda + \delta\psi)^2] = 0, \quad (2.83)$$

where we used $\gamma^2 = 1 + p_\perp^2 + p_z^2$. Eq. 2.83 is a second order algebraic equation which has two distinct real roots for $v_z \neq v_\phi$. It can be directly related to the equation for γ and for $v_z - v_\phi$, in order to study the trapping condition.

We eventually obtain:

$$p_z = \frac{1 + p_\perp^2 - (\lambda + \delta\psi)^2}{v_\phi(\lambda + \delta\psi) \mp \sqrt{(\lambda + \delta\psi)^2 - (1 - v_\phi^2)(1 + p_\perp^2)}}, \quad (2.84)$$

$$\gamma = \frac{v_\phi(1 + p_\perp^2) \mp (\lambda + \delta\psi)\sqrt{(\lambda + \delta\psi)^2 - (1 - v_\phi^2)(1 + p_\perp^2)}}{v_\phi(\lambda + \delta\psi) \mp \sqrt{(\lambda + \delta\psi)^2 - (1 - v_\phi^2)(1 + p_\perp^2)}}, \quad (2.85)$$

$$v_z - v_\phi = |v_z - v_\phi| \left[\frac{-|v_z - v_\phi| \pm v_\phi(1 - v_z v_\phi)}{v_\phi(1 - v_z^2) \mp (1 - v_z v_\phi)|v_z - v_\phi|} \right], \quad (2.86)$$

where the term between square brackets must be ± 1 , its sign depending on whether the particle is trapped in the plasma wave, $v_z > v_\phi$, or it is not, $v_z < v_\phi$.

The occurrence of trapping arises when $v_z = v_\phi$, and this condition determines that the two real roots of Eq. 2.83 are coincident: we can get the following relationship rearranging Eqs. 2.84 and 2.85, leading to a trapping condition in terms of energy in a multidimensional plasma wake:

$$p_z = \frac{1 + p_{\perp}^2 - (\lambda + \delta\psi)^2}{v_{\phi}(\lambda + \delta\psi)}, \quad (2.87)$$

$$\gamma = \frac{1 + p_{\perp}^2}{\lambda + \delta\psi} \rightarrow \lambda + \delta\psi = \frac{\gamma}{\gamma_{\phi}^2}, \quad (2.88)$$

where $\frac{\gamma}{\gamma_{\phi}} = \sqrt{\frac{1-v_{\phi}^2}{1-v_{\phi}^2-v_{\perp}^2}}$. If $v_{\perp} = 0$ and change back to dimensional equation we find again the 1D trapping condition Eq. 2.76.

Eq. 2.88 basically states that the onset of trapping for a plasma electron depends on the potential and on the ratio between particle energy and wake energy: the potential depends directly on the driver beam, i.e. laser intensity or electron bunch charge, and so does the wake energy.

In the case of laser wake-field schemes the phase velocity of the plasma wave corresponds to the group velocity of the laser, which is $v_{g,L} < c$. In Eq. 2.88 we see that the dominant term is therefore the transverse component of the Lorentz factor, i.e. the dimensionless laser parameter a_0 . If we raise the laser intensity over a certain value, namely $a_0 > 1$ [51], Wave-breaking occurs, and the background electrons are massively trapped into the plasma wake.

Instead, in the case of an electron beam driver the phase velocity of the plasma wave is bounded to the propagation velocity of the beam, which is $v_b \sim c$. The electrons in front of the driver feel its electric field and are radially pushed off-axis, leading to the formation of an ion cavity in the wake of the driver. When the electrons are eventually pulled back by the ion space charge force, they get a very high transverse momentum, but not enough to get trapped because $\gamma_{\phi} \rightarrow \infty$. The plasma electrons cannot overcome the phase velocity of the wake, and therefore they only accumulate at the back of the ion bubble, leading to the characteristic density spike.

A few methods have been proposed to seed self-injection also for beam driven plasma

acceleration schemes [54][55]. In Chapter 4 we will introduce the one that uses ionization to directly inject electrons inside the plasma wake, avoiding Wave-breaking.

Chapter 3

Numerical tools

3.1 Numerical Plasma and Particle In Cell method

We have shown in Section 2.1 how to describe the dynamics of a plasma via the Vlasov-Maxwell set of equations. We have also mentioned how it generally has no analytical solution but for very simple and symmetric problems. Besides, we said that even numerical solutions present issues concerning computational time requirements, for we should solve the Vlasov-Maxwell equations using finite differences on a Eulerian grid in phase space.

In the general 3D case the plasma phase space is six-dimensional, and therefore the number of grid points required for the simulation scales as n^6 , being n the linear dimension of the computational grid. It appears immediately how even with a coarse grid, with respect to typical plasma acceleration simulations, having ~ 100 grid points, the memory required would reach $\sim \text{TB}$ level.

Besides, it is possible that a large volume of the 6D computational grid is wasted [56], as we can see for a simple 1d1v case in Fig. 3.1 a), where the shaded area represents the region of phase space occupied by plasma particles, i.e. where the distribution function is essentially non-zero.

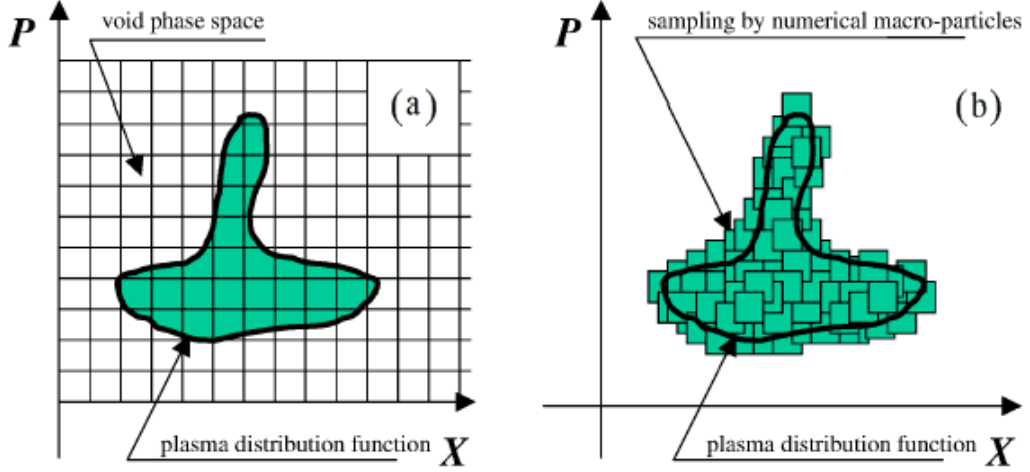


Figure 3.1. Numerical plasma simulations: a) solution of the Vlasov-Maxwell Equation using a Eulerian grid in the phase space; b) PIC method, following the dynamics of the distribution function along the characteristics of the Vlasov-Maxwell equations [56]

The area empty of plasma particles has to be kept in memory as a part of numerical arrays composing the Eulerian grid, and it has to be processed when solving the Vlasov Maxwell equations, which leads to an inefficient use of computational power. There is another, currently more computationally effective, method to solve the Vlasov equation, namely the *Particle In Cell* method[57][58]. The basic theoretical model underlying PIC method is provided by the Vlasov-Maxwell system in Lagrangian form, where the Vlasov equation, for each plasma species, is represented by the equation of motion of a finite number of particles and the distribution function is defined in the *Klimontovich delta – like formalism* [59], by:

$$f(\mathbf{r}, \mathbf{p}, t) = \sum_n^{N_s} \delta[\mathbf{r} - \mathbf{r}_n(t)] \delta[\mathbf{p} - \mathbf{p}_n(t)]. \quad (3.1)$$

In numerical PIC schemes, the following main computational approximations are

applied:

1. The N_s real plasma particles are replaced by a subset of $\mathcal{N}_s \ll N_s$ numerical particles, or *macro-particles*, each containing a fixed number of real particles given by the ratio (a weight) $W_s = N_s/\mathcal{N}_s$. Correspondingly, each macro-particle has larger charge $Q_s = W_s q_s$ and mass $M_s = m_s W_s$ than a real particle, but the total mass and charge of numerical and real plasma are the same.

The macro-particle weight is a conserved quantity during the particle motion. Moreover, since the particle equation of motion in a collisionless systems depends only on the ratio $q_s = m_s$ and $Q_s/M_s = q_s/m_s$, the macro-particle weights has no dynamical relevance at all.

It is however of paramount importance for accuracy the macro-particle number \mathcal{N}_s is sufficiently large, allowing also to reduce discreteness effects (numerical noise) and to improve statistical sampling.

2. A finite dimensional computational grid in space and time is introduced, to integrate the particle motion and the Maxwell equations. The total number of grid points in a Cartesian computational box of size $V = L_x L_y L_z$ is denoted by $N_g = N_x N_y N_z$, giving a cell volume size $V = \Delta_x \Delta_y \Delta_z$, where, along each coordinate axis, $\Delta_c = Lc/Nc$ for $c = x, y, z$, respectively.

Field variables, $(\mathbf{E}, \mathbf{B}, \rho, \mathbf{J})$, all depending on the (\mathbf{r}, t) continuous coordinates, are then discretized on the grid, and space derivatives are approximated by two-point centred finite differences in second order schemes, or by four-point centred finite differences in fourth order Runge-Kutta integration schemes.

3. In the Klimontovich distribution function Eq. 3.2 the $\delta(\mathbf{r} - \mathbf{r}_n(t))$ functions are replaced by smoother *shape functions*, here denoted in short by $\hat{S}_\Delta(\mathbf{r} - \mathbf{r}_n(t))$, taking non-zero values around a particle position on a spatial range with size Δ related to the cell computational grid sizes. The shape functions are designed to reduce particle granularity effects and two-particle (electrostatic) interactions over this grid-related characteristic scale length. We have then:

$$f(\mathbf{r}, \mathbf{p}, t) = \sum_n^{N_s} \hat{S}_\Delta[\mathbf{r} - \mathbf{r}_n(t)] \delta[\mathbf{p} - \mathbf{p}_n(t)], \quad (3.2)$$

where \mathbf{p} coordinate is still represented by a Dirac- δ function.

In Cartesian coordinate $\mathbf{r} = (x, y, z)$, \hat{S}_Δ is represented by tensor product of one dimensional shape functions:

$$\hat{S}_\Delta[\mathbf{r} - \mathbf{r}_n(t)] \equiv \frac{1}{\Delta x \Delta y \Delta z} S[x - x_n(t)] S[y - y_n(t)] S[z - z_n(t)], \quad (3.3)$$

and macro-particle density, for each species, is then defined by:

$$n^{mc}(\mathbf{r}, t) = \frac{1}{\Delta V} \sum_n \hat{S}[\mathbf{r} - \mathbf{r}_n(t)]. \quad (3.4)$$

To relate physical to macro-particles density, one takes into account that the weights $W_s = N_s / \mathcal{N}_s$, that can be expressed in terms of mean particle and macro-particle densities by:

$$W_s = \bar{n}_s / \bar{n}^{mc}, \quad \bar{n}_s = N_s / V, \quad \bar{n}_s^{mc} = \mathcal{N}_s / V. \quad (3.5)$$

For each species, the physical density normalized to the reference initial density \bar{n} is then computed using macro-particles by:

$$\tilde{n}(\mathbf{r}, t) = n(\mathbf{r}, t)/\bar{n} = \sum_n w \hat{S}[\mathbf{r} - \mathbf{r}_n(t)], \quad (3.6)$$

where the macro-particle weight w has been introduced:

$$w = \frac{1}{n^{mc} \Delta V} = \frac{1}{m_{pc}}, \quad (3.7)$$

which is the inverse of the number of macro-particles of a given species per grid cell defined in the initial conditions. In this way, gradients in the initial density distribution can be accounted for only by using variable macro-particle numbers m_{pc} , which is usually a difficult task in multidimensional case where m_{pc} , are discrete small numbers.

In ALaDyn code this difficulty is faced by introducing particle dependent weights w_n , with sizes related to the particle positions in the initial conditions, in such a way density gradients are reproduced yet using small macro-particle numbers.

3.1.1 Particle-grid connection

Each one-dimensional shape function, i.e. $S[(x - x_p)/h]$, where h is the cell size, is a piecewise polynomial (a spline) of some order r in the $\zeta = (x - x_p)/h$ dimensionless coordinate. For a given x_p particle position, it takes non-zero values on a compact support around the $x = x_p$, $\zeta = 0$ point where the maximum is located. Relevant properties are:

1. *translational invariance*

Since each shape function depends only on ζ , it is invariant under a coordinate shift of the system $x \rightarrow x + L$, $x_p \rightarrow x_p + L$, assuring then momentum conservation;

2. *partition of unity*:

$$S(\zeta) \geq 0, \quad \int S(\zeta) d\zeta = 1; \quad (3.8)$$

3. *smoothness*

For given r^{th} polynomial order, a spline has smoothness class C^{r-1} ;

4. *local charge conservation*

One-dimensional density for each species is defined by:

$$n(x, t) = \sum_n^N w_n S[(x - x_n(t))/h], \quad (3.9)$$

where particle dependent weights are also considered.

To check for continuity equation, it is sufficient to consider the density given by just one particle shape function. It satisfies exactly the relation:

$$\frac{\partial S[(x - x_n(t))/h]}{\partial t} = -\frac{\partial S[(x - x_n(t))/h]}{\partial x} \frac{dx_n(t)}{dt}, \quad (3.10)$$

leading to:

$$\frac{\partial n(x, t)}{\partial t} = \frac{\partial}{\partial x} \sum_n w_n v_n S[(x - x_n(t))/h], \quad (3.11)$$

because of the linearity of Eq. 3.9.

The most widely used shape functions are low order splines: linear ($r = 1$) and quadratic ($r = 2$). Higher order polynomials are too expensive since computation complexity for each particle increases as $(r+1)^3$ in 3D current deposition procedures.

Linear splines are defined by:

$$\hat{L}(\zeta) = 1 - |\zeta|, \quad |\zeta| \leq 1, \quad (3.12)$$

resulting by joining two linear polynomials at the $\zeta = 0$ branch point.

Quadratic splines are defined joining three quadratic polynomials:

$$\hat{Q}^0(\zeta) = 3/4 - \zeta^2, \quad -1/2 \leq \zeta \leq 1/2, \quad (3.13)$$

$$\hat{Q}^+(\zeta) = \frac{1}{2}(3/2 - \zeta)^2, \quad 1/2 \leq \zeta \leq 3/2, \quad (3.14)$$

$$\hat{Q}^-(\zeta) = \hat{Q}^+(-\zeta), \quad -3/2 \leq \zeta \leq -1/2, \quad (3.15)$$

which is continuous and differentiable at the branch points $x - x_p = \pm h/2$ and $x - x_p = \pm 3h/2$. Other examples of B-spline used to define the shape functions of the macro-particles are presented in Fig. 3.2.

In PIC codes, shape functions are discretized on the same grid used for fields, allowing to relate point-particle coordinates to grid projected fields. Grid defined splines are usually referred to as *B*-splines.

The linear *B*-spline, for a particle inside a $C_{i+1/2} = [x_i, x_{i+1}]$ cell, in terms of the $\zeta = (x_p - x_i)/h$ relative coordinate takes values at the $j = i, i + 1$ grid points

$$\hat{L}_i = 1 - \zeta, \quad \hat{L}_{i+1}(\zeta) = \zeta 1. \quad (3.16)$$

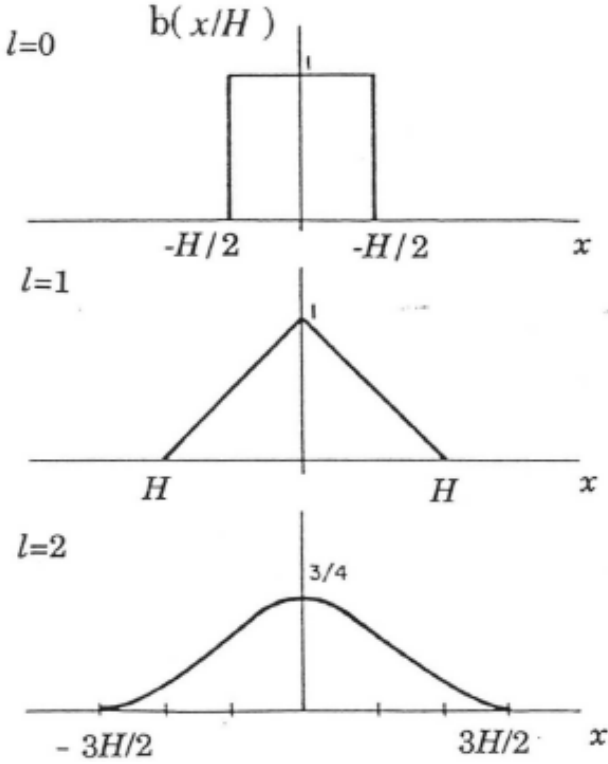


Figure 3.2. 0^{th} , 1^{st} and 2^{nd} order splines, where l represents the spline order and the length scale is indicated by H [60]

Likewise, a quadratic B -spline, for a particle located in the $C_i = [x_{i-1/2}, x_{i+1/2}]$ cell, takes values at the $j = i - 1, i, i + 1$ grid points

$$\hat{Q}_i = 3/4 - \zeta_i^2, \quad \hat{Q}_{i-1} = \frac{1}{2}(3/2 - \zeta_i)^2, \quad \hat{Q}_{i+1} = \frac{1}{2}(3/2 + \zeta_i)^2, \quad (3.17)$$

where now the relative coordinates have been defined as $\zeta_i = (x_i - x_p)/h$, $|\zeta_i| \leq 1/2$. Representing point particles in a finite dimensional grid via discretized shape functions entails relevant, yet unsolved, numerical problems. In fact, whereas finite dimensional integration of particle and field equations produces numerical errors which can be controlled and then reduced by increasing the integration scheme order and by grid refinement, spline based representation of particles on a grid entails

deeper problems, affecting the structural properties and the conservation laws of the Vlasov-Maxwell system.

The following list covers some of these problems, already considered in PIC classical papers [61][62]:

1. B -splines are defined on a compact support and have low smoothness class.

Fourier spectra are then necessarily contaminated by an infinite set of high frequency modes (aliasing), producing anomalous heating, and even grid instability, during particle motion. These numerical effects are often referred to as *numerical collisionality*.

2. Discretized shape functions $S_j[(x_i - x_p)/h]$ depend not only on the $\zeta = (x - x_p)/h$ difference but also on the i -th cell where a particle resides, $\zeta \rightarrow \zeta_i$.

As a consequence, translational invariance and thus momentum conservation get lost.

3. The dependence of shape function values on the cell where a particle resides, when coupled to discretized space-time differentiation, leads to a failure of local charge conservation. More precisely:

(a) - If a particle, during one timestep motion, remains inside a cell, numerical continuity equation is exactly satisfied;

(b) - If a particle, during one timestep motion, instead crosses a cell, then continuity equation fails. The size of the resulting error is problem dependent, of course, since depends only on the number of particles crossing a cell during particle motion.

3.1.2 FDTD Yee module in PIC numerical integration

Space-time discretization usually introduced in PIC codes to integrate field and particle equations is provided by the Yee [63] module on a staggered grid (Fig.3.3), where time and space derivatives are approximated by second order two-point centred finite differences. The overall procedure is denoted as *Finite Difference Time Domain* (FDTD).

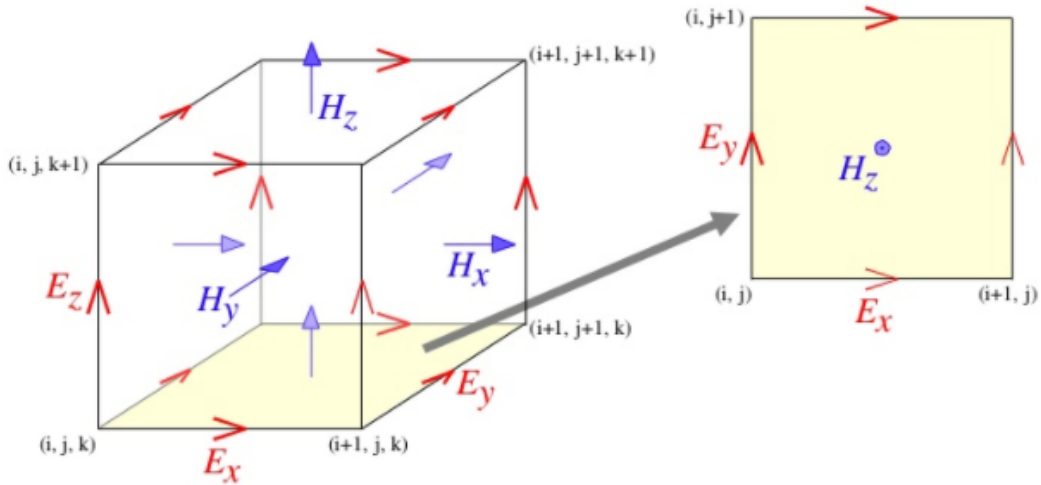


Figure 3.3. 3D Yee grid, [cite Yee]

Centred finite differences entail numerical truncation error of even order in space and time grid sizes, thus introducing only dispersive numerical error. Conservative properties of the system and time reversal are then preserved by a FDTD schemes. Finite differences on a staggered grid is more than a numerical technique among others. It turns out to be appropriate for Vlasov-Maxwell system (but not necessarily for other systems, like a fluid system even when it is derived from the Vlasov equation), essentially because of the Hamiltonian structure of the Vlasov-Maxwell system, where fields (\mathbf{E}, \mathbf{B}) are conjugate-pair variable with respect to the rot $\nabla \times$ operator. Grid collocation in FDTD schemes takes into account field vector structure in a sense

1. *Scalar fields* (ρ, ϕ) are discretized at the grid nodes (cell boundaries in 1D cells and corners in 3D cubic cell) $[x_i, y_j, z_k]$. Let then denote by $g_0 = [i, j, k]$ the corresponding 3D grid index.
2. *Polar vectors* \mathbf{P} like (\mathbf{E}, \mathbf{J}) fields and gradients of scalar fields, are discretized at cell centres of the one-dimensional grid along the proper longitudinal direction, and at the cell boundaries along the perpendicular directions. For example, E_x and J_x are discretized at the grid points indexed by $g_x \equiv [i + 1/2, j, k]$, and in similar way for other vector components following this rule.
3. *Axial vectors*, like the magnetic field and rot of polar vector $\nabla \times \mathbf{P}$ are collocated at the complementary or dual grid, that is $B_x[i, j + 1/2, k + 1/2]$ is collocated at the centre of the (y, z) cell perpendicular to the field x direction, and at the cell boundaries along the proper longitudinal direction, and so forth for other components. In the case of the B_x component, grid indexes are denoted as $g_{y,z} = [i, j + 1/2, k + 1/2]$ and likewise for other field components.

In this way, staggering allows to relate the x -derivative collocated at the i -th point, using a variable located at the cell centre $(i \pm 1/2)$ -th points

$$g_i = [\mathcal{D}_x f]_i = \frac{f_{i+1/2} - f_{i-1/2}}{\Delta x}, \quad (3.18)$$

and by converse, the f_i derivative returns the value of the dual g field

$$f_{i+1/2} = [\mathcal{D}_x g]_{i+1/2} = \frac{g_{i+1} - g_i}{\Delta x}. \quad (3.19)$$

In both cases, $[\mathcal{D}_x]$ approximates the one dimensional x derivative with leading

truncation error $O(\Delta x)^2$. This allows, in particular, for variables $f_{i+1/2}$ located at cell centres to evaluate its values at the cell boundaries to within the same approximation order by a mid-point interpolation $f_i = (f_{i+1/2} + f_{i-1/2})/2$.

Along similar lines, a staggered time grid $t^n = n\Delta t$ and $t^{n+1/2} = t^n + \Delta t/2$ is introduced in FDTD module, connecting conjugate-pair variables $[\mathbf{x}, \mathbf{p}]$ and $[\mathbf{E}, \mathbf{B}]$. Time derivatives on a staggered grid follows the same scheme adopted for space derivatives, that is, for any pair of field variables (f, g) , one has

$$g^n = [\mathcal{D}_t f]^n = \frac{f^{n+1/2} - f^{n-1/2}}{\Delta t}, \quad (3.20)$$

and by converse for the $[\mathcal{D}_t g]^{n+1/2}$ derivative.

3.1.3 PIC numerical integration of particle and field equation

In the ALaDyn PIC code, a one-step $t^n \rightarrow t^{n+1}$ integration cycle of particles and fields is detailed by the following main computational steps, resumed in Fig.3.4:

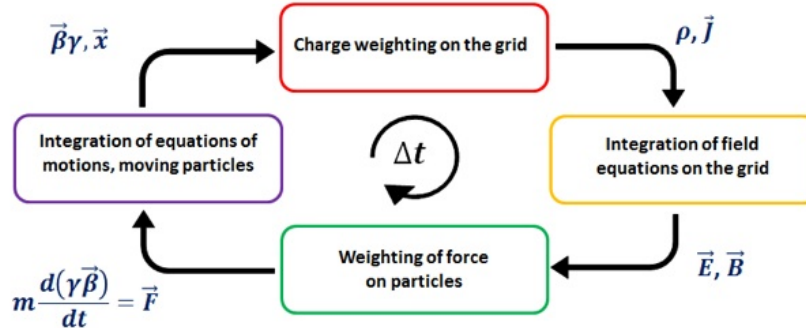


Figure 3.4. Time loop in a PIC code

1. At the initial t^n time level, grid collocated fields $[\mathbf{E}^n(\mathbf{x}_g), \mathbf{B}^n(\mathbf{x}_g)]$ enter as known quantities resulting from previous integration step. Likewise, particle

coordinates enter at time index \mathbf{x}^n and $\mathbf{p}^{n-1/2}$, respectively.

The first computational step is then devoted to assign grid fields to the particle position \mathbf{x}^n using shape functions. In synthetic notations, one has:

$$\mathbf{E}^n(\mathbf{x}_p) = \sum_g \hat{S}[\mathbf{x}_g - \mathbf{x}_p] \mathbf{E}^n(\mathbf{x}_g), \quad (3.21)$$

$$\mathbf{B}^n(\mathbf{x}_p) = \sum_g \hat{S}[\mathbf{x}_g - \mathbf{x}_p] \mathbf{B}^n(\mathbf{x}_g), \quad (3.22)$$

(3.23)

where for fixed particle positions, the sum extends for all grid points where shape functions take non zero values.

2. For given fields and particle positions at time t^n , one-step update of particle momentum is the solution of the algebraic equation (particle index omitted for brevity):

$$\mathbf{p}^{n+1/2} = \mathbf{p}^{n-1/2} + \alpha \Delta t [\mathbf{E}^n + \mathbf{v}^n \times \mathbf{B}^n], \quad (3.24)$$

and the update of particle positions is then evaluated by:

$$\mathbf{x}^{n+1} = \mathbf{x}^n + \Delta t \mathbf{v}^{n+1/2}, \quad (3.25)$$

being $\mathbf{v}^{n+1/2} = \mathbf{p}^{n+1/2} / \gamma^{n+1/2}$.

Here particles and field variables are in dimensionless form. The α constant in the Lorentz force is the q/m ratio with size depending on the adopted normalization units.

The momentum update Eq. 3.24 has an implicit structure, since $\mathbf{v}^n = \mathbf{p}^n/\gamma^n$ on the RHS is not given and depends also on $\mathbf{p}^{n+1/2}$. However, the equation can be reduced to a solvable explicit form using Boris pusher algorithm [64] (Appendix 3) or variants of this scheme.

In the ALaDyn code the mod point momentum $\mathbf{p}^n = (\mathbf{p}^{n+1/2} + \mathbf{p}^{n-1/2})/2$ is first introduced and Eq. 3.24 is then reformulated as:

$$\mathbf{p}^n = \mathbf{p}^{n-1/2} + \beta[\mathbf{E}^n + \mathbf{v}^n \times \mathbf{B}^n], \quad (3.26)$$

being $\beta = \alpha\Delta t/2$, $\mathbf{v}^n = \mathbf{p}^n\gamma^n$ and $\gamma^n = \gamma(\mathbf{p}^n)$. As algebraic equation in the $\mathbf{p} = \mathbf{p}^n$ and $\gamma = \gamma^n$ unknowns, the momentum update Eq. 3.26:

$$\mathbf{p}^n = \mathbf{a} + \frac{\mathbf{p}^n}{\gamma} \times \mathbf{b}, \quad (3.27)$$

where:

$$\mathbf{a} = \mathbf{p}^{n-1/2} + \beta\mathbf{E}^n/2, \quad \mathbf{b} = \beta\mathbf{B}^n, \quad (3.28)$$

act as known coefficients.

By algebraic manipulation, the solution can be finally expressed in explicit form:

$$\mathbf{p} = \frac{[\gamma^2\mathbf{a} + \gamma(\mathbf{a} \times \mathbf{b}) + \mathbf{b}(\mathbf{a} \cdot \mathbf{b})]}{\gamma^2 + b^2}, \quad (3.29)$$

where the $\gamma = \gamma^n$ quantity is solution of the quadratic algebraic equation:

$$\gamma^2(\gamma^2 + b^2) - \gamma^2(1 + a^2) - b^2 - (\mathbf{a} \cdot \mathbf{b})^2 = 0. \quad (3.30)$$

The positive roots of Eq.3.30 are given by:

$$\gamma^2 = \frac{1}{2}[\gamma_0^2 - b^2 + \sqrt{(\gamma_0^2 - b^2)^2 + 4(b^2 - (\mathbf{a} \cdot \mathbf{b})^2)}], \quad (3.31)$$

where $\gamma_0 = 1 + |\mathbf{a}|^2$ is the approximation used in the Boris pusher.

For a given \mathbf{p}^n , the updated particle momentum is evaluated by $\mathbf{p}^{n+1/2} = 2\mathbf{p}^n - \mathbf{p}^{n-1/2}$ allowing to advance particle positions by:

$$\mathbf{x}^{n+1} = \mathbf{x}^n \Delta t \mathbf{v}^{n+1/2}, \quad \mathbf{v}^{n+1/2} = \frac{\mathbf{p}^{n+1/2}}{\gamma^{n+1/2}}. \quad (3.32)$$

3. To perform one step integration of (\mathbf{E}, \mathbf{B}) fields in Maxwell equations, the grid defined current density $\mathbf{J}^{n+1/2}$ based on particle velocity $\mathbf{v}^{n+1/2}$ and particle positions $(\mathbf{x}^n, \mathbf{x}^{n+1})$ must be evaluated first.

This step is usually the most time consuming and the most problematic due to the failure of local charge conservation, as discussed in previous sections.

For one species particle with charge $\tilde{q} = q/e$ expressed in units of electron charge ($\tilde{q} = -1$ for electron species), the current density in dimensionless form collocated at the proper space-time grid points, is defined by:

$$\mathbf{J}_g^{n+1/2} = \tilde{q} \sum w_p \mathbf{v}_p^{n+1/2} (\hat{S}_g[\mathbf{x}_g - \mathbf{x}_p^n] + \hat{S}_g[\mathbf{x}_g - \mathbf{x}_p^{n+1}]) / 2, \quad (3.33)$$

where shape functions are the same used for field-particle assignments.

To have shape functions centred at time level $t^{n+1/2}$, a two-point average is

here applied. A variant of this formulation, with shape function evaluated at the centred $x^{n+1/2} = (x^n + x^{n+1})/2$ particle position, can be used as well.

4. Finally the (\mathbf{E}, \mathbf{B}) fields can be updated from time level t^n to t^{n+1} . Time update of Maxwell equation is given by (grid index not explicitly indicated are given using the Yee module):

$$\mathbf{B}^{n+1/2} = \mathbf{B}^{n-1/2} - \Delta t \mathcal{D} \times \mathbf{E}^n = \mathbf{B}^n - \frac{\Delta t}{2} \mathcal{D} \times \mathbf{E}^n, \quad (3.34)$$

where $\mathbf{B}^{n-1/2} = 2\mathbf{B}^n - \mathbf{B}^{n+1/2}$ has been used in the last equality, as appropriate when \mathbf{B} is discretized at integer time levels, and by:

$$\mathbf{E}^{n+1} = \mathbf{E}^n + \Delta t [\mathcal{D} \times \mathbf{B}^{n+1/2} - \omega_p^2 \mathbf{J}^{n+1/2}], \quad (3.35)$$

where the electron plasma frequency arises from field and density normalization.

In this formulation, to recover \mathbf{B}^{n+1} at the same time level as the electric field, a third step has to be added:

$$\mathbf{B}^{n+1} = \mathbf{B}^{n+1/2} - \frac{\Delta t}{2} \mathcal{D} \times \mathbf{E}^{n+1}. \quad (3.36)$$

By error analysis, this three-step formulation of field numerical integration results to be fully equivalent to standard Leap-frog integration on time-staggered grid.

3.2 The ALaDyn Code

The Particle In Cell code we have employed for our simulations is the ALaDyn Code [37][38]. The ALaDyn Code was originally developed at University of Bologna to study the propagation and the interaction of a laser pulse with a pre-ionized plasma. The routines related to the beam-plasma interaction have been subsequently added to the main kernel in collaboration between the University of Rome, the INFN national laboratories of Frascati and the University of Rome, La Sapienza.

The ALaDyn code is a full 3D, fully relativistic PIC-code, with high flexibility even in the 1D and 2D form, successfully tested for both the laser plasma interaction and the beam plasma interaction, and is currently used for both electron acceleration simulations (LWFA and PWFA) [39] and ion acceleration [40] (TNSA).

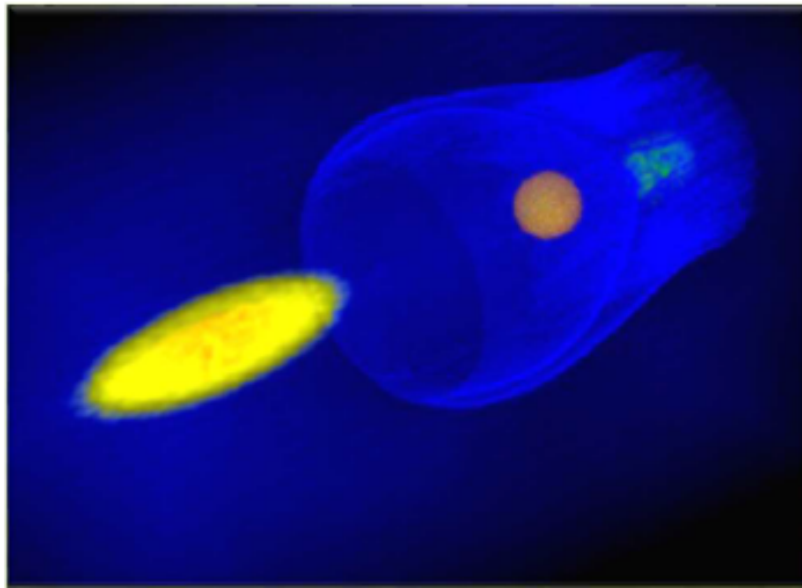


Figure 3.5. Driver beam density (light yellow), witness beam density (dark yellow) and background density (plasma wake, blue) in a 3D output obtained from Visit.

ALaDyn is equipped with high order integrating algorithm in both space and time

(RK4), and with a numerical Cherenkov radiation mitigation algorithm FDTD still under development. The charge deposition is performed with the Esirkepov deposition scheme [65] and ensures charge conservation for high order macro-particle shape functions.

The field ionization module is equipped with the ADK model [66], the BSI model [67] and the ADK modified model [68], to consider intermediate regimes between tunneling and barrier suppression ionization. A routine for the impact ionization is implemented as well. We have introduced in the code the capability to export 3D output via the interface with Visit and python routines, in order to perform both post-processing and online analysis (Fig.3.5).

ALaDyn is massively parallelized in both the longitudinal and transverse domain, and efficiently runs on both Tier-0 and small clusters.

Chapter 4

Electron trapping via ionization

4.1 Wake-Field Ionization Injection

In Section 2.3 we derived the trapping condition for the background plasma electrons in terms of the energy gained by the plasma wave (γ) and the initial conditions (ψ_i). The threshold we presented is general, but it was originally derived for the Laser driven plasma wake-field acceleration scheme[51]. It is possible to prove [52][53] that the background electrons which have radial positions close to the edge of the bubble ($r_i \sim R_b$), gain sufficient longitudinal momentum to reach the condition $v_z > v_{phi}$, where v_{phi} is the phase velocity of the plasma wave, equal to the laser group velocity. This condition corresponds to the longitudinal breaking of the plasma wave, and leads to a self-injected electron beam which is accelerated and focused inside the plasma wave.

Since $v_z > v_{phi}$ the self-injected beam propagates in the plasma wave across the accelerating region and eventually reaches the decelerating region, corresponding roughly to the centre of the bubble. The electron beam therefore starts to oscillate longitudinally, reducing its length but on the other hand increasing its energy spread to values too large for light sources applications or high energy physics.

In the Beam driven plasma acceleration scheme the phase velocity of the plasma wave corresponds to the velocity of the driving beam, which for relativistic electron beams is approximately the speed of light c . The background electrons at $r_i \sim R_b$ are accelerated to relativistic velocities but cannot overcome the velocity of the plasma wave, therefore accumulate at the back of the bubble, leading to the characteristic density spike. The trapping via longitudinal Wave-breaking is thus impossible, at least for typical accelerating distances of cm scale. In order to trap background electrons in the plasma wave it is therefore mandatory to inject them somehow directly inside the bubble.

The ionization injection method for a Beam driven scheme was initially proposed for extremely high charge driving beams [54]. The scheme implies the ionization of an initially neutral gas mixture (Li+He) via the electric field due to the driving beam charge. The low ionization potential element (Li) is required to create and sustain the plasma wave and does not play any role in the injection process. The high potential element triggers the ionization injection. As the driving beam propagates through the Li plasma it is focused by the ion column transverse forces to a size much smaller than its initial size. The driving beam space charge forces increase and eventually reach the threshold value required to ionize the first level of the He. The ionizing field of the driving beam is highly sensitive to the betatron oscillations due to the ion column forces ($E_r \propto \sigma_r^{-1}$), and its variations along the ionization and transport distance determine a large, growing emittance for the self-injected beam. The Wake-Field Ionization Injection scheme [69][70][71] avoids this inconvenient, relying only on the bubble fields to ionize and inject electrons precisely in the accelerating and focusing phase of the wake. To avoid ionization in the driving beam region, the scheme proposes to choose a dopant element which has a sufficiently high ionization potential not to be ionized by the driving beam space charge fields, but

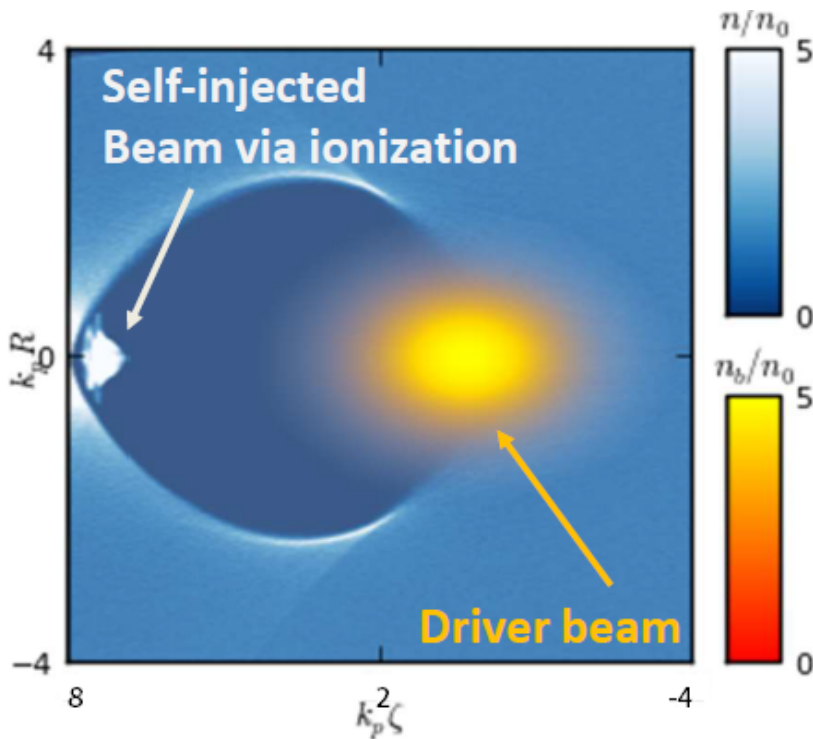


Figure 4.1. Self injected beam in the rear of the bubble via ionization.

only via the higher fields developed in the back of the bubble.

Besides, to control the injected charge and to improve the beam quality, the dopant element, and therefore the injection process, is confined in a limited region with respect to the whole accelerating chamber. This choice avoids continuous injection of electrons and along the whole transport and separates the injection from the acceleration and transport, leading to inherently short, low emittance and quasi-monochromatic trapped electron beams (Fig.4.1).

4.1.1 Ionization model

Ionization is the process of separating a bound electron from the positively charged nucleus of an atom. In the theory and simulations we will discuss in this work we will focus on the tunnelling ionization models, where the electric field superimposed

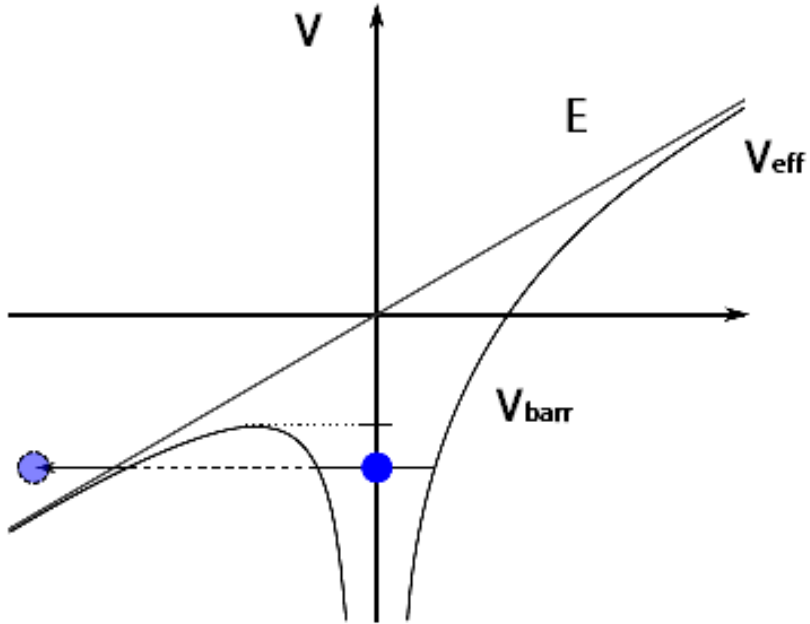


Figure 4.2. The schematic process of tunnel ionization: a field superimposed on the atom binding potential determines a finite probability for an initially bounded electron to tunnel the potential barrier and be freed [73].

on an atom is intense enough to perturb a bounded electron in such a way a finite probability of tunnelling the potential barrier develops (Fig.4.2). Several analytical models exist to study the tunnel ionization phenomenon [72], but in this work the ADK model [66] seemed particularly suitable to simulate the Wake-Field Ionization Injection since its formulas for the ionization rate is applicable for the high Z atoms employed in the Wake-Field Ionization Injection.

The ADK model links the ionization rate and probability to the intensity of the electric field superimposed on the atom, to the ionization potential of the i^{th} bound level and to the atomic number Z of the atom. The formula for the ionization rate

in a static field is:

$$W_{ADK} = \omega_a C_{n^* l^*}^2 \frac{(2l+1)(l+|m|)!}{2^{|m|}(|m|)!(l-|m|)!} \left(\frac{U_i}{2U_H} \right) \left(2 \frac{E_a}{E} \left(\frac{U_i}{U_H} \right)^{3/2} \right)^{2n^* - |m|-1} \exp \left(-\frac{2}{3} \frac{E_a}{E} \left(\frac{U_i}{U_H} \right)^{3/2}, \right) \quad (4.1)$$

where $\omega_a = \alpha^3 c / r_e = 4.13 \times 10^{16} \text{s}^{-1}$ is the atomic unit frequency, U_i is the ionization potential of the i^{th} level, and $U_H = 13.6 \text{eV}$ is the ionization potential of Hydrogen at the fundamental state. Here r_e is the classical electron radius and $\alpha = 1/137$ is the fine structure constant. The effective principal quantum number, $n^* = Z \sqrt{U_H/U_i}$ and the effective value of the orbital number l^* depend on the Z of the element.

The coefficients $C_{n^* l^*}$ can be calculated via a semi-classical approximation:

$$C_{n^* l^*}^2 = \frac{2^{2n^*}}{n^* \Gamma(n^* + l^* + 1) \Gamma(n^* - l^*)} \simeq \frac{1}{2\pi n^*} \left(\frac{4e^2}{n^{*2} - l^{*2}} \right)^{n^*} \left(\frac{n^* - l^*}{n^* + l^*} \right)^{l^* + 1/2}, \quad (4.2)$$

which can be simplified for high Z atoms, $l^* \ll n^*$, to:

$$C_{n^* l^*}^2 = \frac{1}{2\pi n^*} \left(\frac{2e}{n^*} \right)^{2n^*} \quad (4.3)$$

It has been shown [74] how the ADK formula for the ionization rate can be applied as long as the electric field acting on the atom remains below a critical value:

$$E_{CRIT} = (\sqrt{2} - 1)(U_i)^{3/2}, \quad (4.4)$$

where both the field and the ionization potential are written in atomic units, and the conversion to *SI* are $5.14 \times 10^{14} \text{V/m}$ for the electric field and 27.2eV for the ionization potential.

In tab.4.1 are shown the ionization potentials and the critical fields for N, Ne, Ar. The ADK model is strictly valid in the whole wake volume for most of the elements, but in the zone where trajectory crossing of the background electrons occurs, as

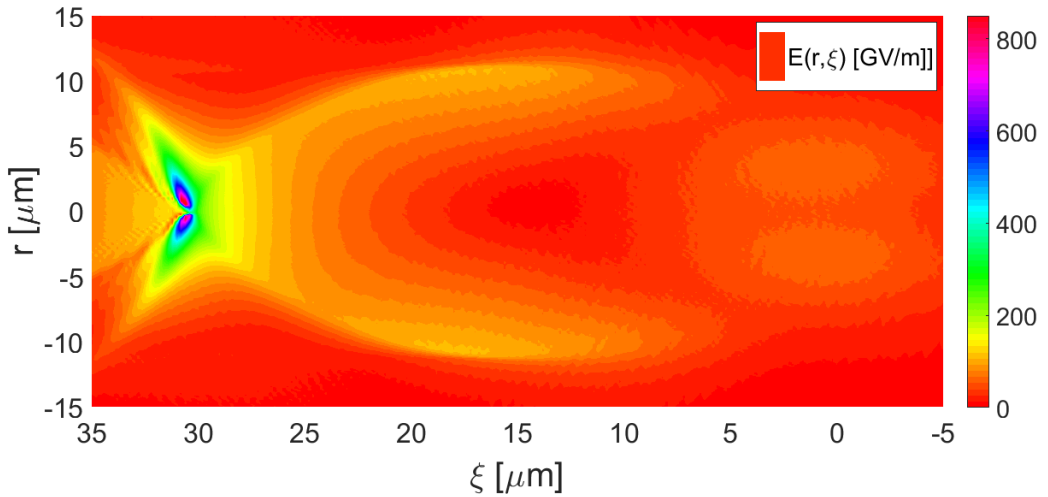


Figure 4.3. The modulus of the electric field as a function of r and ξ . The maximum intensity is close to 900 GV/m at the back of the bubble (blue to violet area).

one can see in Fig. 4.3. In that region, where the background electrons accumulate forming the typical spike, a different ionization model is required. Nevertheless, as we will explain later in the trapping section, the zone where the field intensity exceeds the critical field resides outside of the trapping region. The electrons which are born in that region are not trapped, and do not contribute to the self-injected beam properties.

From a numerical point of view, the ionization module in a PIC code works basically as a Monte Carlo algorithm. Every time-step it calculates the ionization rate for a given atom, given the local electric field and the atom ionization parameters (ionization potential and charge state). The electron ionization probability is therefore calculated as $P(t) = 1 - \exp(W_{ADK}(t)\Delta t)$, where Δt is the simulation time-step (Fig. 4.4). The code generates a random number p with a uniform distribution between 0 and 1, and compares it to the ionization probability: if $p < P(t)$ the atom is set to be ionized and the ionized electron is injected into the background with a thermal energy equal to the one of the atom it has been expelled from. On the

Table 4.1. Ionization Potentials for N, Ar, Ne

Species	Z	Ionization Potential (eV)	Critical Field (GV/m)
N^{1+}	1	14.53	83.13
N^{2+}	2	29.6	241.7
N^{3+}	3	47.45	490.56
N^{4+}	4	77.47	964.5
Ar^{1+}	1	15.76	93.9
Ar^{2+}	2	27.62	217.86
Ar^{3+}	3	40.74	390.27
Ar^{4+}	4	59.81	694.22
Ar^{5+}	5	75.02	975.21
Ne^{1+}	1	21.56	150.25
Ne^{2+}	2	40.96	393.44
Ne^{3+}	3	63.45	758.55

other hand, if $p > P(t)$ the atom is not ionized and preserves its charge state until the next evaluation.

4.1.2 Ionization injection trapping condition

We derived in Section 2.3 the trapping condition for a background plasma electron to be captured by the plasma wake having a phase velocity $v_\phi < c$. In the Wake-Field Ionization Injection scheme the phase velocity of the wake, driven by an ultra-relativistic electron beam, is approximately equal to the speed of light. A freed electron, as we have seen speaking of the tunnel ionization models, is created roughly at rest by the electric field of the plasma wake in a region close to back of

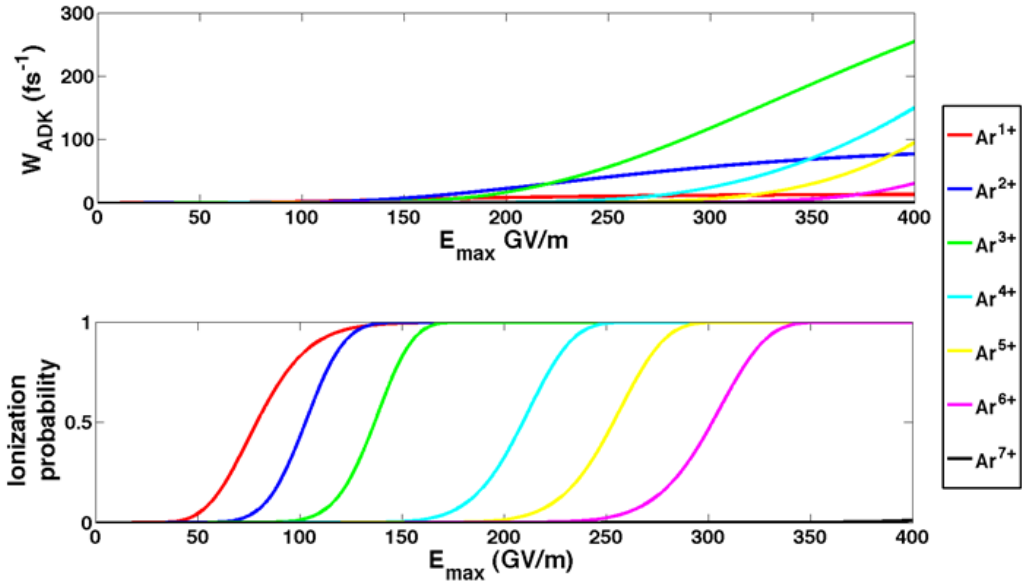


Figure 4.4. ADK ionization rate and ionization probability for Ar as a function of the superimposed electric field.

the bubble, where the accelerating electric field reaches its highest values. Since the electrons start at rest, $\gamma_i - p_{z,i} = 1$ and the pseudo-potential ψ_i depends on the ionization location $\xi_i = \xi_{ion}$. The trapped electron slips in the bubble while it gains energy from the wake-field, and eventually reaches a velocity $\beta_z \sim 1$ in a position ξ_f , corresponding to a value of the pseudo-potential ψ_f . In this situation, the Eq. 2.88 becomes:

$$1 - \psi_i = -\psi_f \quad (4.5)$$

which is the trapping condition for an electron born at rest inside the plasma wake. Equation 4.5 states that only the electrons whose displacement inside the bubble satisfies $\Delta\psi = -1$ gain sufficient longitudinal momentum to be trapped and co-propagate with the plasma wave. In other terms, an ionized electron cannot reach any position inside the bubble, but only the ones corresponding to $\Delta\psi = -1$.

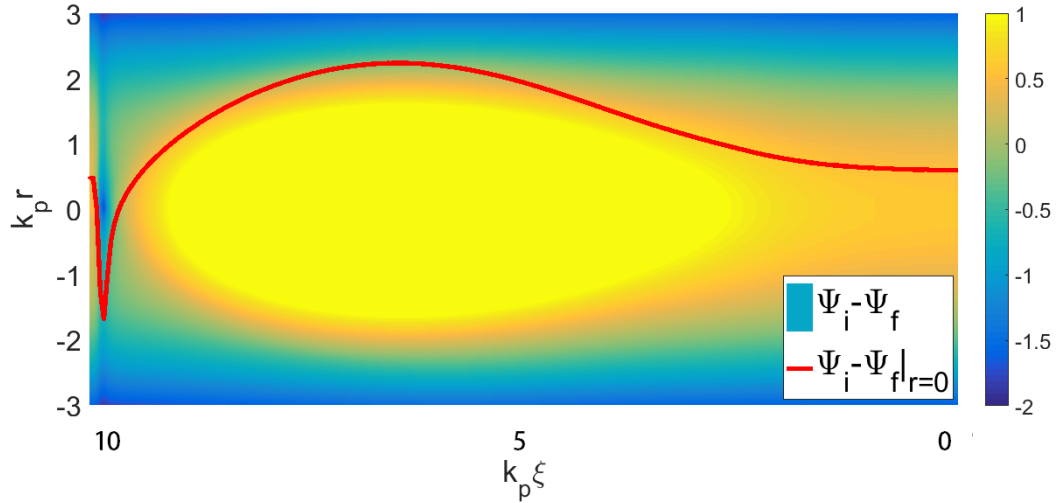


Figure 4.5. Pseudo-potential as a function of r and ξ . All the electron whose displacement correspond to a variation in ψ equal to -1 , and resides inside the focusing and accelerating volume of the wake, is trapped.

Things change if the trapping condition is reached outside the bubble: the field configuration is different, since the accelerating field turns to decelerating and the focusing field to defocusing. Electrons which do not satisfy Eq. 4.5 inside the bubble are not trapped and are lost in the plasma background.

Given this phenomenological consideration, we show in Fig. 4.5 the $-\Delta\psi$ as a function of r and ξ where we have chosen as final electron position ξ_f the one corresponding to the accelerating field turning to decelerating.

The equations we derived in Section 2.2.3 and the scaling laws obtained for the blowout radius and the accelerating field are now used to derive a simplified threshold for the ionization injection to occur in term of driving beam current. In a simplified, yet useful, 1D scaling, the pseudo-potential $\psi(\xi)$ is related to the accelerating field by $E_z = -\partial\psi/\partial\xi$, and its maximum value ψ_m is reached at the centre of the blowout cavity $\xi_i \simeq r_m$, where E_z changes from decelerating to accelerating and the blowout

radius reaches its maximum $r_b = r_m$. The minimum value ψ_{min} is reached at the very back of the bubble $\xi_f \simeq 2r_m$, where the background electron trajectories cross and the density spike is developed. Therefore the maximum potential difference an ionized electron can experience is given by $\Delta\psi = -\int_{\xi_i}^{\xi_f} E_z(\xi)d\xi$.

Assuming that the accelerating field continues with the linear slope along the longitudinal direction from ξ_i to the end of the cavity ξ_f , we obtain a simple estimate of the magnitude $E_z(\xi_f)$ and the maximum difference in pseudo-potential:

$$E_z(\xi_f) \sim -\frac{r_m}{2}, \quad (4.6)$$

$$\Delta\psi_{max} \sim \left(\frac{r_m}{2}\right)^2, \quad (4.7)$$

where we assumed the ion cavity to perfectly match a spherical shape. The maximum blowout radius r_m depends on the beam normalized charge per unit length Λ_b , as we will derive in Appendix B. Given this dependency, we can relate the maximum pseudo-potential difference $\Delta\psi$ to the driving beam current:

$$\Delta\psi \sim \Lambda_b = \frac{2I_b}{I_A} \quad (4.8)$$

where $I_A = 4\pi\varepsilon_0 mc^3/e \simeq 17.05$ kA. The trapping condition Eq. 4.5 relates to the driving beam current as $I_b \sim I_A/2$, showing how kA current beams are required in order to induce a sufficiently deep potential well able to trap the freed electrons.

The scaling laws presented in fact overestimate driving beam current required, since we assumed a linear slope of the accelerating field until $\xi = \xi_f$, i.e. the back of the bubble, where the PIC simulations show how the electric field behaviour is far from being linear with xi . The density spike corresponding to $\xi = \xi_f + \Delta$, where Δ is the

width of the electron sheet around the ion cavity, leads to a strong steepening of the electric field. The potential well is therefore much deeper than the one corresponding to Eq. 4.7, and the condition in Eq. 4.8 can be relaxed. Nowadays simple analytical models able to reproduce such nonlinear behaviour do not exist: we accepted to use Eq. 4.8, being conscious it represents an upper limit to the driving beam current to provide electron trapping.

Another important approximation we have employed is to relate the difference in pseudo-potential only to the longitudinal coordinate ξ , and we will qualitatively explain in the next section how the trapped electron behaviour changes as we introduce the transverse motion.

4.1.3 Dynamics of wake-field ionized electrons

In this section we present a detailed qualitative study of the dynamics of the ionization-injected electrons. We already showed how the trapping of electrons in the plasma wave is related to the depth of the potential well $\Delta\psi$ and to the ionization position ξ_{ion} inside the bubble. The first term depends on the driving beam current, and the second term is related to the electric field magnitude, which also depends on the driving beam current and on the plasma background density ($E \sim \sqrt{n_0}$), and to the ionization potential of the atom. In Fig. 4.4 we showed the ionization probability as a function of the electric field for the Ar atom, and it is possible to appreciate how the ionization process starts for electric field intensities higher than a few tens of GV/m.

By combining the ionization threshold and the trapping threshold, we aim to define an ionization volume inside the bubble which satisfies the trapping condition $\forall(r, \xi)$, which we will call *injection volume*. In Fig. 4.6 we show the injection volume for three different dopant element: Argon, Nitrogen and Neon, the colours corresponding

to the ionization probability. We assume that Ar and N are already pre-ionized up to the first level, while Ne is ground state. The reason of the choice of the initial ionization state is related to the pre-ionization of the background hydrogen, required for the development of the plasma wave, as we will explain later in details.

The injection volumes presented in Fig. 4.6 were obtained in the same blowout

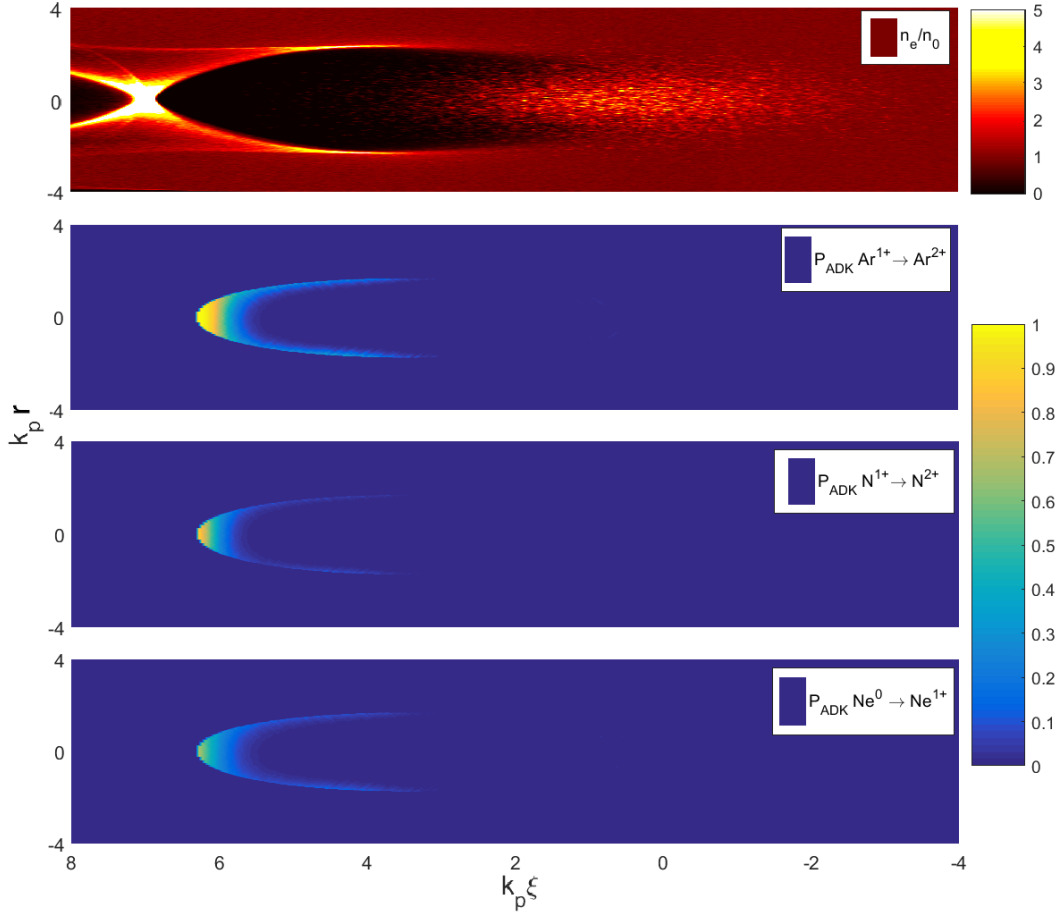


Figure 4.6. Plasma density contour plot a) and injection volumes for N^{1+} b), Ar^{1+} c) and Ne^0 d)

configuration, where the electric field intensity corresponds to what we have shown in Fig.4.3, obtained via PIC simulations. The results for Ar^{1+} and N^{1+} are very similar, both in terms of local ionization probability and injection volume, while the local ionization probability for Ne^0 is much lower and does not reach unity in

the trappable region. This difference compared to Ar^{1+} and N^{1+} leads to a lower trapped charge along the injection process.

The ionization probability distribution $P(r, \xi)$ we have shown in Fig. 4.6, determines the initial condition of the ionization-injected electrons dynamics, and therefore defines the self-injected beam properties. A quantitative analysis of this aspect will be presented in the next chapter.

The dynamics of a ionization-injected electron can be divided in two different time-scales: a fast transient one, which takes place between the ionization time t_{ion} and the trapping time t_{trap} , and the slow, long term steady state for $t > t_{trap}$, when the electron has already reached relativistic velocity and becomes stationary with respect to the plasma wave.

The long term steady state motion can be studied via a anharmonic relativistic oscillation model in time. The transverse forces of the ion cavity are responsible of the oscillation, which slowly damps due to the constant accelerating field $E_z(t_{trap})$ corresponding to the phase ξ_f in the wake where the electron reached $v_z \sim v_{phi}$.

The transient dynamics instead obeys to Eq.2.57, which we have presented in Section 2.2.3, and can be numerically solved for a given pseudo-potential $\psi(r, \xi)$. However, the analytical model does not well reproduce the electric field behaviour at the very end of the bubble, since it gives a quasi-linear dependence of the accelerating field with respect to the co-moving variable ξ , and leads to an underestimation of the potential well depth and therefore of both the trapping parameters such as trapping time, position, and energy.

As a qualitative analysis, we want to present the results of the study of the dynamics of the trapped electrons via a 2D Particle Tracking Code we have developed. In this code, the electrons are treated as test particles which move in the frozen fields in

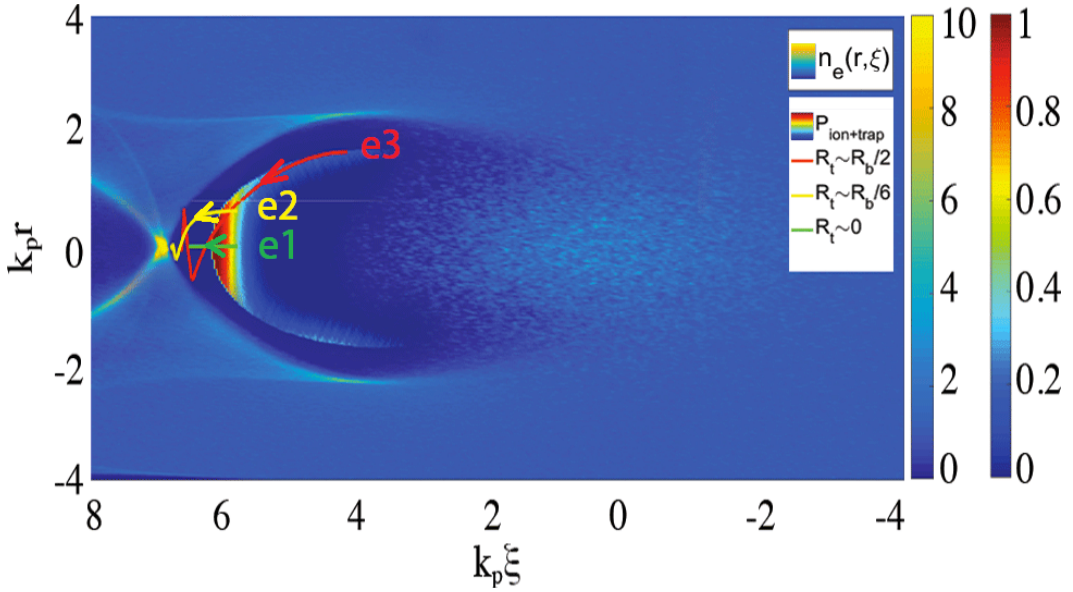


Figure 4.7. Trajectories of the electrons for Ar^{1+} injection volume

the laboratory frame obtained by the PIC Code ALaDyn. In Fig.4.7 the trajectories of the ionization-injected electrons are shown for the example case of Ar^{1+} injection volume.

The highest ionization probability, i.e. higher than 0.5, is confined in a hemispherical area of radius $R_t \sim R_b/3$ and length $\Delta z \sim R_b/6$, where $k_p R_b \sim 3$ is the bubble radius in dimensionless quantities. The light blue shadow, similar to a hollow cylinder having $R_t \sim R_b/2$ and length $\Delta z \sim R_b$, corresponds to a lower ionization probability area, and is responsible of the tails of the distribution function representing the self-injected beam.

In Fig. 4.8 is shown the longitudinal position as a function of time of three representative test electrons having initial coordinates $e_1 \equiv (k_p R_{t1} \sim R_b/2, k_p \xi_{t1} = 4)$, $e_2 \equiv (k_p R_{t2} \sim R_b/6, k_p \xi_{t1} = 5.7)$ and $e_3 \equiv (k_p R_{t3} \sim 0, k_p \xi_{t3} = 5.7)$. The final position of the j^{th} ionization-injected electron e_j corresponds to the $\xi_{f,j}$ which satisfies the trapping condition Eq. 4.5. For the electron on axis e_3 we can see both

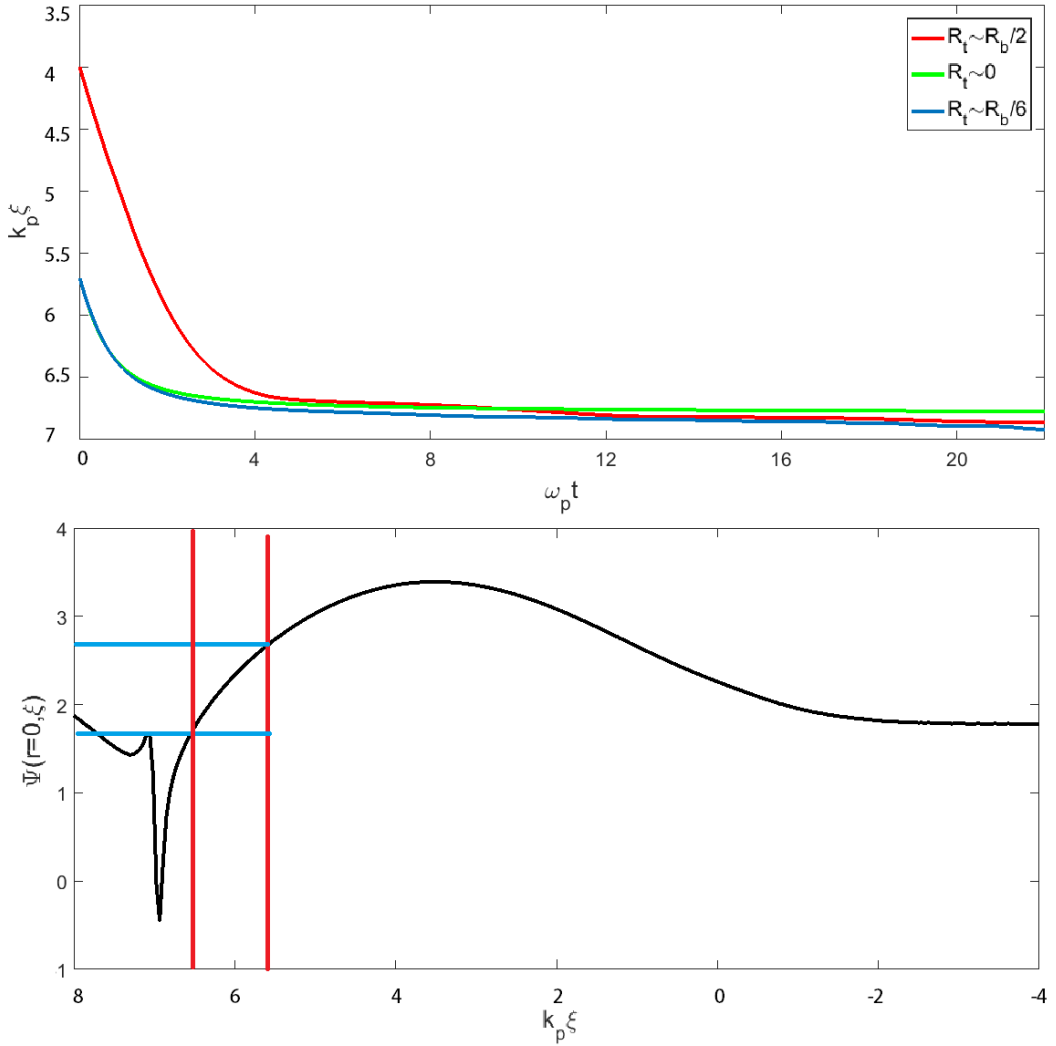


Figure 4.8. Longitudinal position evolution during the transient time. Electrons with an initial offset with respect to the propagation axis (red and blue curve) become relativistic at larger ξ .

via the pseudo-potential on axis $\psi(r = 0, \xi)$, knowing the initial position, and via the particle tracking, that it corresponds to $k_p\xi_{f,3} \sim 6.75$.

For the off-axis electrons e_1 and e_2 it is not obvious to foresee the final trapping position, since the transverse motion influences the trapping process. As a matter of fact, we can see in Figs. 4.10 and 4.9 the different behaviour of the particles in terms of transverse motion and how it affects the longitudinal dynamics.

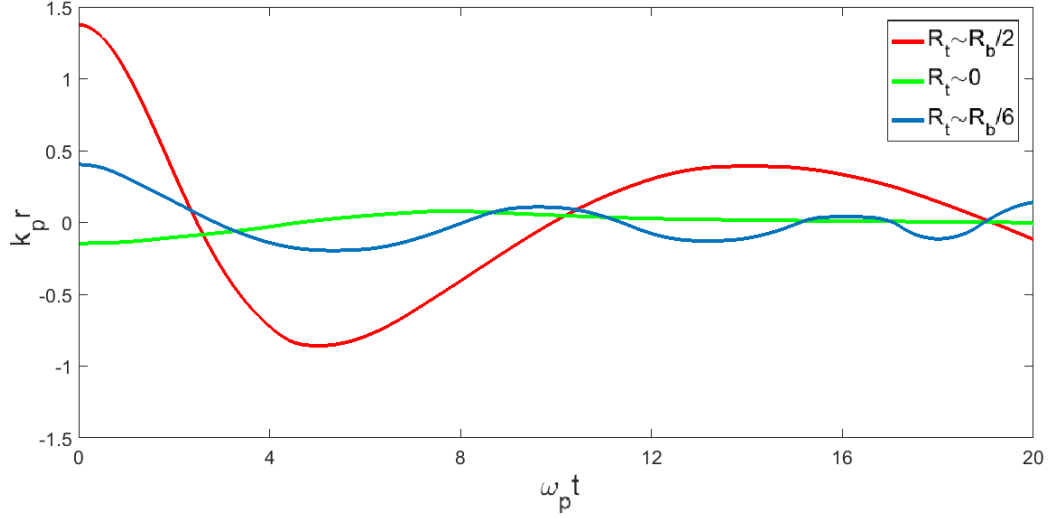


Figure 4.9. Electron transverse oscillation as a function of time, for different initial radial positions.

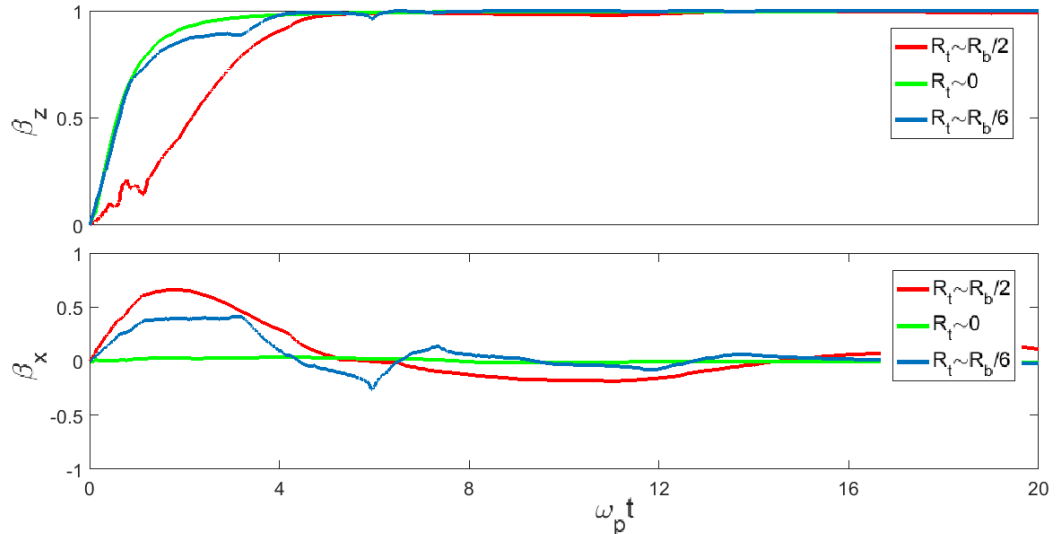


Figure 4.10. Electron longitudinal velocity a) and transverse velocity b) as a function of time, for different initial radial position.

The on-axis electron e_3 reaches the phase velocity of the plasma wave at $\omega_p t_3 \sim 4$ and at the same time it stops its motion relatively to the plasma wave, at $\xi_{f,3}$. On the

other hand the transverse electrons at the same $\omega_p t \sim 4$ still have residual transverse velocity due to the focusing forces of the plasma wake. It is possible to estimate these forces since the dimensionless radial field goes as $W_t = E_r - \beta_z B_\phi \sim r(1 - \beta_z)$: at the beginning of the motion, when $\beta_z = 0$, the off-axis electrons feel respectively a radial field $E_r(r_1) \sim R_b/2$ and $E_r(r_2) \sim R_b/6$. On one hand, electron e_2 initially feels a lower focusing field than e_1 , but on the other hand a higher accelerating field, since $E_z(\xi_{i,2})/E_0 \sim 1 > E_z(\xi_{i,1})/E_0 \sim 0.05$. The transverse oscillation of e_2 damps due to the higher acceleration in roughly 1.5 oscillation period, until e_2 becomes fully relativistic ($\omega_p t_2 \sim 8$).

Electron e_1 on the other hand is freed at $\psi(\xi_{i,1}) < \psi(\xi_{i,2})$, and reaches the on-axis condition Eq. 4.5 before electron e_2 , stopping its de-phasing after $\Delta\xi_1 < \Delta\xi_2$.

However, the on-axis condition on the pseudo-potential is proved to be limiting in multidimensional dynamics, since it would have predicted for electrons e_1 and e_2 to have a difference in their final positions $\sim 0.7k_p$, while considering the transverse motion with the tracking code, this difference is approximately $\xi_1 - \xi_2 \sim 0.12k_p$. With the results of the tracking code it is also possible to estimate qualitatively a trapping condition for the ionized electrons, given the analysis on the multidimensional motion we have presented so far.

In Fig. 4.11 is presented the γ factor growth as a function of ξ for electrons e_1 , e_2 and e_3 . We can see the gamma factor corresponding to the oncoming steady state is the same for the electrons having initial transverse position closer to the axis, i.e. $\gamma_{f,2} = \gamma_{f,3} \sim 8$, while the residual transverse momentum of e_1 explains the higher value $\gamma_{f,1} \sim 12$, as we can see in Fig. 4.12.

Besides, electron e_1 and e_3 have steady state phases corresponding to a lower accelerating field than electron e_2 , and the energy growth they subdue is therefore

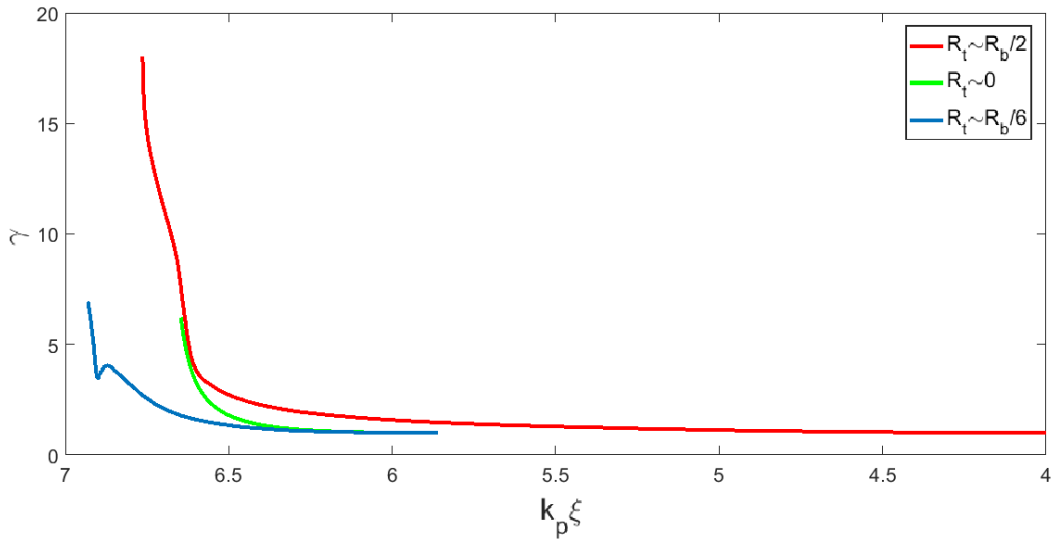


Figure 4.11. Electron Lorentz gamma factor as a function of ξ , for different initial radial positions.

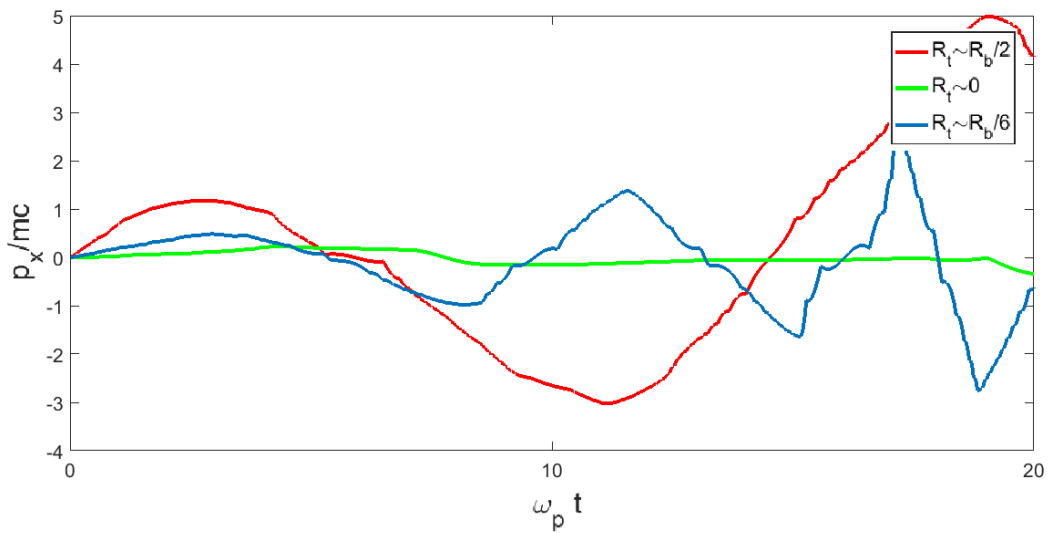


Figure 4.12. Electron transverse momentum evolution in time, for different initial radial positions.

less steep. This difference in acceleration due to different trapping steady-state phases determines what we call *beam – lenght energy spread*. We will discuss in details this topic in the next Chapter.

The electrons e_1 and e_2 represent the most significant cases in terms of characteristics,

since they are freed in the region of the bubble corresponding to an ionization probability close to 0.9, while electron e_3 is injected with a lower probability, close to 0.3. Its weight for determining the self-injected beam properties corresponds to the tail of the beam distribution both in energy, energy spread and emittance.

In the next chapter we will present the results of the PIC simulations we have performed, and we will extend the single particle dynamics to the dynamics of a realistic beam.

4.2 Chapter 4 Summary

In this chapter was developed the concept of injection volume, as the region inside the blowout cavity where both ionization and trapping of freed electrons occurs. It was discussed how the geometry of the injection volume is related to the magnitude of the electric field inside the blowout cavity, for what it concerns the ionization position ξ_i , and to the more general trapping condition Eq. 4.5, which determines either if the freed electron is trapped at ξ_f or it is not. It was shown how the dynamics of the ionization-injected electrons can be split in two timescales: a fast transient, characterizing the trapping process, and a long steady state, characterizing the transport of the trapped electrons once they have become relativistic and co-propagate with the plasma wave. Given the difficulties of dealing with a predictive yet simple analytical model of the blowout regime, a Particle Tracking Code I have developed was employed to study the transient dynamics, which I believe is the one determining the self-injected beam parameters, such as beam charge, duration, spot size, emittance, and energy spread. The injected electrons were treated as test particles moving according to the non-evolving electromagnetic fields obtained via PIC simulations. In this space-charge-free domain I tracked a representative group of electrons, freed in three different positions inside the injection volume,

so that the envelope of their trajectories would closely reproduce the self-injected beam dynamics. Although the presented analysis is far from being conclusive, given the assumptions of test particles moving in a non-evolving wakefield, it gives a satisfactory insight on how the injection volume geometry influences the injected electrons. A retrospective tracking of the electrons in the full PIC simulation would surely represent a more proper study, especially regarding the transient timescale, where the non-relativistic electrons interact each other via the space-charge forces self-consistently developed.

Chapter 5

Beam properties analysis

5.1 Self-injected Beam characteristics

The goal of this thesis is to develop and characterize a plasma injector able to accelerate to GeV energies high brightness electron beams in a cm scale accelerating length. High brightness beams require high charge, tens of pC, for a very short duration, order of fs. These characteristics lead to very high current electron beams, about a few kA, able to drive a new generation of light sources like Free Electron Lasers. Besides, there are strong limitations on the normalized beam emittance and the beam energy spread, in order to contain the dimension of the undulators and to reach high radiation fluence.

As we presented in Section 4.1.3, electron dynamics in the bubble is related to the injection volume, which is related to the choice of the dopant gas that triggers the ionization process. The studies on the single electron trajectories give qualitative information to understand the beam properties, such as the beam spot size and duration, and can be applied as well to qualitatively understand the generation of the emittance and the energy spread. Besides, the ionization volume and the dopant choice are directly related to the injected charge, which leads itself to space charge

and beam loading effects that influence the beam quality.

To control the injected charge and to avoid beam quality degradation, the injection region is limited to a thin layer of a mixture of a background pre-ionized hydrogen and a certain percentage of dopant gas at the entrance of a capillary (Fig.5.1), filled with pre-ionized hydrogen that serves as accelerating and transport device.

The length of the dopant layer is related to the so called *slice energy spread* and to the injected charge, as we will discuss later in details via both qualitative analysis and PIC simulation results.

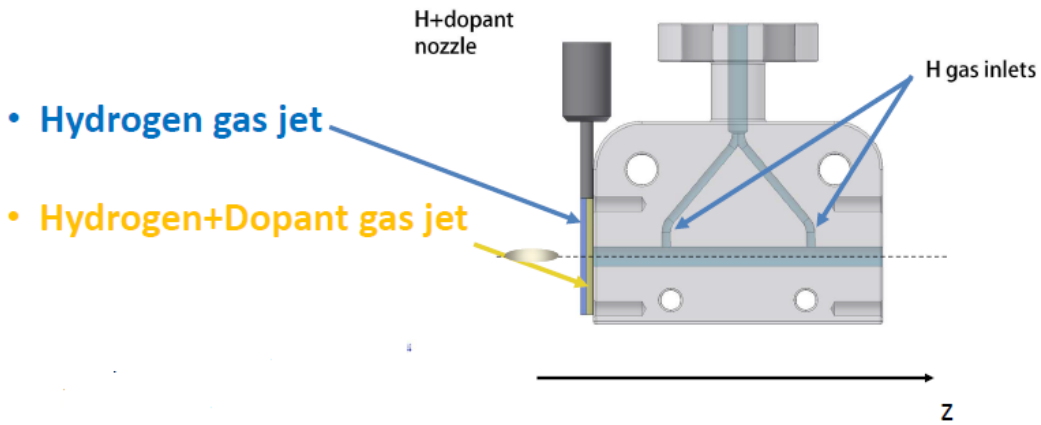


Figure 5.1. Layout of plasma injector for Wake-Field Ionization Injection. The driver beam propagates from left to right and encounters a two region gas jet (Hydrogen)+(Hydrogen+Dopant) as injection region, and a capillary for transport and acceleration.

5.1.1 Beam spot size and emittance

Electrons injected via Wake-Field Ionization Injection have initial position r_i in the injection volume, thus related to the electric field intensity and to the nature of the dopant gas. We assume for the initial momentum $\mathbf{p}_i = 0$ since as far as we can treat

the plasma as a cold plasma, the thermal velocity related to the background energy (a few eV) is much smaller than the phase velocity of the plasma wave.

As the drive bunch propagates through the plasma and the trapped electrons rotate in the $x - p_x$, or $y - p_y$ plane (Fig.5.2), the wake collects additional electrons at $\theta = 0$, resulting in a uniform distribution in θ and a finite emittance. The forces exerted by the ion column are linear, and therefore no emittance growth is induced after the ionization process is completed.

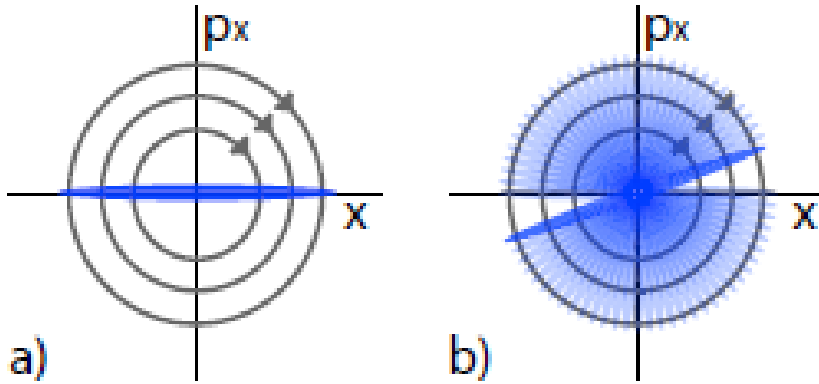


Figure 5.2. The initial distribution of trapped electrons in the $x - p_x$ plane immediately following ionization a) and its rotation along the ionization path b).

We can approximately relate the emittance of the self injected beam to the ionization volume, since:

$$\varepsilon_{n,rms} = \frac{1}{mc} \sqrt{\langle x^2 \rangle \langle p_x^2 \rangle - \langle xp_x \rangle^2}, \quad (5.1)$$

$$\langle x^2 \rangle = \sigma_x^2, \quad (5.2)$$

$$\langle p_x^2 \rangle = \sigma_{p_x}^2. \quad (5.3)$$

Following the derivation in [75], we can now give an estimate to the normalized emittance for the trapped beam, i.e. co-propagating with the wake at $\xi = cost$, assuming that the relative change in γ for the beam is small during one oscillation. With this assumption the equations for the coupled transverse and longitudinal motion in dimensionless variables are:

$$\frac{dp_x}{dt} = \frac{m\omega_p^2 x}{4} (1 + \beta_z), \quad (5.4)$$

$$\frac{dp_z}{dt} = \eta m c \omega_p, \quad (5.5)$$

where η is a multiplying factor used to consider the real magnitude of the accelerating field, ranging from 1, the 1D Wave-breaking limit, to a maximum related to the background density and the driving beam current.

With the assumption of small change in γ during one oscillation, the transverse component of Eqs. 5.4 has the following solution:

$$x(t) = x_i \cos \left(\frac{\omega_p t}{\sqrt{2\gamma_f}} + \theta_i \right), \quad (5.6)$$

$$p_x(t) = -m\omega_p x_i \sqrt{\frac{\gamma_f}{2}} \sin \left(\frac{\omega_p t}{\sqrt{2\gamma_f}} + \theta_i \right), \quad (5.7)$$

where we set x_T as initial value of $x(t)$ and x_i as initial value of $p_x(t)$ because the injected beam shrinks its spot size during the first oscillation, but the transverse momentum spread depends on the initial transverse position of ionization inside the bubble. Keeping this result in mind, we obtain the expectation values required for the determination of the emittance:

$$\langle x^2 \rangle = \frac{x_i^2}{2}, \quad (5.8)$$

$$\langle p_x^2 \rangle = \frac{m^2 \omega_p^2 \gamma_f}{2} \frac{x_i^2}{2}, \quad (5.9)$$

$$\langle xp_x \rangle = 0. \quad (5.10)$$

A substitution of these expectation values into the emittance definition yields:

$$\varepsilon_{n,rms} = k_p \frac{x_i^2}{2} \sqrt{\frac{\gamma_f}{2}}. \quad (5.11)$$

The σ_x^2 we have to take into account to compute the beam spot size at the steady state condition, when the electrons co-propagate with the bubble at $v_z = v_\phi$, is related to the longitudinal dynamics of the ionized electrons and is related to the amplitude of the beam betatron oscillations.

As we have seen in the previous chapter, the amplitude of the electron oscillation during acceleration in the plasma wake, which is related to the σ_x of the self-injected beam, damps because of the energy growth. We can approximately relate the trapping oscillation amplitude x_T to the γ_f and the initial amplitude oscillation x_i [76][77][78], which corresponds to the radius of the ionization volume $R_b/2$:

$$x_T \sim \frac{x_i}{2} \left(\frac{1}{\gamma_f} \right)^{1/4}. \quad (5.12)$$

With the values of $\gamma_f = 8$, $k_p x_i = 0.3$ that we have obtained in the previous chapter for the test electrons, we get $k_p x_T \sim 0.1$. It is important to notice how this value does not take into account space charge effects nor beam loading effects, which are

in fact highly relevant in our simulations, since the injected charge is large enough to perturb the plasma wake-field.

The values we have presented are just lower boundaries of the beam emittance and the spot size achievable for the wake-field ionization injection scheme, assuming no space charge effects nor beam loading of the plasma wake. In real scenarios, the injected charge self-field leads to a larger spot size for the beam and therefore to a larger emittance.

Besides, dopant electrons are ionized at different times as the wake propagates through the dopant layer. Since electrons ionized at different times have different initial betatron phase, the area in phase space increases during the injection process leading to emittance growth due to the phase mixing.

5.1.2 Beam length and energy spread

Electrons i, j freed at the same initial longitudinal position but at different radial positions inside the ion cavity will reach the phase velocity of the wave, and therefore will be trapped, at different longitudinal final positions. Typically if $x_{i,0} < x_{j,0}$ we will have $\xi_{i,T} < \xi_{j,T}$, and this difference in longitudinal trapping positions determines approximately the self-injected beam length.

We can assume that the head of the beam ξ_H corresponds to the electrons which have been ionized at $x_i = 0$, and whose dynamics is therefore purely longitudinal. Conversely, the electrons ionized at $x_i \neq 0$ gain additional transverse velocity and momentum, and therefore get trapped at $\xi_T > \xi_H$.

This difference in final locations for the trapped electrons is partially responsible to the energy spread of the beam. If we assume that no beam loading effects occur, i.e. the beam charge does not perturb the accelerating field, along the transport the

head of the beam will feel a constant value of accelerating field lower than the tail of the beam, i.e. $|E_z(\xi_H)| < |E_z(\xi_T)|$. If we assume that at FWHM of the beam profile $\Delta\xi = L_{beam} \sim 0.3k_p^{-1}$, as we have found with the particle tracking code, at the end of the transport L_{acc} the corresponding induced energy spread at trapping will be:

$$\frac{\sigma_\gamma}{\bar{\gamma}} = \frac{\left(\frac{\partial E_z}{\partial \xi} L_{beam} \right) \frac{L_{acc}}{6mc^2}}{\gamma_f + \left(E(\xi_H) + \frac{\partial E_z}{\partial \xi} L_{beam} \right) \frac{L_{acc}}{mc^2}}, \quad (5.13)$$

where we have assumed a linear slope of the electric field along the beam length and a Gaussian current distribution. For $L_{acc} = 600 \mu\text{m}$, an accelerating field slope $\frac{\partial E_z}{\partial \xi} \sim 20 \text{ ((GV/m)/}\mu\text{m)}$ and for an injection energy $\gamma_f = 8$ (as given by the tracking code), we obtain $\sigma_\gamma/\bar{\gamma} = 0.087$.

We called this term *beam length energy spread*. Its effect is an unavoidable drawback of the high transformer ratios we obtain in the blowout regime and corresponds to a lower limit of the energy spread for a low charge beam, either externally and internally injected. The longitudinal phase space presents a typical chirped profile, with the tail of the beam at much higher energies than the head, due to the large difference in accelerating field felt along the transport. The electric field gradient at the back of the bubble (Fig.5.3) ensures extreme acceleration in very short distances, but on the other hand determines high energy spread even for extremely short beams such as the wake-field ionization injection ones, which reach $\sim \text{fs}$ level duration and less.

The finite active ionization length induces energy spread as well, particularly the so-called *slice energy spread*, which corresponds to the thickness of the longitudinal phase space distribution along the longitudinal momentum direction. Electrons that have been ionized at different times t_{ion} , and therefore different longitudinal

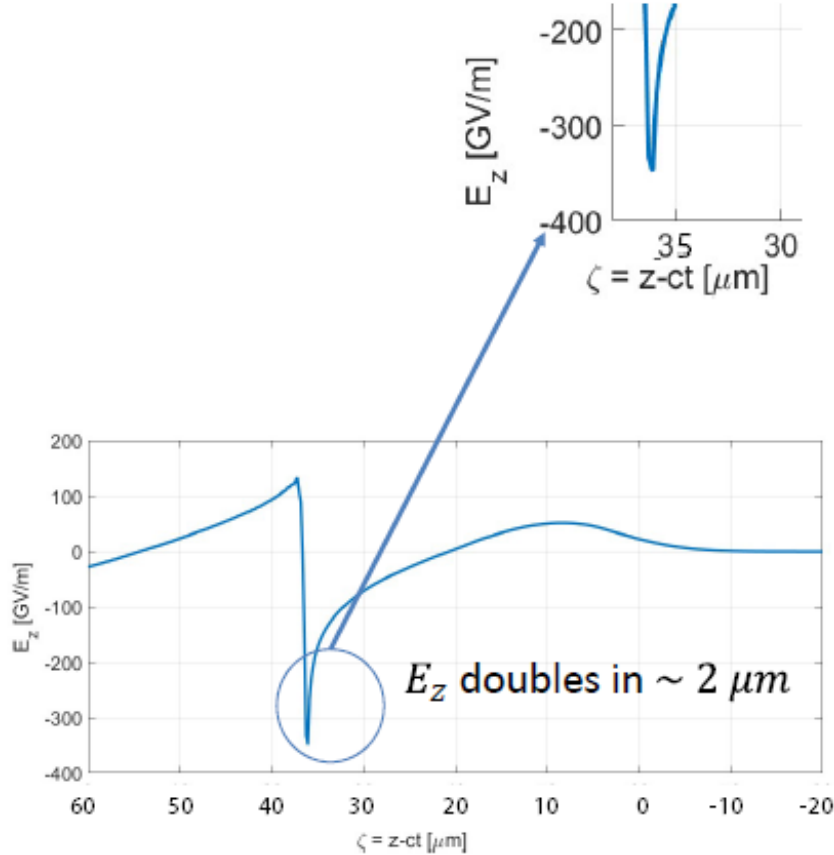


Figure 5.3. The steep slope of the accelerating field at the back of the bubble determines high transformer ratios, but also high energy spread even for extremely short beams.

positions along the transport, will eventually be trapped at the same ξ_f inside the bubble, but with different energies corresponding to the different t_{ion} .

Electron on axis which have been ionized at the beginning of the ionization region will have reached at the end of it an energy $\gamma_1 = \gamma_T + \frac{E_z(\xi_T)L_{dopant}}{mc^2}$, while electrons ionized at same ξ_T but at the end of the ionization region will have gained $\gamma_2 = \gamma_T$, corresponding to the minimum energy necessary to be trapped.

The dopant layer induced energy spread will therefore modify the beam energy spread since electrons at the same ξ will have different energies, and with the same assumptions as for Eq. 5.13, we will have the expression:

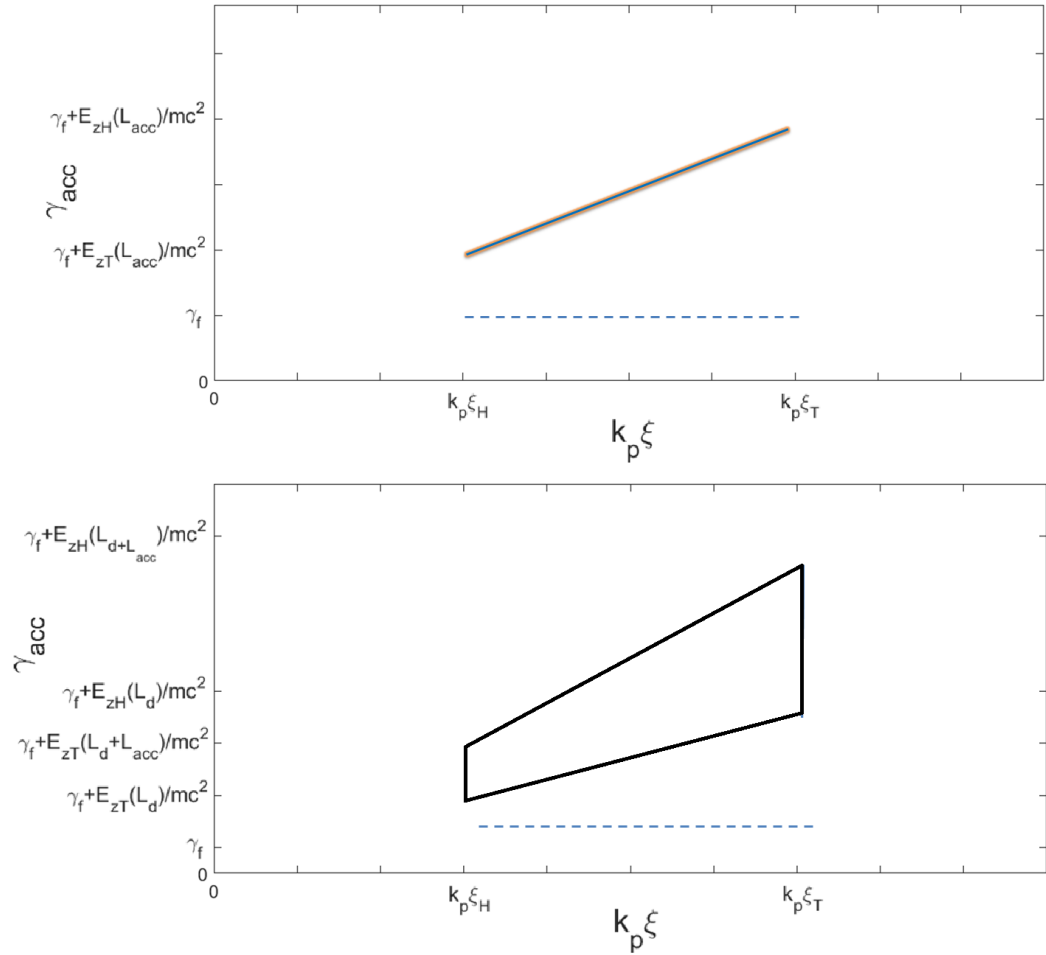


Figure 5.4. Comparison between theoretical longitudinal energy profiles for a) beam length energy spread induced b) beam length + dopant length energy spread induced. The ionization length introduces a spread in energy related to the ionization time along the transport, related to the thickness of the $\gamma(\xi)$ profile.

$$\frac{\sigma_\gamma}{\bar{\gamma}} = \frac{1}{6mc^2} \frac{\left(L_d E(\xi_H) + (L_d + L_{\text{acc}}) \frac{\partial E_z}{\partial \xi} L_{\text{beam}} \right)}{\gamma_T + \left(2E(\xi_H) + \frac{\partial E_z}{\partial \xi} L_{\text{beam}} \right) \frac{2L_{\text{acc}} + L_d}{4mc^2}}, \quad (5.14)$$

where L_d is the active ionization region, and L_{acc} is to be considered to start after L_d . Equations 5.13 and 5.14 are derived from a simplified geometrical analysis of the longitudinal phase space of the self-injected beam shown in Fig. 5.4. They assume a

uniform electron distribution along the $z-p_z$ coordinates and are far from being a conclusive scaling law, but clearly show the dependence of the energy spread both by the beam length and the dopant layer length. We will compare the results from this scaling formula to the PIC simulation results in the next sections.

This contribute for the energy spread can be reduced by reducing the active ionization length, contemporary raising the dopant percentage to keep constant the injected charge. The upper limit of dopant percentage is $\sim 10\%$ of the background density for a flat, sharp-edged distribution along the longitudinal coordinate, since the electron density raise becomes significant with respect to the background. Such a density gradient at the interfaces between the hydrogen + dopant region and the pure hydrogen region, would cause undesired dark current. As a matter of fact, the fall of the n_e along L_{dopant} changes the phase velocity of the plasma wave and determines self-injection phenomena similar to the so called down-ramp injection scheme [55] or shock injection scheme [80].

In this qualitative analysis of the energy spread for the wake-field ionization injected beams we did not consider beam loading effects, to clarify the different energy spread generation causes. Beam loading effects for high charge injected beams, > 10 pC, can flatten the accelerating field along the longitudinal direction, leading to smaller values of energy spread for at least the beam FWHM.

5.1.3 Beam Charge

The self-injected beam charge, for a given dopant gas percentage, is related to both the ionization region and the dopant layer length. We have shown in the previous chapter how the ionization region inside the bubble can be approximately defined as a hemispherical surface A_{ion} having radius $r_{ion} \sim R_b/2$ and width $\Delta z \sim R_b$,

resulting in $A_{ion} = \Delta z \pi (R_b/2)^2 = \pi R_b^2$ with finite probability of both ionization and trapping.

The injected charge can be therefore obtained integrating the ionization surface and the dopant density along the longitudinal direction:

$$Q_{inj} = \int_0^{L_d} A_{ion} n_d dz \sim \pi R_b^2 n_d L_d \quad (5.15)$$

where n_d is the density of the dopant element.

The injection of electrons along the transport leads to the loading of the bubble electric field, and therefore to the gradual drop of the electric field intensity. The injection rate diminishes in time and theoretically stops where the beam charge is so high that the resulting electric field in its wake is lower than the ionization threshold given by the ADK model.

In our simulations we avoided this injection self-termination by selecting a dopant layer length, i.e. the active ionization length along the transport, limiting the charge injection and therefore the loading of the wake.

5.2 Numerical experiment layout

In order to characterize the Wake-Field Ionization Injection scheme we performed our simulations choosing three different dopant elements: Argon, Nitrogen, and Neon. The initial ionization level of the dopant elements was chosen to match the pre-ionization of the hydrogen, which is needed for the development of the plasma wave and can be achieved via a low intensity laser beam or via an inductive discharge. Therefore both the Argon and the Nitrogen were set as Ar^{1+} and N^{1+} , since the ionization potential of the first level is close to the ionization potential of

the hydrogen, and we can assume that if the pre-ionization discharge/laser is able to 100% ionize the hydrogen, it is able to ionize the dopant first level as well. This assumption does not apply to Neon, since the first ionization potential is $\sim 4/3$ the hydrogen ionization potential and it is unlikely ionized by the pre-ionization discharge/laser.

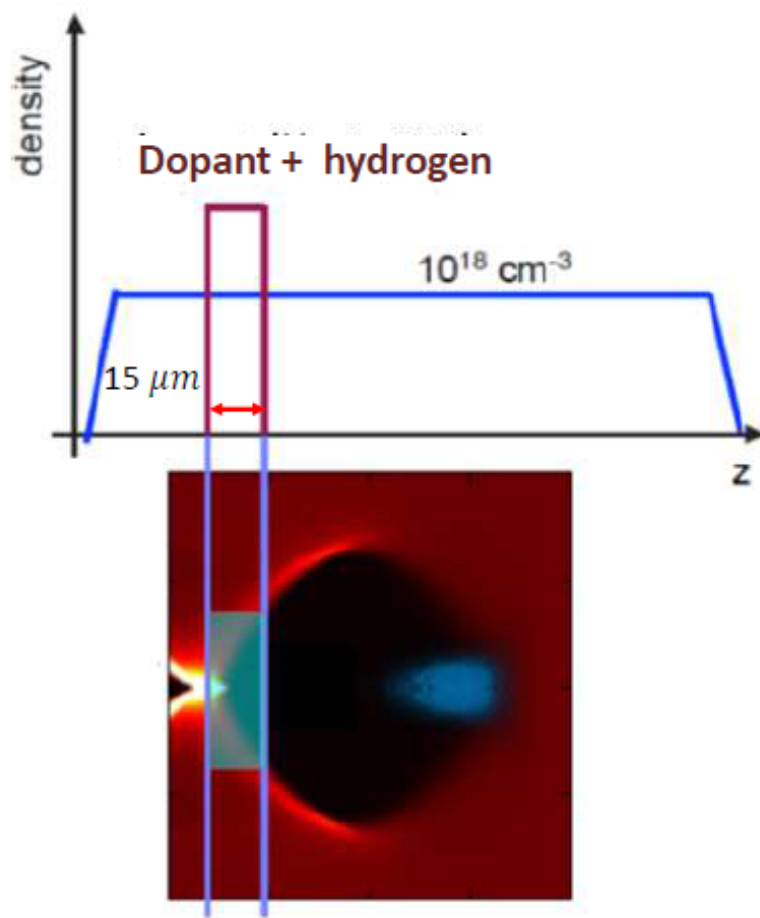


Figure 5.5. The background density distribution and the dopant density distribution along the propagation direction.

However, we performed a simulation also with pre-ionized Neon and compared its results to the ground state case: the different ionization potentials of the two states determines a different injection volume, and therefore different self-injected

beam properties.

We chose a background plasma density $n_0 = 1.2 \times 10^{18} \text{ cm}^{-3}$ in such a way to induce an accelerating field able to produce GeV electron beams in a cm-s length scale, i.e. $E_z \sim 100 \text{ GV/m}$ as given by the 1D cold Wave-breaking limit. The dopant percentage, with respect of the background density, was chosen to inject an electron beam having a charge higher than at least 10 pC in an ionization active length (the dopant layer) of $15 \mu\text{m}$, as shown in Fig.5.5. The dopant layer length was chosen to reduce as much as possible the slice energy spread, avoiding injection of dark current.

We employed a 1 GeV, 10 kA peak current driver beam, with $\sigma_r = 4 \mu\text{m}$ and $\sigma_z = 7 \mu\text{m}$, to create a potential well deep enough to trap a kA current level self-injected beam. The transport distance of $600 \mu\text{m}$ was chosen to reach an asymptotic behaviour of the self-injected beam characteristics, such as emittance and energy spread, to define something we could call *injection distance*.

The simulative box was set with 416 cells along the longitudinal coordinate z , and 520×520 cells along the transverse plane xy , the elementary cells dimensions being $\Delta_z = 0.2 \mu\text{m}$ and $\Delta_x = \Delta_y = 0.08 \mu\text{m}$. Each cell contains 8 computational electrons in the whole domain, and 8 computational electrons+1 computational ion in the ionization active length L_d .

The high resolution we used, and the number of particles involved determined a very high computational cost in terms of simulation time (~ 10 days per simulation). We therefore used the PIC code ALaDyn with a 2D MPI decomposition along the transverse xy plane, and ran the simulations over 20x20 cpu-s at the INFN-CNAF computational centre.

5.3 Simulation results

In this section we present the results we have obtained via PIC simulations keeping the parameters we have defined in the previous section but varying the dopant element acting as active electron source. We want to compare the results of the simulations with the semi-quantitative estimates achieved thanks to the particle tracking code, and discuss the similarities and the differences.

Table 5.1. Simulation results after $\sim 600 \mu\text{m}$ propagation

Species	Q [pC]	I_{rms} [kA]	$\sigma_r[\mu\text{m}]$	$\sigma_z[\mu\text{m}]$
N^{1+}	22.2	4.7	0.69	0.57
Ar^{1+}	26.7	4.49	0.92	0.71
Ne^0	22.5	4.04	0.74	0.67

Table 5.2. Simulation results after $\sim 600 \mu\text{m}$ propagation

Species	$\frac{\sigma_\gamma}{\gamma}[\%]$	$\varepsilon_{n,rms}[\mu\text{m}]$	$\sigma_\gamma[\text{MeV}/mc^2]$	$\gamma[\text{MeV}/mc^2]$
N^{1+}	4.7	0.96	3.01	64.3
Ar^{1+}	5.9	0.96	3.58	60
Ne^0	7	1.15	4.5	64.2

In tabs. 5.1 and 5.2 we present the self-injected beam properties after the injection distance of $600 \mu\text{m}$. As we have previously demonstrated, the beam parameters for the three dopant elements are very similar one another, since the ionization volumes for each dopant element do not differ significantly.

We can assume for the ionization volume of each dopant element to be characterized

by $r_{ion} \sim 1.5k_p^{-1}$ and $\Delta_z \sim 3k_p^{-1}$, following the analysis of the previous chapter. Given this assumption, the injected charge along $15 \mu\text{m}$ of active ionization length should be, according to Eq. 5.15, $Q_{inj} \sim 50 \text{ pC}$, a factor 2 larger than the PIC simulation results since in our analysis we assumed that the whole ionization volume is characterized by a 100 % probability of ionization, which is strictly true for $r_{ion} \sim R_b/3$ and only for the Argon dopant element, while for both Nitrogen and Neon the corresponding ionization probability is lower.

The transverse dimension of the self-injected beam, recalling Eq. 5.12 and assuming that the initial oscillation amplitude corresponds to the weighted average of the oscillation amplitudes of the three test electrons whose dynamics we have studied, $r_1 = 0.4k_p^{-1}$ and $r_2 = 0.1k_p^{-1}$ with the probability $\sim 90\%$ to be injected and $r_3 = 1.3k_p^{-1}$ having the probability of 20%. The resulting $\sigma_M = 0.3$, and Eq. 5.12 with $\gamma_T = 8$, give a trapping spot size of $\sigma_T = 0.1k_p^{-1} = 0.55 \mu\text{m}$, which differs from the simulation values in a range of 50% – 100%.

The largest difference between our analysis and the PIC results corresponds to the Argon dopant element self-injected beam, which is the highest injected charge case. This dissimilarity agrees with the fact that non-linear space charge effects must be considered during the transient between ionization and trapping if the injected charge is high, resulting in a larger spot size.

The beam energy spread for an average beam length of $\sim 1.5 \mu\text{m}$, can be obtained from Eq. 5.14 as we have mentioned in the previous sections. Assuming again $\gamma_T = 8$ and $\partial E_z / \partial \xi \sim 50 \text{ (GV/m)}\mu\text{m}$, we obtain for $15 \mu\text{m}$ dopant layer $\sigma_\gamma / \gamma \sim 11\%$, a value two times larger than the PIC results. This difference between the result from Eq. 5.14 and the PIC results is mainly due to two reasons: the first one is that we did not consider the probability distribution of the injected electrons. This determines automatically that we assume a uniform electron distribution in the injection area,

and therefore overestimate the energy spread induce by the dopant layer length.

The second, more important, reason is that in the tracker analysis, beam loading effects were neglected. In fact, the space charge field of the self-injected beam flattens the acceleration profile along the longitudinal direction for a length \sim to the FWHM of the self-injected beam, close to L_b , as one can appreciate in Fig. 5.6, where the longitudinal phase spaces are presented together with the energy spectrum.

Almost the $\sim 75\%$ of the charge is confined in the FWHM of the self-injected beam duration, $\sim 1.5 \mu\text{m}$, where the phase space shows a flat profile along z and whose width corresponds to the slice energy spread determined mainly by the dopant layer length. The beam emittance at $600 \mu\text{m}$ transport is close to $1 \mu\text{m}$, which is twice the theoretical value obtained from Eq.5.11 $\varepsilon_{n,rms} = 0.42 \mu\text{m}$, where we used $\sigma_M = 1.4 \mu\text{m}$ and $\gamma_T = 8$. The space charge effects partially motivate this discrepancy, since the injected electrons feel each other in the transverse motion during the trapping transient, while they are still not relativistic. As a matter of fact, the equations we have used to derive this approximated emittance value do not take this aspect into account.

The reasons why the final emittance value differ so much from the theoretical value is still an open field of investigation. However we think that the main cause of emittance growth during transport is numerical Cherenkov instability. As reported in [81], numerical Cherenkov instability influences the transverse dynamics of the self-injected beam, as can be appreciated in Fig. 5.8, where we show the beam properties evolution along transport for $700 \mu\text{m}$ after the dopant layer, and Fig. 5.7, where snapshots of the beam 2D-zx beam profile are presented for $z = 300 \mu\text{m}$ and $z = 800 \mu\text{m}$ for Nitrogen.

The emittance decreases to a minimum value close to the theoretical one from

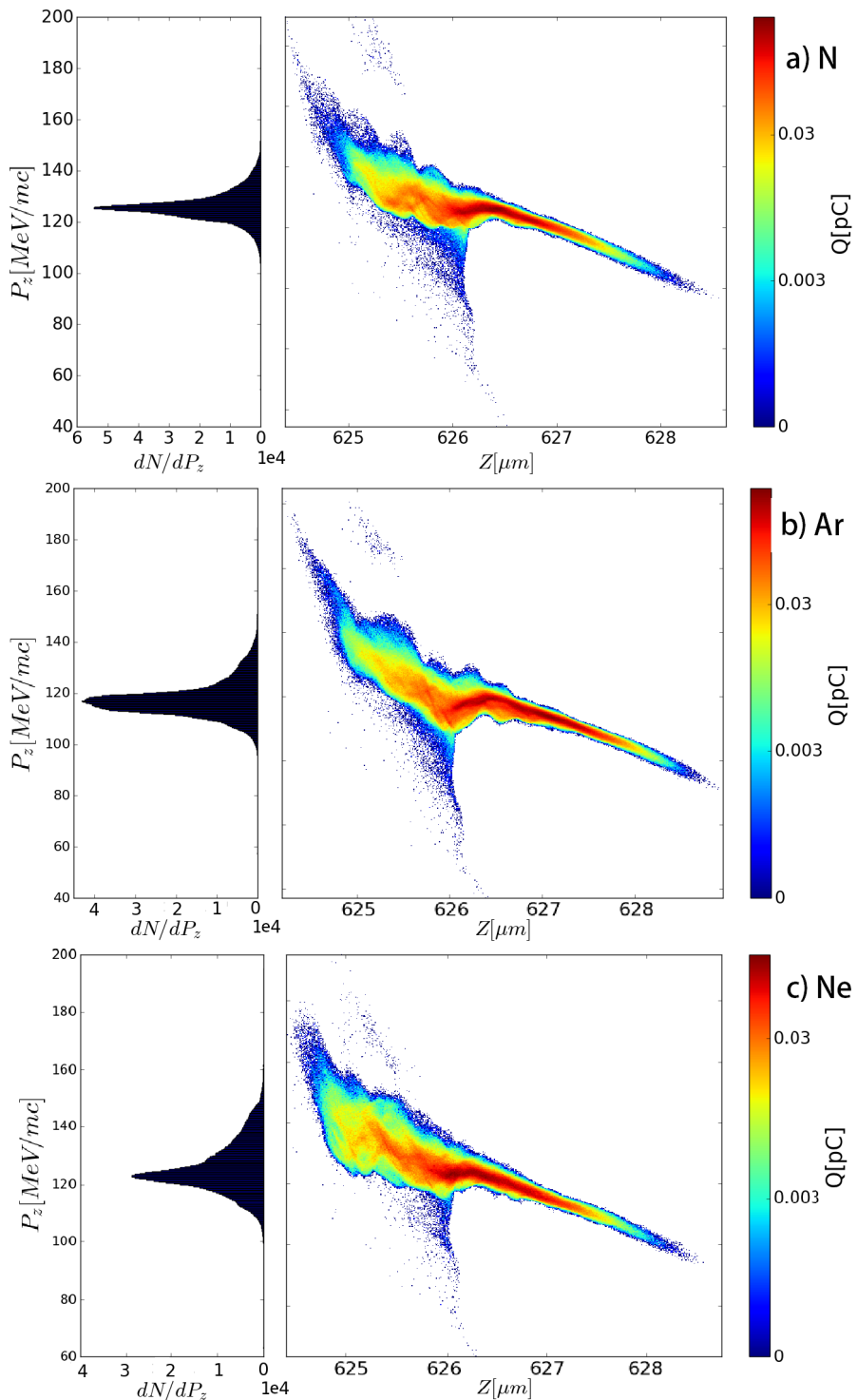


Figure 5.6. Longitudinal phase-spaces and energy spectra of a)Nitrogen, b)Argon and c)Neon, for the injection distance of 600 μm .

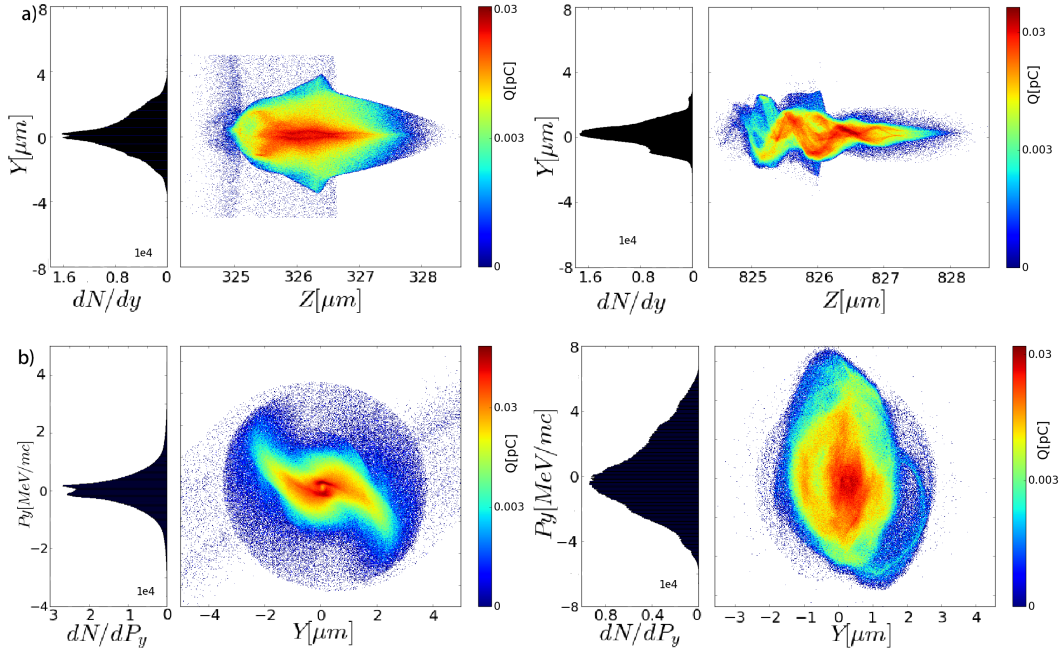


Figure 5.7. zy plane beam spot and transverse phase space for a) $300 \mu\text{m}$ propagation and $800 \mu\text{m}$ propagation. The numerical Cherenkov radiation effect on the beam envelope oscillation at the beam tail determines unphysical emittance growth along the transport.

Eq. 5.11 $\sim 0.6 \mu\text{m}$ and then slowly increases up to $1 \mu\text{m}$ due to the high spread in transverse momentum induced by the high frequency non-physical fields induced by numerical Cherenkov.

The energy spread decreases down to an asymptotic value which is theoretically function of the beam loading of the field, and thus related to the injected charge, of the ionization volume and the dopant length. However, the numerical Cherenkov influences this asymptotic value as well, because of the large noise it introduces in the electron transverse momentum, leading to a higher spread than how it is expected for a beam loaded configuration, where energy spread decreases while the mean energy of the beam linearly grows.

This behaviour is explained by the fact that the FWHM core of the beam feels a flat accelerating field along the transport, and therefore does not experience absolute

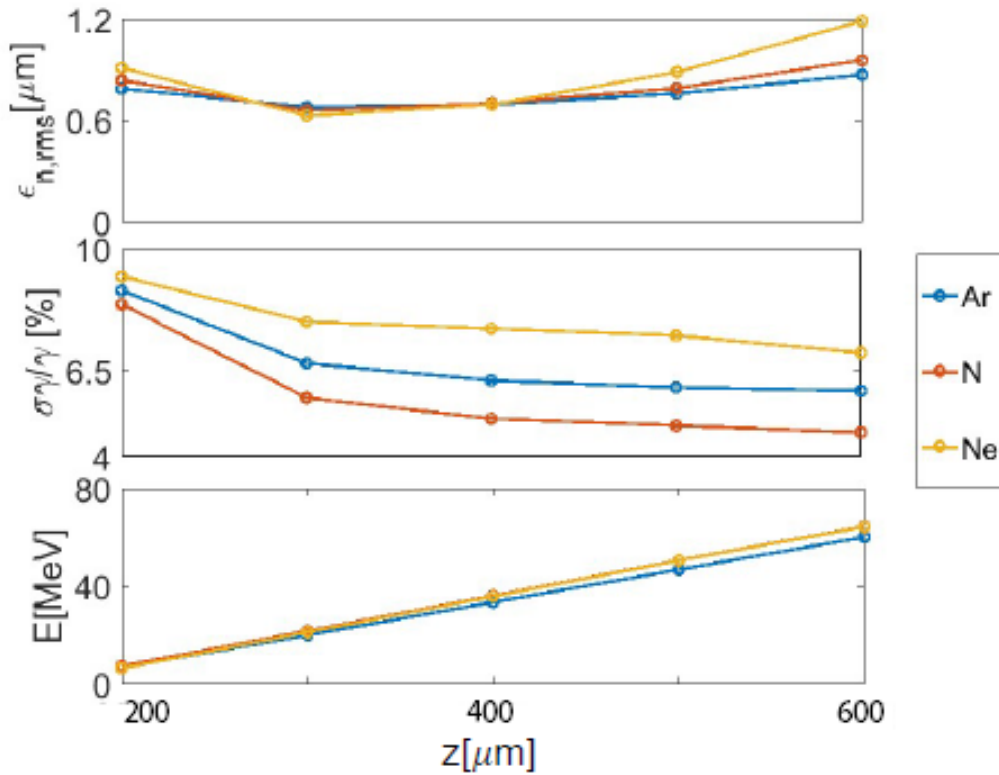


Figure 5.8. The beam properties evolution along transport in plasma for $600\mu m$ for Argon (blue curve), Nitrogen (red curve) and Neon (yellow curve).

energy spread growth while gaining energy, therefore reducing the relative energy spread. On the other hand, the tails at high and low energy feel a large difference in accelerating field, but their contribution to the behaviour of the whole beam is significantly lower, since they contain only $\sim 25\%$ of the beam charge.

The slice analysis in Fig.5.9 highlights how the betatron de-coherence corresponds to the high energy tail of the beam distribution, i.e. the highly non-linear area at the back of the bubble, where the numerical Cherenkov instability influence is higher. We finally compare in Fig. 5.10 the beam injection and transport for a pre-ionized Neon dopant and a ground state Neon dopant. It is clear from this comparison how

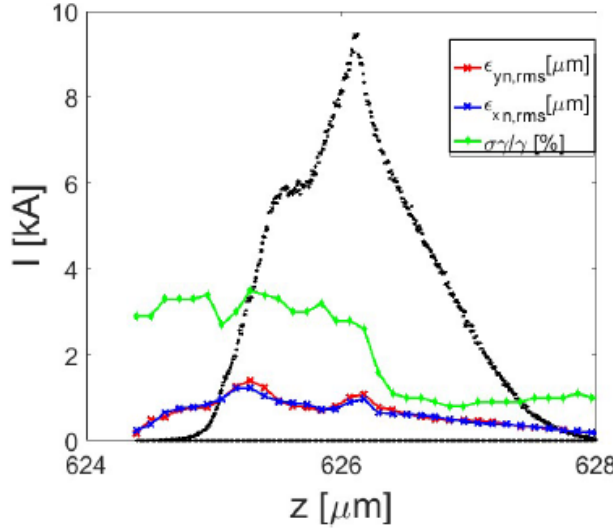


Figure 5.9. Slice analysis for N dopant element after 600 μm of acceleration. The beam current profile is superimposed on the relative energy spread (green curve) and the $\varepsilon_{xn,rms}$ and $\varepsilon_{yn,rms}$. The slice dimension was chosen equal to 0.1 μm .

the ionization volume determines different beam properties such as emittance and energy spread. As we have already shown, the emittance of the self-injected beam is related to the ionization volume transverse dimension. Since the ionization potential of ground state Ne is much lower than the Ne^{+1} , the ionization volume in the first case is much wider. This leads to more than double of emittance for ground state Ne compared to $Ne+1$ (0.45 μm vs 1.15 μm).

We compared the energy spread as well. In the pre-ionized case the injected charge is lower than the ground state case (0.1 pC vs \sim 20 pC) and the beam duration is smaller as well ($\sigma_{z,Ne^0} \sim 0.2 \mu\text{m}$ vs $\sigma_{z,Ne^{+1}} \sim 0.67 \mu\text{m}$). There is no beam loading effect and a moderate energy spread is induced because of the short length. The same value of $\sigma_\gamma/\hat{\gamma} \sim 7\%$ is surprisingly induced in the ground state case, but this time because even if the beam is longer, the higher charge of the beam strongly loads the field, flattening the profile along the beam. The beam loading effect is

even clearer if we compare the energy gain for the two cases (87 MeV vs 64 MeV).

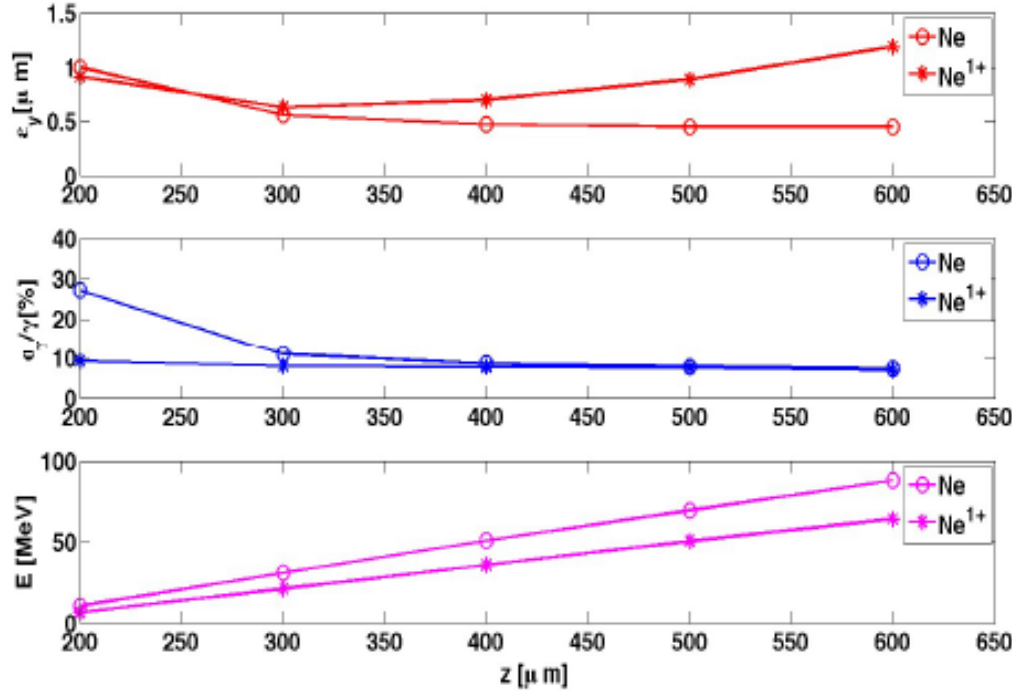


Figure 5.10. Initial ionization level influence on beam properties: Ne ground state and Ne^{1+} comparison over emittance (red curve), relative energy spread (blue curve) and energy gain (purple curve).

5.4 Chapter 5 Summary

In this Chapter were presented the results obtained via PIC simulations in different scenarios of the beam driven Wakefield Ionization Injection scheme. Several simulations were performed to first reproduce the data found in literature [69][70][71], and then to find the best-case scenarios in terms of self-injected beam quality and to characterize how the injection volume varies for different dopant elements and how it influences the beam properties. It was chosen to present the four most significant

PIC simulations in terms of beam quality, employing as dopant element respectively pre-ionized Nitrogen, pre-ionized Argon, ground state and pre-ionized Neon.

Low energy spread, low emittance and high current, and thus high brightness self-injected beams, are inherently generated in every dopant element configuration, since the core of the injection volume for the different dopant elements, i.e. the region of the blowout cavity where both ionization and trapping occur, do not differ significantly. The simulations, and the single particle dynamics, show how emittance and energy spectrum of the self-injected beam depend on the injection volume geometry, and therefore on the blowout configuration, the dopant element Z, and its initial ionization state.

The comparison of beam spot size, emittance, charge, and energy spread with the scaling laws presented in section 5.1 show a satisfactory agreement in the free-space-charge-force regime (i.e. pre-ionized Neon), while significantly differ when the self-injected charge is high enough to load the wakefield and influence the trapping process.

The generation of numerical Cherenkov radiation [81] influenced the beam quality for a propagation distance $> 400\mu\text{m}$, even if great effort was made in order to reduce its effect at least along the propagation direction (Appendix D). The suppression of the numerical Cherenkov radiation using a modified version of the FDTD is one of the topic of my current work. Besides, I am working on introducing an online particle tracking routine in ALaDyn to study the transient dynamics of the electrons after ionization without neglecting neither beam loading nor space charge effects.

Finally, our group plans to develop a routine in ALaDyn able to import a plasma density profile from a hydrodynamic code, to study how realistic plasma and dopant distribution affect the generation and the transport of the self-injected beam.

Chapter 6

Conclusion

The work presented in this thesis focuses on the characterization of the Wake-Field Ionization Injection [69][70][71] in the blowout, or bubble, regime of plasma wake-field acceleration. The goal of my work was to develop a plasma injector of high brightness electron beams able to match the requirements of new generation light sources. It was discussed the beam driven Wake-Field-Ionization-Injection as a promising scheme to provide injection and acceleration of high brightness electron beams for future design of plasma based accelerators, and proved its capability to deliver high quality GeV electron beams with few cm-s accelerating devices.

The first two Chapters of this thesis are dedicated to a global review of the concepts of Plasma Wakefield Acceleration theory and numerical methods employed to explore it. The structure of these introductory Chapters was chosen in order to highlight the context and the scientific background wherein our work was developed. In Chapter 2, in particular, the foundations of the kinetic theory for the study of multi-particle systems and the derivation of the cold fluid model were introduced. Its application to plasma acceleration was presented discussing the generation of wake-fields driven by an electron beam in a plasma for different regimes, corresponding to the electron beam current. The analytical model for linear regime and its limitations in terms of

trailing beam properties was presented, as well as the development of the non-linear or blowout regime as the current of the driving beam is raised. The optimal properties of the blowout regime were discussed, in terms of transport (emittance conservation) and acceleration (high transformer ratios). The theory of the background plasma electron trapping in the non-linear plasma wave as an efficient way to self-inject and accelerate electron beams was presented. A threshold in terms of particle energy and wake-fields characteristics was derived and it was eventually discussed the different behaviour of Laser driven plasma wave and Beam driven plasma wave in terms of electron trapping.

In Chapter 3 a review of the state of the art numerical method to investigate plasma acceleration, i.e. the Particle In Cell method, was presented. It was discussed how to model the numerical plasma from the continuous distribution function to the discrete ensemble of numerical macro-particles. A review was given of the numerical integration of the Maxwell equations and the equation of motion for the numerical particles, focusing on the algorithms implemented in the PIC code ALaDyn.

In Chapter 4 the Wake-Field-Ionization-Injection was introduced as a scheme to provide self-injection of high quality electron beams in a beam driven scheme. The trapping condition depending on the potential developed in the bubble was related to the driving beam current, using the scaling laws of the nonlinear regime obtained in Chapter 2. The ADK field ionization model was then reviewed, and a volume in the plasma wake was described, which was called *injection volume*, where both the condition of ionization and trapping are satisfied. It was finally presented a qualitative study of the ionization-injection process via the analysis of the ionization-injected electron dynamics obtained by a Particle Tracking code I developed, where the electrons were treated as test particles moving in the non-evolving plasma wakefield obtained by PIC simulations. It was investigated the

dynamics of three test electrons, representative of three different ionization-injected electron populations, characterized by different injection position inside the injection volume. The choice of the followed electrons was made with the aim of reproducing the envelope dynamics of the self-injected beam.

It was discussed how the electron dynamics is characterized by a fast transient (after the electrons are freed and before they become relativistic) and a long steady state (the electrons become relativistic and co-propagate with the plasma wave). The analysis provided information on how the self-injected beam characteristics, such as trapping energy, beam length, and spot size, depend on the geometry of the injection volume. The shape of the injection volume is approximately an emispherical shell, with varying width along the longitudinal direction (Fig. 4.6, 4.7), and radius $\sim R_b/2$, where R_b is the maximum bubble radius. The transverse dimension of the injection volume determines the initial transverse position of a freed electron, and therefore is related to both the spot size of the self-injected beam (envelope of the trajectories of the test particles), and the beam emittance (spot size and transverse momentum spread). The initial transverse position of the ionization-injected electrons also influences the beam length. The off-axis electrons are trapped , i.e. co-propagate with the wave, backward with respect of the on-axis electrons because of the time necessary to damp their transverse oscillation. Finally, an upper limit of the injected charge can be obtained via multiplying the injection volume times the dopant layer length.

In Chapter 5 the aforementioned electron dynamics analysis was used to predict the self-injected beam properties in a space-charge-free system of forces, and it was presented simple scaling laws for the beam charge, emittance, spot size and energy spread as a function of the injection volume. It was discussed the source of spread in energy for the ionization-injected beam, explaining how it mainly depends

on the beam length and on the dopant layer length. The results of the simulations performed with the PIC code ALaDyn varying the dopant element were presented, choosing the four most successful in terms of delivered beam quality. The setup of the simulations, i.e. driving beam characteristics, plasma density, density and length of the dopant layer, was initially chosen in agreement with the data found in literature [69][70][71], and then adjusted via a preliminary set of simulations that was not presented here. The input data scan was intended to find a scenario where a kA ionization-injected beam presented no more than $1\mu\text{m}$ normalized emittance, fs duration and a few percent of energy spread. It was found as best-case scenario the one employing a $15\mu\text{m}$ layer of dopant element with a percentage of 8 % with respect of the hydrogen plasma background density of $1.2 \times 10^{18} \text{ cm}^{-3}$. In terms of dopant nature, we studied pre-ionized Nitrogen and, in decreasing order of delivered beam quality, pre-ionized Argon, ground state Neon, and pre-ionized Neon. The ionization potentials of the dopant elements, and therefore the injection volumes, do not differ substantially, and this determines similar emittance, energy spread, charge, and current for the delivered beams. Pre-ionized Neon represents the only exception, due to its much higher ionization potential and therefore much smaller injection volume. A comparison between ground state Neon and pre-ionized Neon was presented, to stress the influence of different injection volumes. The injected charge is two orders of magnitude lower for N^{1+} than for N^0 and the emittance is one half, while the energy spread is similar, since the higher charge of N^0 produces positive beam loading effects that compensate a beam length greater than N^{1+} . The comparison with the results of PIC simulations showed reasonable agreement but further studies are needed to consider the transient electron dynamics, corresponding to the acceleration from $v_z = 0$ to $v_z \sim v_\phi$, in presence of space charge forces, which influence both the spot size of the beam, the emittance and the injected charge.

The obtained beam energy spread was highly sensitive to the injected beam charge, since beam loading effects that flatten the accelerating field profile along the beam longitudinal dimension. Again, further studies are needed to take it into account in the scaling laws we presented. In this thesis it was assumed the mixture gas layer to be a sharp edge flat top in density along the longitudinal direction. This configuration is very simple to simulate and reasonably matches, e.g., a realistic supersonic gas-jet profile. However a realistic density distribution of the gas mixture obtained via gas-dynamics simulations must be considered to study possible effects on the self-injected beam properties.

Appendix A

Linear regime full derivation

In this appendix we give a full derivation of the equations ruling the linear regime of plasma acceleration, following the one presented in [23]. We start from the Maxwell equations:

$$\nabla \cdot \mathbf{E}(\mathbf{r}, t) = \frac{\rho(\mathbf{r}, t)}{\varepsilon_0}, \quad (\text{A.1})$$

$$\nabla \cdot \mathbf{B}(\mathbf{r}, t) = 0, \quad (\text{A.2})$$

$$\nabla \times \mathbf{E}(\mathbf{r}, t) = -\frac{\partial \mathbf{B}(\mathbf{r}, t)}{\partial t}, \quad (\text{A.3})$$

$$\nabla \times \mathbf{B}(\mathbf{r}, t) = \mu_0 \mathbf{J}(\mathbf{r}, t) + \varepsilon_0 \frac{\partial \mathbf{E}(\mathbf{r}, t)}{\partial t}. \quad (\text{A.4})$$

Taking the curl of Eq.A.3, and combining the result with the time derivative of Eq.A.4, we obtain the wave equation for the electric field:

$$\left(\nabla^2 - \frac{1}{c^2} \frac{\partial^2}{\partial t^2} \right) \mathbf{E}(\mathbf{r}, t) = \frac{1}{\varepsilon_0} \left(\nabla \rho(\mathbf{r}, t) + \frac{1}{c^2} \frac{\partial \mathbf{j}}{\partial t} \right). \quad (\text{A.5})$$

We can rewrite the wave equation specifying that the charge and current densities

are the superposition of both plasma and beam charge density and current density, namely:

$$\left(\nabla^2 - \frac{1}{c^2} \frac{\partial^2}{\partial t^2} \right) \mathbf{E}(\mathbf{r}, t) = \frac{1}{\varepsilon_0} \nabla (\rho_p(\mathbf{r}, t) + \rho_b(\mathbf{r}, t)) + \frac{1}{\varepsilon_0 c^2} \frac{\partial}{\partial t} (\mathbf{J}_b(\mathbf{r}, t) + \mathbf{J}_p(\mathbf{r}, t)), \quad (\text{A.6})$$

where the subscripts b and p refer, respectively, to the beam and the plasma quantities. From now on we will drop the (\mathbf{r}, t) dependencies for sake of compactness of the equations.

The next step of the derivation is linearization of the cold plasma equations, namely the continuity equation and the momentum equation. We assume the plasma to be initially unperturbed, stationary, unmagnetized and that the perturbation itself is small compared to the equilibrium condition. This assumption means that we can write any quantity as the sum of its equilibrium value and the first order perturbation:

$$\mathbf{E} = \mathbf{E}_0 + \mathbf{E}_1, \quad (\text{A.7})$$

$$\mathbf{B} = \mathbf{B}_0 + \mathbf{B}_1, \quad (\text{A.8})$$

$$\mathbf{u} = \mathbf{u}_0 + \mathbf{u}_1, \quad (\text{A.9})$$

$$\rho_p = \rho_{p0} + \rho_{p1} = e(n_{i0} - n_{e0}) + e(n_{i1} - n_{e1}), \quad (\text{A.10})$$

where the electric and the magnetic field at equilibrium condition are zero because the plasma is assumed to be initially neutral $\rho_{i0} + \rho_{e0} = 0$.

Momentum equation becomes:

$$m_e \left(\frac{\partial}{\partial t} + \mathbf{u}_1 \cdot \nabla \right) \mathbf{u}_1 = -e \mathbf{E}_1, \quad (\text{A.11})$$

$$m_e \frac{\partial}{\partial t} \mathbf{u}_1 = -e \mathbf{E}_1, \quad (\text{A.12})$$

$$\frac{\partial}{\partial t} \mathbf{J}_{1e} = \frac{-e^2 n_e}{m_e} \mathbf{E}_1, \quad (\text{A.13})$$

$$\frac{1}{\varepsilon_0} \frac{\partial}{\partial t} \mathbf{J}_{1e} = \omega_p^2 \mathbf{E}_1, \quad (\text{A.14})$$

where every second order term is dropped. We define $\mathbf{J}_{1e} = -en_{1e}\mathbf{u}_1$, neglecting the ion current due to the much larger ion inertia when compared to the electron inertia. Inserting Eq. A.14 into Eq. A.6 we have:

$$\left(\nabla^2 - k_p^2 - \frac{1}{c^2} \frac{\partial^2}{\partial t^2} \right) \mathbf{E}_1 = \frac{1}{\varepsilon_0} (\nabla \rho_p + \rho_b) + \frac{1}{\varepsilon_0 c^2} \frac{\partial}{\partial t} \mathbf{J}_b. \quad (\text{A.15})$$

Taking the curl of Eq. A.15 and using Eq. A.3 we get:

$$\left(\nabla^2 - k_p^2 - \frac{1}{c^2} \frac{\partial^2}{\partial t^2} \right) \mathbf{B}_1 = -\frac{1}{\varepsilon_0 c^2} (\nabla \times \mathbf{J}_b). \quad (\text{A.16})$$

From now on we will drop the indices 1 so that the quantities we will refer to have to be recognized as perturbed quantities.

Since we are mainly interested in the phenomena developing behind the trailing beam, we will perform a change of variable introducing $\xi = ct - z$, so that the time derivative becomes $\frac{\partial}{\partial t} = c \frac{\partial}{\partial \xi}$ and the longitudinal derivative becomes $\frac{\partial}{\partial z} = -\frac{\partial}{\partial \xi}$.

The LHS of Eqs. A.15 and A.16 expand like:

$$\begin{aligned}
\nabla^2 - k_p^2 - \frac{1}{c^2} \frac{\partial^2}{\partial t^2} &= \frac{\partial^2}{\partial r^2} + \frac{1}{r} \frac{\partial}{\partial r} + \frac{1}{r^2} \frac{\partial^2}{\partial \phi^2} + \frac{\partial^2}{\partial z^2} - k_p^2 - \frac{1}{c^2} \frac{\partial^2}{\partial t^2} \\
&= \frac{\partial^2}{\partial r^2} + \frac{1}{r} \frac{\partial}{\partial r} + \frac{1}{r^2} \frac{\partial^2}{\partial \phi^2} + \frac{1}{c^2} \frac{\partial^2}{\partial \xi^2} - k_p^2 - \frac{1}{c^2} \frac{\partial^2}{\partial t^2} \\
&= \nabla_{\perp}^2 - k_p^2
\end{aligned} \tag{A.17}$$

Assuming that the source term, and therefore the density perturbation is axisymmetric ($\mathbf{J}_b = \hat{z} c \rho_b$), we find that Eqs. A.15 and A.16 become:

$$\left(\nabla_{\perp}^2 - k_p^2 \right) \mathbf{E}_1 = \frac{\hat{r}}{\varepsilon_0} \frac{\partial}{\partial r} (\rho_p + \rho_b), \tag{A.18}$$

$$\left(\nabla_{\perp}^2 - k_p^2 \right) \mathbf{B}_1 = \frac{\hat{\phi}}{\varepsilon_0 c} \frac{\partial}{\partial r} \rho_b. \tag{A.19}$$

We use now the linearized continuity equation in order to express the plasma density perturbation ρ_p as a function of the beam density. The linearized density perturbation is given by:

$$\frac{\partial n_e}{\partial t} + \nabla \cdot (n_e \mathbf{u}) = 0, \tag{A.20}$$

$$\frac{\partial n_{e1}}{\partial t} + \nabla \cdot ((n_{e0} + n_{e1}) \mathbf{u}_1) = 0, \tag{A.21}$$

$$\frac{\partial n_{e1}}{\partial t} + n_0 \nabla \cdot (\mathbf{u}_1) = 0. \tag{A.22}$$

We drop the 1 index, take the partial time derivative and insert it into the linearized momentum equation and get:

$$\frac{\partial^2 n_e}{\partial t^2} - \frac{n_0 e}{m_e} \nabla \cdot (\mathbf{E}) = 0. \tag{A.23}$$

Via Eq. A.1 and using the co-moving variable ξ we finally obtain:

$$\left(\frac{\partial^2}{\partial \xi^2} + k_p^2 \right) \rho_p = -k_p^2 \rho_p. \quad (\text{A.24})$$

It is useful now to solve the system of Eqs. A.18,A.19 and A.24 in Fourier space. Assuming that $\rho_p, \rho_b, \mathbf{E}$ and \mathbf{B} have the Fourier integral representation $f(\mathbf{r}, \xi) = \frac{1}{2\pi} \int_{-\infty}^{\infty} \tilde{f}(\mathbf{r}, k) e^{-ik\xi} dk$, we can solve the density perturbation equation for the inverse Fourier transform of the plasma density:

$$\tilde{\rho}_p = \frac{k_p^2}{k^2 - k_p^2} \tilde{\rho}_b. \quad (\text{A.25})$$

We insert this result into the Fourier transformed Eqs. A.18 and A.19 and obtain:

$$\left(\nabla_{\perp}^2 - k_p^2 \right) \tilde{\mathbf{E}} = \frac{\hat{r}}{\varepsilon_0} \frac{\partial}{\partial r} \frac{k^2}{k^2 - k_p^2} \tilde{\rho}_b + \frac{\hat{z}ik}{\varepsilon_0} \tilde{\rho}_b \left(\frac{k_p^2}{k^2 - k_p^2} \right), \quad (\text{A.26})$$

$$\left(\nabla_{\perp}^2 - k_p^2 \right) \tilde{\mathbf{B}} = \frac{\hat{\phi}}{\varepsilon_0 c} \frac{\partial}{\partial r} \tilde{\rho}_b. \quad (\text{A.27})$$

A way to solve Eqs. A.26 and A.27 is to first find the transverse Green's function associated to the LHS operator of the general inhomogeneous equation:

$$\left(\nabla_{\perp}^2 - k_p^2 \right) G(\mathbf{x}, \mathbf{x}') = \frac{1}{r} \delta(r - r') \delta(\phi - \phi'), \quad (\text{A.28})$$

where we dropped the azimuthal symmetry in order to obtain a more general solution [84]. We expand the angle dependent Dirac delta function as $\delta(\phi - \phi') =$

$\frac{1}{2\pi} \sum_{m=-\infty}^{\infty} e^{im(\phi-\phi')}$ and similarly the Green's function as:

$$G(\mathbf{x}, \mathbf{x}') = \frac{1}{2\pi} \sum_{m=-\infty}^{\infty} e^{im(\phi-\phi')} g_m(k_p, r, r'), \quad (\text{A.29})$$

where g_m is the m^{th} term of the polynomial expansion of the radial Green's function.

If we insert Eq. A.29 into Eq. A.28 we get:

$$\left(\nabla_{\perp}^2 - k_p^2 \right) \frac{1}{2\pi} \sum_{m=-\infty}^{\infty} e^{im(\phi-\phi')} g_m(k_p, r, r') = \frac{1}{r} \delta(r - r') \delta(\phi - \phi'), \quad (\text{A.30})$$

$$\left(\frac{\partial^2}{\partial r^2} + \frac{1}{r} \frac{\partial}{\partial r} + \frac{1}{r^2} \frac{\partial^2}{\partial \phi^2} \right) \left(\frac{1}{2\pi} \sum_{m=-\infty}^{\infty} e^{im(\phi-\phi')} g_m(k_p, r, r') \right) = \frac{1}{r} \delta(r - r') \delta(\phi - \phi'), \quad (\text{A.31})$$

$$\frac{1}{2\pi} \sum_{m=-\infty}^{\infty} e^{im(\phi-\phi')} \left[\frac{\partial^2}{\partial r^2} + \frac{1}{r} \frac{\partial}{\partial r} + \left(\frac{m^2}{k_p^2} + k_p^2 \right) \right] g_m(k_p, r, r') = \frac{1}{r} \delta(r - r') \delta(\phi - \phi'). \quad (\text{A.32})$$

The radial equation must be satisfied for each m , and we can prove that for $r \neq r'$ the radial equation is just the equation for the modified Bessel functions $I_m(k_p r), K_m(k_p r)$.

The solution which satisfies the boundary condition is therefore:

$$g_m(k_p, r, r') = -I_m(k_p r_{<}) K_m(k_p r_{>}) \quad (\text{A.33})$$

where the arguments of the modified Bessel function $r_{<}$ and $r_{>}$ denote respectively the minimum and the maximum values of r and r' .

We write the final form of the Green's function in terms of real functions using the symmetry of the cosine function:

$$G(\mathbf{x}, \mathbf{x}') = -\frac{1}{2\pi} \left(I_0(k_p r_{<}) K_0(k_p r_{>}) \sum_{m=1}^{\infty} 2 \cos[m(\phi - \phi')] I_m(k_p r_{<}) K_m(k_p r_{>}) + \right). \quad (\text{A.34})$$

Now before we convolve the Green's function with the real density perturbation we must convert the unit vectors $\hat{r} = \cos \phi \hat{x} + \sin \phi \hat{y}$ and $\hat{\phi} = -\sin \phi \hat{x} + \cos \phi \hat{y}$ because of the integration over the azimuthal angle. We write the Fourier transform of the fields as:

$$\tilde{E}_z(r, k) = \frac{ik}{\varepsilon_0} \left(\frac{k_p^2}{k^2 - k_p^2} \right) \int \tilde{\rho}_b(r', k) G(\mathbf{x}, \mathbf{x}') r' dr' d\phi', \quad (\text{A.35})$$

$$\tilde{E}_r(r, k) = \frac{1}{\varepsilon_0} \frac{k^2}{k^2 - k_p^2} \int \frac{\partial}{\partial r} \tilde{\rho}_b(r', k) (\cos \phi' \hat{x} + \sin \phi' \hat{y}) G(\mathbf{x}, \mathbf{x}') r' dr' d\phi', \quad (\text{A.36})$$

$$\tilde{B}_\phi(r, k) = \frac{1}{\varepsilon_0 c} \int \frac{\partial}{\partial r} \tilde{\rho}_b(r', k) (-\sin \phi' \hat{x} + \cos \phi' \hat{y}) G(\mathbf{x}, \mathbf{x}') r' dr' d\phi'. \quad (\text{A.37})$$

If we now come back to assume cylindrical symmetry we notice how the integration over the azimuthal angle leads to drop every m term of the summation but them = 0 index in Eq. A.35, because the cosine is an even function

$$\tilde{E}_z(r, k) = -\frac{ik}{\varepsilon_0} \left(\frac{k_p^2}{k^2 - k_p^2} \right) \int \tilde{\rho}_b(r', k) I_0(k_p r_{<}) K_0(k_p r_{>}) r' dr. \quad (\text{A.38})$$

Similarly, in Eqs. A.36 and A.37 only the $m = 1$ index survives because $\sin_m(\phi)$ and $\cos_l(\phi)$ are orthonormal functions:

$$\tilde{E}_r(r, k) = -\frac{1}{\varepsilon_0} \frac{k^2}{k^2 - k_p^2} \int \frac{\partial}{\partial r} \tilde{\rho}_b(r', k) I_1(k_p r_{<}) K_1(k_p r_{>}) r' dr', \quad (\text{A.39})$$

$$\tilde{B}_\phi(r, k) = -\frac{1}{\varepsilon_0 c} \int \frac{\partial}{\partial r} \tilde{\rho}_b(r', k) I_1(k_p r_{<}) K_1(k_p r_{>}) r' dr'. \quad (\text{A.40})$$

Now the equations can be inverted and we will show the example of inverting the longitudinal field equation Eq. A.38:

$$E_z(r, \xi) = -\frac{i}{\varepsilon_0} \int I_0(k_p r_{<}) K_0(k_p r_{>}) r' dr' \frac{1}{2\pi} \int e^{-ik\xi} k \left(\frac{k_p^2}{k^2 - k_p^2} \right) \tilde{\rho}_b(r', k) dk \quad (\text{A.41})$$

We start recognize that once we integrate on the k domain, Eq. A.38 is just a form of the convolution theorem $f * g = \mathcal{F}^{-1}\{\mathcal{F}\{f\}\mathcal{F}\{g\}\}$ with:

$$f(r', \xi) = \rho_b(r', \xi), \quad (\text{A.42})$$

$$g(r', \xi) = \frac{1}{2\pi} \int k e^{ik\xi} \left(\frac{k_p^2}{k^2 - k_p^2} \right) d\xi. \quad (\text{A.43})$$

Therefore Eq. A.38 becomes:

$$\begin{aligned} E_z(r, \xi) &= -\frac{i}{\varepsilon_0} \int I_0(k_p r_{<}) K_0(k_p r_{>}) r' dr' \\ &\quad \frac{1}{2\pi} \int_{-\infty}^{\infty} \rho_b(r', \xi') d\xi' \int_{-\infty}^{\infty} k e^{-ik(\xi - \xi')} \left(\frac{k_p^2}{k^2 - k_p^2} \right) dk = \\ &= -\frac{i}{\varepsilon_0} \int I_0(k_p r_{<}) K_0(k_p r_{>}) r' dr' \\ &\quad \frac{1}{2\pi} \int_{-\infty}^{\infty} \rho_b(r', \xi') d\xi' \int_{-\infty}^{\infty} k e^{-ik(\xi - \xi')} \left(\frac{1}{k - k_p} + \frac{1}{k + k_p} \right) dk \end{aligned} \quad (\text{A.44})$$

The integral on k has two simple poles at $k = \pm k_p$, but we can greatly simplify the integration along a complex contour if we substitute $k = k - i\epsilon$. With this substitution we are assuming that the poles reside in the upper half of the complex plane, and therefore when performing the limit of the arc radius to infinity, only the

terms with negative sign of $(\xi - \xi')$ contribute to the integral. This constraint has a physical implication, regarding the part of the source beam contributing to the electric field at location ξ . In the ultra-relativistic limit, because of causality, only the charge in front of the infinitesimal slice at ξ gives contribute, and therefore the choice of positive or negative sign directly implies the propagation direction in the negative or positive \hat{z} direction, respectively.

Using theorem of residues we get:

$$\begin{aligned} Res(f, \pm k_p + i\epsilon) &= \lim_{k \rightarrow \pm k_p + i\epsilon} (k - (\pm k_p + i\epsilon)) f(k) = \\ &= \left(1 \mp \frac{i\epsilon}{k_p \mp i\epsilon} \right) e^{-i(\pm k_p - 2i\epsilon)(\xi - \xi')}, \end{aligned} \quad (\text{A.45})$$

and therefore

$$\int_{-\infty}^{\infty} k e^{-ik(\xi - \xi')} \left(\frac{1}{k - k_p} + \frac{1}{k + k_p} \right) dk = \begin{cases} ik_p^2 \cos[k_p(\xi - \xi')], (\xi - \xi') < 0, \\ 0, (\xi - \xi') > 0. \end{cases} \quad (\text{A.46})$$

We use a similar method to integrate Eqs. A.39 and A.40, and finally get the fields in the space domain as:

$$E_z(r, \xi) = \frac{k_p^2}{\varepsilon_0} \int I_0(k_p r_<) K_0(k_p r_>) r' dr' \int_{\xi}^{\infty} \rho_b(r', \xi') \cos[k_p(\xi - \xi')] d\xi, \quad (\text{A.47})$$

$$E_r(r, \xi) = -\frac{k_p}{\varepsilon_0} \int I_1(k_p r_<) K_1(k_p r_>) r' dr' \int_{\xi}^{\infty} \frac{\partial}{\partial r'} \rho_b(r', \xi') \sin[k_p(\xi - \xi')] d\xi, \quad (\text{A.48})$$

$$B_{\phi}(r, \xi) = -\frac{\beta}{c\varepsilon_0} \int I_1(k_p r_<) K_1(k_p r_>) \frac{\partial}{\partial r'} \rho_b(r', \xi') r' dr'. \quad (\text{A.49})$$

We should be careful with Eqs. A.47,A.48 and A.49, because if we perform the limit for $k_p \rightarrow 0$ in the radial component of the electric field, i.e. we calculate the field of a bare beam, we find it goes to zero too, which is obviously unphysical. This happens, as reported in [23], because we performed the ultra-relativistic approximation before inverting the Fourier transform equations. On the other hand, if we invert this order we find back the complete radial field with the extra term of the beam in absence of plasma:

$$E_r(r, \xi) = -\frac{k_p}{\varepsilon_0} \int I_1(k_p r_{<}) K_1(k_p r_{>}) r' dr' \frac{\partial}{\partial r'} (-\rho_b(r', \xi)) + \quad (\text{A.50})$$

$$+ \int_{\xi}^{\infty} \sin[k_p(\xi - \xi')] \rho_b(r', \xi') d\xi' \quad (\text{A.51})$$

Appendix B

Wave breaking and trajectory crossing

In this Appendix we derive the condition for trajectory crossing for both 1D plasma oscillation and 2D cylindrical oscillation, and discuss the non-linear dynamic behaviour of the plasma wave, following the derivation in [6][85].

We start from a simple 1D linear non-relativistic electron sheet model, considering the displacement ξ of a thin electron sheet from its equilibrium position $x = x_0$. The displacement of the electron sheet leaves behind a net positive charge $q^+ = en_0\xi$, corresponding to the electric field $E(\xi) = \frac{en_0}{\varepsilon_0}\xi$, which pulls back the electrons towards their initial position. Assuming the density perturbation, and therefore the displacement, to be small with respect to the equilibrium condition, we can write the equation of motion as:

$$m \frac{d^2\xi}{dt^2} = -eE(\xi) \rightarrow \frac{d^2\xi}{dt^2} + \frac{e^2n_0}{m\varepsilon_0}\xi = 0, \quad (\text{B.1})$$

where m , e are the electron mass and charge, and the coefficient of the electric field

is the square of the plasma frequency $\omega_p = \sqrt{\frac{e^2 n_0}{m \varepsilon_0}}$. The solution of the Eq. B.1 is a harmonic function $\xi(x_0, t) = A_1(x_0) \cos(\omega_p t) + A_2(x_0) \sin(\omega_p t)$, where the amplitude is a function of the initial condition x_0 .

The assumption of linearity of the model holds until each of the electron sheets executes simple harmonic oscillation without intersecting one another. In other terms, if we consider another electron sheet with instantaneous position $x_2 = x_0 + \Delta x_0 + \xi_2$, in order to keep the linearity its oscillation must not cross the ones of the previous one, i.e. $\xi_2 + \Delta x_0 > \xi$. It is possible to derive a condition under which the non-crossing condition, and thus the linear approximation holds:

$$\lim_{\Delta x_0 \rightarrow 0} \frac{\Delta \xi}{\Delta x_0} = \lim_{\Delta x_0 \rightarrow 0} \frac{\xi_2 - \xi}{\Delta x_0} > \frac{\xi - \Delta x_0 - \xi}{\Delta x_0} = -1, \quad (\text{B.2})$$

and therefore simply $\frac{\partial \xi}{\partial x_0} > -1$.

We use this condition to derive a constraint on the initial energy ensuring that the linearity is preserved: the total energy associated to the oscillation is $\mathcal{E} = \frac{1}{2} \left(\frac{d\xi}{dt} \right)^2 + \frac{1}{2} \omega_p^2 \xi^2$, where the first term on the RHS corresponds to the kinetic energy of the sheet and the second to the ‘elastic’ potential energy. We differentiate Eq.B.1 with respect to the initial position x_0 and, since $\partial \xi / \partial x_0$ is a solution of the equation of motion as well as ξ , we find:

$$\mathcal{E} = \frac{1}{2} \left(\frac{d}{dt} \frac{\partial \xi}{\partial x_0} \right)^2 + \frac{1}{2} \omega_p^2 \left(\frac{\partial \xi}{\partial x_0} \right)^2. \quad (\text{B.3})$$

We apply the condition of non-crossing oscillations $\partial \xi / \partial x_0 > -1$ and find that the condition for the initial energy to maintain the ordering of the sheets holds if:

$$\mathcal{E}|_{t=0} < \frac{\omega_p^2}{2}, \quad (\text{B.4})$$

where for initial energy we mean the energy corresponding to the $d\xi/dt = 0$ condition, i.e. for $t = 0$ and any inversion point.

To understand the onset of the non-linear solution we show in Fig. B.1 the solution of the equation of motion with the particular initial conditions $A_1(x_0) = A \sin(kx_0)0$, $A_2(x_0) = 0$. We have $\xi(x_0, t) = A \sin(kx_0) \cos(\omega_p t)$, which gives the instantaneous position $x = x_0 + A \sin(kx_0)$ and the electric field $E = \frac{en_0}{\varepsilon_0} A \sin(kx_0)$ at $t = 2n\pi$. If we solve and plot $E(x)$ for different values of A , we see that when $A \geq \frac{1}{k}$ the electric field solution is no more a single valued function, meaning that the linear model is no longer valid. We obtain:

$$E = \frac{mc\omega_p}{e} \sin(kx_0) \cos(\omega_p t), \quad (\text{B.5})$$

where the amplitude is the well known 1D non-relativistic Wave-breaking limit we have already introduced, and we have defined $k = \frac{\omega_p}{c}$. If the amplitude of the oscillation determines an electric field whose amplitude exceeds $mc\omega_p/e$, a fine-scale phase mixing of various regions of the oscillation occurs, and the harmonic behaviour of the oscillations is destroyed.

In order to study the onset of trajectory crossing in 2D cylindrically symmetric geometry, we start from the momentum equation for an electron in an electrostatic cylindrical wave $\frac{d^2r}{dt^2} = -\frac{e}{m} E_r$, where E_r is the radial electric field. We obtain via Gauss's law, assuming a radial displacement of a thin shell of electron due to the charge of a bi-flat top beam:

$$n_b(r, \xi) = \begin{cases} n_b, & r < a, 0 < \xi < L \\ 0, & \text{otherwise,} \end{cases} \quad (\text{B.6})$$

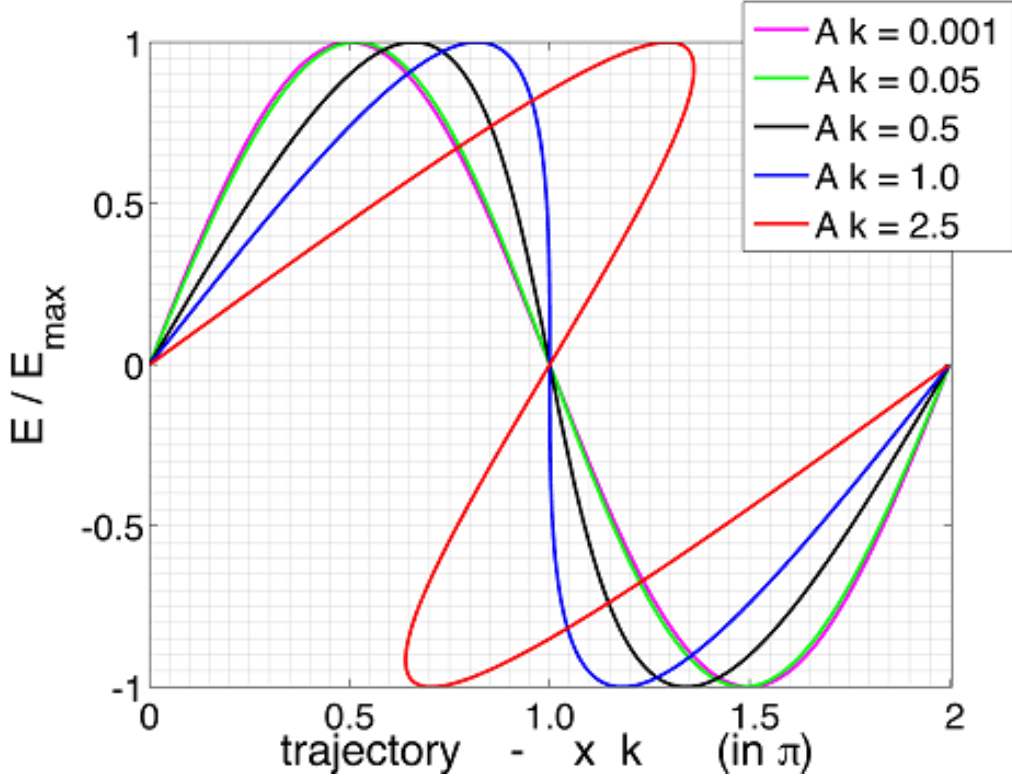


Figure B.1. Normalized electric field profile in a plasma with planar oscillation with respect of the instantaneous position of an electron sheet. As the amplitude of the oscillation approaches the value $1/k$, where k is the wavenumber of the electrostatic wave, the electric field tends to a multi-valued function of space, obviously unphysical, meaning the breaking of the linear model.[85]

where a is the radial dimension of the beam, and L its longitudinal dimension. We also assume that the plasma current induced fields are negligible and that the plasma electrons remain non-relativistic. The momentum equation for the instantaneous radial position $r(r_0, t) = r_0 + R(r_0, t)$, where $R(r_0, t)$ is the radial displacement, therefore becomes:

$$\begin{aligned} \frac{d^2r(r_0, t)}{dt^2} &= -\frac{\omega_p^2}{2} \left[\frac{(r_0 + r(r_0, t)^2 - r_0^2)}{r_0 + r(r_0, t)} - eE_b(r) \right] = \\ &= -\frac{\omega_p^2}{2} \left\{ r(r_0, t) - \frac{r_0^2}{r(r_0, t)} - eE_b(r) \right\}, \end{aligned} \quad (\text{B.7})$$

where the beam radial field $E_b(r)$ depends linearly on r if the initial position of the electron shell is $r_0 < a$, whereas it scales as $1/r$ for $r_0 > a$. We focus on the $r_0 > a$ condition but it can be proved [36] that for $r_0 < a$ the derivation is similar and the result is the same.

Momentum equation for an electron shell at initial position $r_0 > a$ is therefore

$$\frac{d^2r}{dt^2} = -\frac{\omega_p^2}{2} \left\{ r(r_0, t) - \frac{1}{r(r_0, t)} \left[r_0^2 + \frac{n_b}{n_0} a^2 \right] \right\}, \quad (\text{B.8})$$

i.e. a differential equation for the radial displacement as a function of both time and initial position r_0 of the electron shell. The solutions are shown in Fig. B.2 for different values of r_0 and two different values of n_b .

Trajectory crossing occurs where the radial force that pushes away the electrons is such that for $r_{01} < r_{02}$ we have $r_{m1} > r_{m2}$, where r_m is the maximum radial position. It means that $r_m(r_0)$ is not a monotonous increasing function but changes to a function having local maxima/minima. We have to find some explicit expression of $r_m = r_m(r_0)$ and we start to do it by integrating the equation of motion in order to obtain the potential energy:

$$\phi(r, r_0) = \frac{\omega_p^2}{4} \left\{ -r^2 + r_0^2 \left[2 \ln \left(\frac{r}{r_0} \right) \left(\alpha \frac{a^2}{r_0^2} + 1 \right) + 1 \right] \right\}, \quad (\text{B.9})$$

where we defined $\alpha = n_b/n_0$ the normalized beam density. Since the velocity of the electron shell is zero at both the extreme values of the oscillation, i.e. $r = r_m$ and $r = r_0$, the potential energy in these positions must be the same, $\phi(r_m, r_0) = \phi(r_0, r_0)$:

$$r_m^2 - r_0^2 = r_0^2 \ln \left(\frac{r_m^2}{r_0^2} \right) \left(1 + \alpha \frac{a^2}{r_0^2} \right). \quad (\text{B.10})$$

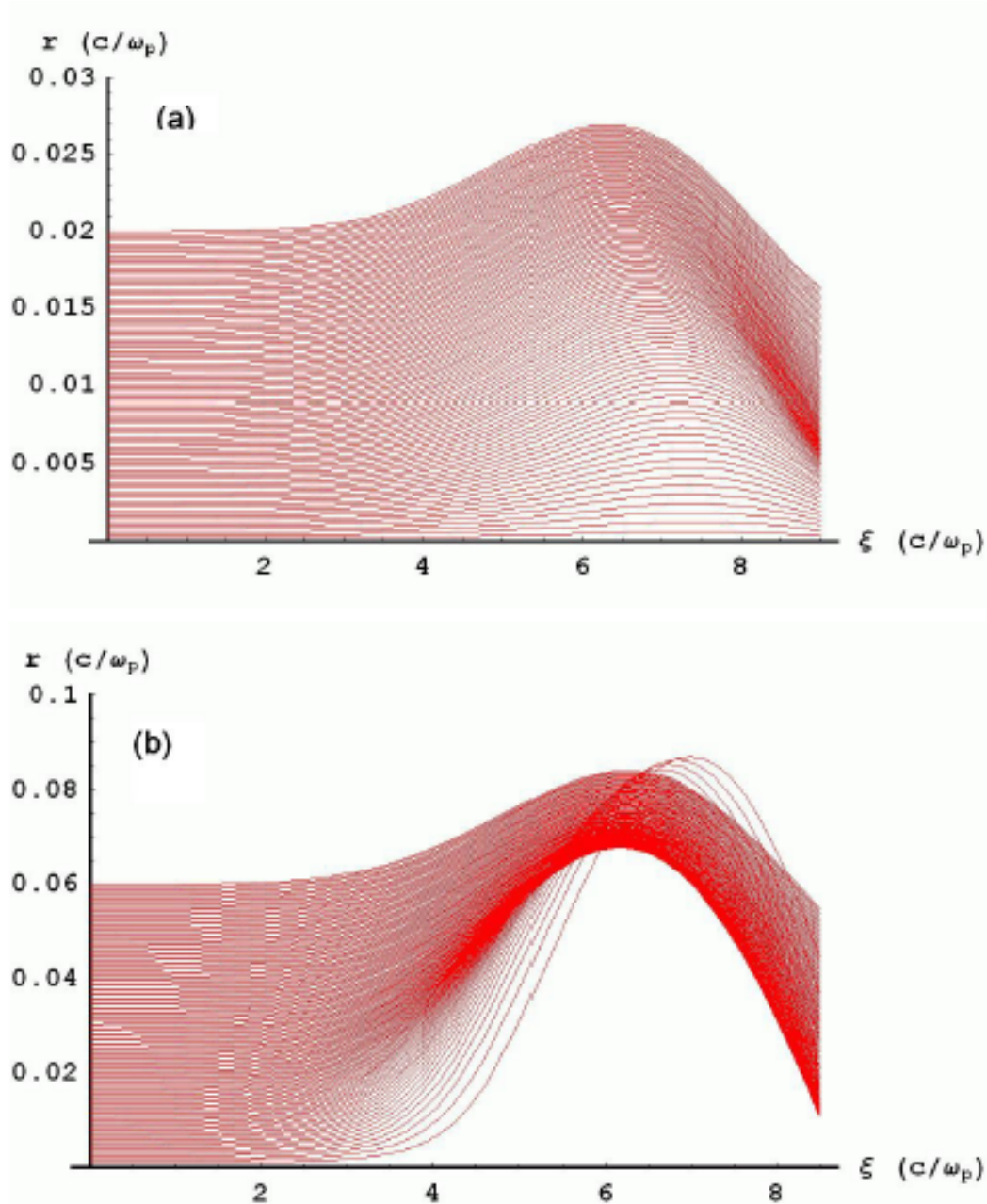


Figure B.2. Plot of trajectories for different initial radial positions r_0 , for a) $\alpha = 1$ and b) $\alpha = 10$. [36]

By differentiating Eq. B.10 with respect to r_0 we obtain:

$$\frac{dr_m}{dr_0} = \frac{\frac{r_m}{r_0} \left(\ln \frac{r_m^2}{r_0^2} \right) - \alpha \frac{a^2}{r_0^2}}{\left(\alpha \frac{a^2}{r_0^2} + 1 \right) \ln \frac{r_m^2}{r_0^2} - \alpha \frac{a^2}{r_0^2}}. \quad (\text{B.11})$$

Equation B.11 shows that for $r_0 \rightarrow \infty$ $\frac{dr_m}{dr_0} \rightarrow 1$, which means that for sufficiently large r_0 , no trajectory crossing occurs. On the other hand, the maximum of $r_m(r_0)$, and thus trajectory crossing, occurs for $\ln \frac{r_m^2}{r_0^2} - \alpha \frac{a^2}{r_0^2} = 0$. We call r_{0m} the initial radial position which defines the onset of trajectory crossing. Combining Eqs. B.11 and B.10 we obtain:

$$1 + \left(\alpha \frac{a^2}{r_{0m}^2} + 1 \right) \ln \frac{r_m^2}{r_{0m}^2} = e^{\alpha \frac{a^2}{r_{0m}^2}}, \quad (\text{B.12})$$

which has non-zero solution for $s = \alpha \frac{a^2}{r_{0m}^2} = 1.7933$. We obtain the initial radial position and the maximum radius for which trajectory crossing occurs as:

$$r_{0m} = 0.747a\sqrt{\alpha}, \quad (\text{B.13})$$

$$r_m(r_{0m}) = 1.831\sqrt{\alpha}, \quad (\text{B.14})$$

where we remember that the derivation we performed started assuming $r_0 > a$, and it implies that we have a condition on the normalized beam density for trajectory crossing to occur as $\alpha > 1.792$ [50].

We already said that the result one could obtain assuming $r_0 < a$ is the same as the one we have deduced so far, however paying attention to add the kinetic energy of the electrons to the potential energy when they reach $r = a$. In this configuration, electrons with $r_0 = 0$ simply pass through the beam without feeling any deflection. The normalized beam density for which $r_m(r_0)$ presents a local maximum is the same value for $r_0 > a$. If we raise the beam density, the radius for which trajectory crossing occurs will move toward zero, which means that a greater amount of electron passing through the beam will be blown out.

We can rewrite r_{max} as a function of the normalized charge per unit length $\Lambda = \int r \alpha dr$, being $\Lambda = \alpha \frac{a^2}{2}$ for the simplified flat top profile, and obtain a scaling law

for the maximum blowout radius: $r_{max} = 2.58\Lambda^{1/2}$. Such a value is very close to the results of PIC simulation with Gaussian profiles, $r_{max} \sim 2\Lambda^{1/2}$, where the larger value of the constant factor comes from the use of a flat-top beam profile with a density corresponding to the maximum density of the Gaussian profile.

Appendix C

Boris pusher algorithm

In this Appendix we want to derive the so-called *Boris Method* equations [64], one of the most widely implemented algorithm to perform integration of the equation of motion in PIC codes.

The integration of the equation of motion for both relativistic and non-relativistic particles in PIC codes is usually performed through a leapfrog method, to achieve second-order accuracy in time of the algorithm. In this method position and velocity are not defined at the same time-step but half integer time-step one ahead another, similarly as it is done for the electric and magnetic field.

The leapfrog method is used to numerically solve the symplectic system of differential equations:

$$\hat{\mathbf{u}} = \frac{q}{m} \mathbf{F}, \quad (\text{C.1})$$

$$\hat{\mathbf{x}} = \frac{\mathbf{u}}{\gamma}, \quad (\text{C.2})$$

where $\mathbf{u} = \gamma \mathbf{v}$ and \mathbf{F} is the Lorentz force . In terms of finite difference, the equations we need to solve are:

$$\frac{\mathbf{u}^{n+1/2} - \mathbf{u}^{n-1/2}}{\Delta t} = \frac{q}{m} \mathbf{F}^n, \quad (\text{C.3})$$

$$\frac{\mathbf{x}^{n+1} - \mathbf{x}^n}{\Delta t} = \frac{\mathbf{u}^{n+1/2}}{\gamma^{n+1/2}}. \quad (\text{C.4})$$

At n^{th} simulation time-step the quantities of interest are defined at times \mathbf{x}^n , $\mathbf{u}^{n-1/2}$, \mathbf{E}^n and $\mathbf{B}^{n-1/2}$. Since the fields are defined at the grid points of a Eulerian grid we have to interpolate them onto the Lagrangian macro-particles in a way that is consistent with the current deposition and for such a reason we use the same shape functions we previously used.

In order to have the Lorentz force at time n we first need to advance the magnetic field for half a time-step using \mathbf{E}^n . Then we add half acceleration via the electric field \mathbf{E}^n , obtaining an estimate of the \mathbf{u} at time $n\Delta t$:

$$\mathbf{u}' = \mathbf{u}^{n-1/2} + \frac{q}{m} \frac{\Delta t}{2} \mathbf{E}^n. \quad (\text{C.5})$$

With this value we have an estimate also for the time centred Lorentz factor $\gamma' = \sqrt{1 + u'^2}$, which we will use to add the magnetic force to the acceleration. The magnetic force does not provide acceleration in the direction of motion, but they actually are the reason of a rotation of the velocity vector in space by an angle $\theta = -2 \arctan(\frac{qB\Delta t}{\gamma m c})$. Therefore we are able to perform half rotation of the velocity vector and use the result to complete the rotation, before to add the remaining electric impulse:

$$\mathbf{u}'' = \mathbf{u}' + \frac{q}{m} \frac{\Delta t}{2} \frac{\mathbf{u}'}{\gamma'} \times \mathbf{B}^n, \quad (\text{C.6})$$

$$\mathbf{u}''' = \mathbf{u}' + \frac{q}{m} \Delta t \frac{\mathbf{u}''}{\gamma'} \times \mathbf{B}^n, \quad (\text{C.7})$$

$$\mathbf{u}^{n+1/2} = \mathbf{u}''' + \frac{q}{m} \frac{\Delta t}{2} \mathbf{E}^n. \quad (\text{C.8})$$

Finally, having $\mathbf{u}^{n+1/2}$, we compute the Lorentz factor at half time-step in order to advance the particle position and close the loop.

$$\gamma^{n+1/2} = \sqrt{1 + (u^{n+1/2})^2}, \quad (\text{C.9})$$

$$\mathbf{x}^{n+1} = \mathbf{x}^n + \Delta t \frac{\mathbf{u}^{n+1/2}}{\gamma^{n+1/2}}. \quad (\text{C.10})$$

In electromagnetic PIC codes particles are bounded not to move more than a cell per time-step, since otherwise higher frequency waves would not be properly sampled by simulation particles. Once the spatial resolution is defined because of the problem we want to study (laser wavelength in laser driven plasma acceleration, plasma skin depth for beam driven plasma acceleration), the time resolution is given by the *Courant – Friedrichs – Levy* condition, which we have already mentioned for the stability of the field integration algorithm. This stability criterium for the fields evolution actually enforces the bounds of the particle motion, so that it is not relevant for the choice of the time-step.

Appendix D

Anisotropic wave propagation mitigation for FDTD-Yee lattice

In this appendix we will show how the FDTD-Yee lattice we use to numerically integrate the Maxwell equations intrinsically introduces errors in the dispersion relation which can induce the development of numerical instabilities affecting the quality of the trailing beam. We will study, as a simplified example, the 2D wave propagation of the electric field for the standard leapfrog+FDTD two-point finite-differences algorithm (*Lpf2 + SE2*) and for an optimized leapfrog+FDTD four point-finite differences algorithm (*Lpf2 + OSE2*), able to reduce the anisotropy of the wave propagation and thus to mitigate emittance and energy spread growth of a trailing beam.

In the standard *Lpf2 + SE2* algorithm the wave equation is discretized by:

$$[\mathcal{D}_t^2] \psi_{i,j}^n = [\mathcal{D}_x^2 + \mathcal{D}_y^2] \psi_{i,j}^n, \quad (\text{D.1})$$

where,

$$[\mathcal{D}_t^2]\psi_{i,j} = \frac{1}{\Delta t^2}[\psi_{i,j}^{n+1} - 2\psi_{i,j}^n + \psi_{i,j}^{n-1}], \quad (\text{D.2})$$

$$[\mathcal{D}_x^2]\psi_{i,j} = \frac{1}{h_x^2}[\psi_{i+1,j} - 2\psi_{i,j} + \psi_{i-1,j}], \quad (\text{D.3})$$

$$[\mathcal{D}_y^2]\psi_{i,j} = \frac{1}{h_y^2}[\psi_{i,j+1} - 2\psi_{i,j} + \psi_{i,j-1}], \quad (\text{D.4})$$

where we can assume for simplicity to have a square computational box of size $h = h_x = h_y$, and ψ can be one component of either electric and the magnetic field. The numerical dispersion relation is obtained via Fourier analysis assuming the fields are the superposition of plane wave such that $\psi = \sum_k \psi_k e^{(-i\omega_k t + i\mathbf{k} \cdot \mathbf{x})}$. We have:

$$\frac{1}{(c\Delta t)^2} \sin^2 \frac{\omega_k \Delta t}{2} = \frac{1}{h^2} \left(\sin^2 \frac{k_x \Delta x}{2} + \sin^2 \frac{k_y \Delta y}{2} \right), \quad (\text{D.5})$$

instead of the analytic dispersion relation $\omega_k = c|\mathbf{k}|$. Using polar coordinates (w, θ) , where $w = kh = \sqrt{w_x^2 + w_y^2}$ and $\theta = \arctan(w_y/w_x)$ we obtain:

$$\frac{1}{(c\Delta t)^2} \sin^2 \frac{\omega_k \Delta t}{2} = 4[\sin^2(w \cos \theta/2) + \sin^2(w \sin \theta/2)]. \quad (\text{D.6})$$

For the 2D square box case we are examining the time-step is bounded by the CFL condition $\Delta t = \tilde{\sigma}h = \frac{\sigma}{\sqrt{2}}h$, where typically $\sigma = 0.7 - 0.9$. We can write the phase velocity of the wave $v_\phi = \omega_k/k$ in the explicit form:

$$v_\phi(w, \theta) = \frac{\arcsin[\tilde{\sigma}\sqrt{\sin^2(w \cos \theta/2) + \sin^2(w \sin \theta/2)}]}{w\tilde{\sigma}/2}. \quad (\text{D.7})$$

In order to evaluate the dependence of the phase velocity by the angle of wave

propagation, we Taylor-expand the sin functions for $w/2 < 1$, and get:

$$v_\phi^2 = 1 - \frac{1}{12}w^2 \left[\cos^4 \theta + \sin^4 \theta - \frac{\sigma^2}{2} \right] + \mathcal{O}(w^4), \quad (\text{D.8})$$

where, since the exact relation in dimensionless quantities would read $v_\phi = 1$, we have a 2nd order truncation error $\epsilon = \left[\cos^4 \theta + \sin^4 \theta - \frac{\sigma^2}{2} \right]$, which attains a minimum for $\theta = \pi/4 \rightarrow \epsilon_{min} = \frac{1-\sigma^2}{2}$. At propagation directions $\theta = 0$ and $\theta = \pi/2$ the error has the highest values $\epsilon_{max} = 1 - \frac{\sigma^2}{2}$, while it has a limiting value $\epsilon_{lim} = 0$ for every θ if $\sigma = 1$, on the other hand attempting to the stability of the algorithm due to violation of the CFL condition.

The anisotropy of the phase velocity with the propagation angle is shown in Fig.D.1 a). The anisotropy we have discussed so far can be reduced via the design of a

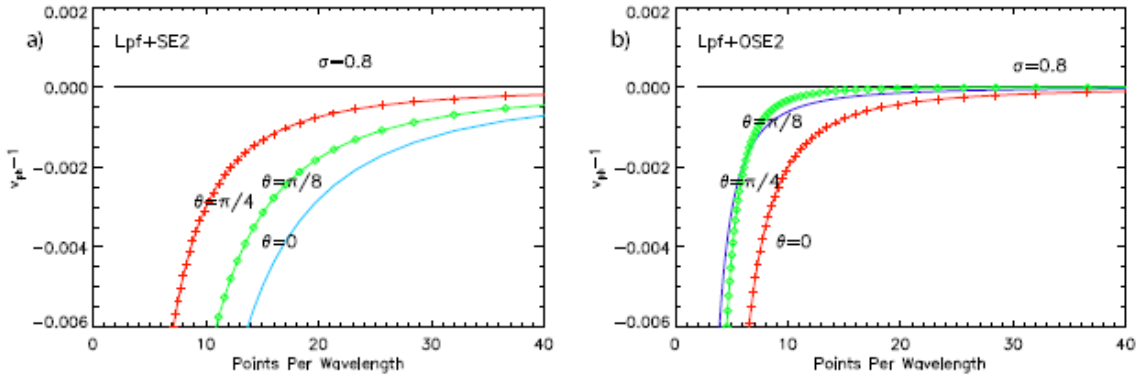


Figure D.1. The phase error in the 2D wave equation as a function on the spatial resolution with a variable angle of propagation θ and Courant number $\sigma = 0.8$. a) the standard leapfrog+2 points finite differences algorithm, b) the optimized+4 points finite differences along x-direction algorithm

scheme with space derivatives along the x-direction (the main propagation direction) discretized with a four-point stencil, while keeping unmodified the other directions.

The first and the second finite difference derivative become:

$$\begin{aligned} [\mathcal{D}_x]_{i+1/2}\psi &= a \left(\frac{\psi_{i+1} - \psi_i}{h} \right) + b \left(\frac{\psi_{i+2} - \psi_{i-1}}{h} \right) = (a + 3b)\psi'_{i+1/2} + \mathcal{O}(h^2), \quad (\text{D.9}) \\ [\mathcal{D}_x^2]_i\psi &= a \left(\frac{\psi_{i+1} - \psi_i}{h^2} - \frac{\psi_i - \psi_{i-1}}{h^2} \right) + b \left(\frac{\psi_{i+2} - \psi_{i-1}}{h^2} - \frac{\psi_{i+1} - \psi_{i-2}}{h^2} \right), \end{aligned} \quad (\text{D.10})$$

where the relation $a + 3b = 1$ holds, so that we can choose one of the two free parameter to reduce the anisotropy of the wave propagation or increase the order of the scheme. For instance, if we take $a = 9/8$ and consequently $b = -1/24$, a formally fourth order scheme is obtained.

The modified numerical dispersion relation leads to Taylor expanded phase velocity:

$$v_\phi^2 = 1 - \frac{1}{12}w^2 \left[g(a) \cos^4 \theta + \sin^4 \theta - \frac{\sigma^2}{2} \right] + \mathcal{O}(w^4), \quad (\text{D.11})$$

where $g(a) = 9 - 8a$ is the free parameter function we use to minimize the $\mathcal{O}(w^2)$ dependence of the phase velocity on the propagation direction. We set $g(a) = \chi\sigma^2$, ad find that:

$$\theta = \frac{\pi}{4} \rightarrow \epsilon = \left(\frac{\chi - 2}{4} \right) \sigma^2, \quad (\text{D.12})$$

$$\theta = \frac{\pi}{8} \rightarrow \epsilon \simeq \left(\frac{1.4\chi - 1}{2} \right) \sigma^2 + 0.02, \quad (\text{D.13})$$

$$\theta = 0 \rightarrow \epsilon = \left(\frac{2\chi - 1}{2} \right) \sigma^2, \quad (\text{D.14})$$

and the best result, as it is shown in Fig.D.1b) is now achieved at the intermediate propagation angle $\theta \simeq \pi/8$.

By considering the constraint $\epsilon > 0$, $\chi < 1/2$ to avoid propagation velocity higher than the speed of light, we find $\chi \sim 0.6 - 0.7$ to be an optimal range of values, when

$\sigma \sim 0.7 - 0.9$ is defined.

We have seen how the discretization of the Maxwell equation with a Yee lattice introduces a numerical error in the phase velocity of the propagating wave, which for a low-resolution grid can be lower than the speed of light. In plasma acceleration either a self-injected or an externally injected beam have relativistic energies such their velocity is close to the speed of light. Due to the numerical error it is therefore possible for a bunch of plasma electrons to overcome the phase velocity of the wave and therefore to excite high frequency modes.

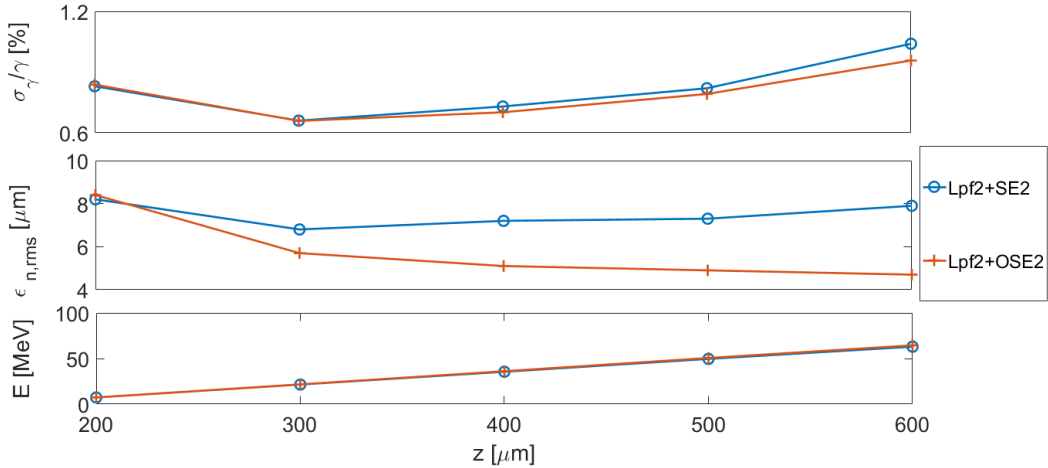


Figure D.2. Evolution of the ionization-injected beam quality over $600 \mu\text{m}$ propagation in $\sim 10^{18} \text{ cm}^{-3}$ plasma density. From top to bottom: energy spread, normalized emittance, transverse sigma. The red curve corresponds to the standard Lpf2+SE2. The blue curve corresponds to the optimized Lpf2+OSE2.

This *numerical Cherenkov radiation* interacts with the beam itself in an unstable process, leading to a general worsening of the beam quality. Several method have been proposed in order to reduce the numerical Cherenkov instability [81], and in Fig.D.2 are shown the results of the optimized algorithm we have presented in this appendix performed with a full 3D PIC simulation with the PIC code ALaDyn.

Since the algorithm focuses on the mitigation of the phase velocity error in the direction of the beam propagation, the energy spread, i.e. the longitudinal phase space, is the parameter which feels the highest change. After $600 \mu\text{m}$ with the optimized algorithm the beam energy spread is almost half than with the standard algorithm. The emittance is ~ 20 percent lower, while the spot size remains unchanged.

Every simulation results we have presented in the main body of the thesis were performed with the optimized algorithm, to reduce at minimum the unphysical effect of the numerical Cherenkov radiation on the beam quality worsening.

Bibliography

- [1] Seeman,J.T. The Stanford Linear Collider, SLAC-PUB 5607, July, 1991.
- [2] The Large Hadron Collider Conceptual Design, CERN/AC/95-05(LHC), October, 1995.
- [3] CLIC $e^+ e^-$ linear collider studies, eds.D.Dannheim et al.,submitted to the update process of the European Strategy of Particle Physics, July, 2012.
- [4] The International Linear Collider, Technical Design Report, Vol. 3 p.II, eds.C.Adolphsen et al., 2013.
- [5] Perl, Martin L. The Superconducting Supercollider project, SLAC-PUB 3493, April, 1986.
- [6] Dawson, John M. "Nonlinear electron oscillations in a cold plasma." Physical Review 113.2 (1959): 383.
- [7] Schlander,F. Study of Quality and Field Limitation of Superconducting 1.3 Ghz 9-Cell RF-Cavities at DESY, PhD. Dissertation, 2012, Hamburg.
- [8] Tajima, T., and J. M. Dawson. "Laser electron accelerator." Physical Review Letters 43.4 (1979): 267.
- [9] Clayton, C. E., et al. "Relativistic plasma-wave excitation by collinear optical mixing." Physical review letters 54.21 (1985): 2343.

- [10] Rosenzweig, James Benjamine, et al. "Experimental observation of plasma wake-field acceleration." *Physical review letters* 61.1 (1988): 98.
- [11] Leemans, Wim P., et al. "GeV electron beams from a centimetre-scale accelerator." *Nature physics* 2.10 (2006): 696-699.
- [12] Blumenfeld, Ian, et al. "Energy doubling of 42 GeV electrons in a metre-scale plasma wake-field accelerator." *Nature* 445.7129 (2007): 741-744.
- [13] Vlasov, Anatoliĭ Aleksandrovich. "The vibrational properties of an electron gas." *Physics-Uspekhi* 10.6 (1968): 721-733.
- [14] Landau, Lev Davidovich. "On the vibrations of the electronic plasma." *Zh. Eksp. Teor. Fiz.* 10 (1946): 25.
- [15] Pucella,G. and Segre, S.E. *Fisica dei Plasmi*, Zanichelli editore SpA, Bologna, 2010.
- [16] Chiuderi, Claudio, and Marco Velli. *Fisica del Plasma: Fondamenti e applicazioni astrofisiche*. Springer Science & Business Media, 2012.
- [17] Shadwick, B. A., et al. "Hamiltonian reductions for modeling relativistic laser-plasma interactions." *Communications in Nonlinear Science and Numerical Simulation* 17.5 (2012): 2153-2160.
- [18] Chen, Pisin, et al. "Acceleration of electrons by the interaction of a bunched electron beam with a plasma." *Physical review letters* 54.7 (1985): 693.
- [19] Ruth, Ronald D., et al. "A plasma wake field accelerator." *Part. Accel.* 17.SLAC-PUB-3374 (1984): 171.
- [20] Bane, Karl LF, Pisin Chen, and P. B. Wilson. On collinear wake field acceleration. No. DOE/ER/40238-1. Stanford Linear Accelerator Center, 1985.

- [21] Katsouleas, S. Wilks T., and JM Dawson JJ Su. "Beam loading efficiency in plasma accelerators." Part. Accel 22 (1987): 81-99.
- [22] BANE, KLF, and PB WILSON. "On Energy Transfer in the Plasma Wake Field Accelerator." (1985).
- [23] Keinigs, Rhon, and Michael E. Jones. "Two-dimensional dynamics of the plasma wake-field accelerator." The Physics of fluids 30.1 (1987): 252-263.
- [24] Ferrario, M. (2011). Accelerator physics: basic principles on beam focusing and transport. Proc. Int. School of Physics ‘Enrico Fermi’, Course CLXXIX, Laser-plasma acceleration, Varenna, 20-25.
- [25] Assmann, R., CERN Accelerator School (2014), lecture
- [26] Barber, S. K. (2015). Plasma Wake-Field Experiments in the Quasi non-linear Regime (Doctoral dissertation, University of California, Los Angeles).
- [27] Kallos, E. (2008). Plasma Wake-Field accelerators using multiple electron bunches. University of Southern California.
- [28] Lu, W., et al. "Limits of linear plasma wake-field theory for electron or positron beams." Physics of Plasmas 12.6 (2005): 063101.
- [29] Kallos, Efthymios, et al. "High-gradient plasma wake-field acceleration with two subpicosecond electron bunches." Physical review letters 100.7 (2008): 074802.
- [30] Boscolo, M., et al. "A train of micro-bunches for PWFA experiments produced by RF photoinjectors." International Journal of Modern Physics B 21.03n04 (2007): 415-421
- [31] Katsouleas, T. "Physical mechanisms in the plasma wake-field accelerator." Physical Review A 33.3 (1986): 2056.

- [32] Power, John Gorham, W. Gai, and A. Kanareykin. "Transformer ratio enhancement using a ramped bunch train in a collinear wake-field accelerator." AIP Conference Proceedings. Vol. 569. No. 1. AIP, 2001.
- [33] Pukhov, Alexancer, and Jürgen Meyer-ter-Vehn. "Laser wake field acceleration: the highly non-linear broken-wave regime." Applied Physics B: Lasers and Optics 74.4 (2002): 355-361.
- [34] Kostyukov, I., A. Pukhov, and S. Kiselev. "Phenomenological theory of laser-plasma interaction in “bubble” regime." Physics of Plasmas 11.11 (2004): 5256-5264.
- [35] Lu, Wei, et al. "Nonlinear theory for relativistic plasma wake-fields in the blowout regime." Physical review letters 96.16 (2006): 165002.
- [36] Lu, W., et al. "A non-linear theory for multidimensional relativistic plasma wave Wake-Fields." Physics of Plasmas 13.5 (2006): 056709.
- [37] Benedetti, Carlo, et al. "ALaDyn: A High-Accuracy PIC Code for the Maxwell–Vlasov Equations." IEEE Transactions on plasma science 36.4 (2008): 1790-1798.
- [38] Londrillo, P., et al. "Charge preserving high order PIC schemes." Nuclear Instruments and Methods in Physics Research Section A: Accelerators, Spectrometers, Detectors and Associated Equipment 620.1 (2010): 28-35.
- [39] Londrillo, P., C. Gatti, and M. Ferrario. "Numerical investigation of beam-driven PWFA in quasi-nonlinear regime." Nuclear Instruments and Methods in Physics Research Section A: Accelerators, Spectrometers, Detectors and Associated Equipment 740 (2014): 236-241.

- [40] Macchi, A., et al. "Advanced strategies for ion acceleration using high-power lasers." *Plasma Physics and Controlled Fusion* 55.12 (2013): 124020.
- [41] Tzoufras, Michail, et al. "Beam loading in the nonlinear regime of plasma-based acceleration." *Physical review letters* 101.14 (2008): 145002.
- [42] Yi, S. A., et al. "Analytic model of electromagnetic fields around a plasma bubble in the blow-out regime." *Physics of Plasmas* 20.1 (2013): 013108.
- [43] Lotov, K. V. "Blowout regimes of plasma wake-field acceleration." *Physical Review E* 69.4 (2004): 046405.
- [44] Golovanov, A. A., et al. "Analytic model for electromagnetic fields in the bubble regime of plasma wake-field in non-uniform plasmas." *Physics of Plasmas* 24.10 (2017): 103104.
- [45] Noble,R.J. Plasma Wave generation in the Beat-Wave Accelerator, SLAC-PUB-3463, November, 1984.
- [46] Rosenzweig,J.B. non-linear Plasma Dynamics in the Plasma Wake-Field Accelerator, *Phys. Rev. Lett.* A44, no.10, 1987.
- [47] Akhiezer, Aleksander Ilyich, and R. V. Polovin. "Theory of wave motion of an electron plasma." *Soviet Phys. JETP* 3 (1956).
- [48] Williams, R. L., et al. "Studies of relativistic wave-particle interactions in plasma-based collective accelerators." *Laser and Particle Beams* 8.3 (1990): 427-449.
- [49] Mora, Patrick, and Thomas M. Antonsen, Jr. "Kinetic modeling of intense, short laser pulses propagating in tenuous plasmas." *Physics of Plasmas* 4.1 (1997): 217-229.

- [50] Lu, Wei. "Nonlinear plasma wake-field theory and optimum scaling for laser wake-field acceleration in the blowout regime." (2006).
- [51] Esarey, Eric, and Mark Pilhoff. "Trapping and acceleration in nonlinear plasma waves." Physics of Plasmas 2.5 (1995): 1432-1436.
- [52] Kostyukov, I. Yu, et al. "Hamiltonian model for plasma electron trapping and acceleration in multidimensional plasma wake field." AIP Conference Proceedings. Vol. 1228. No. 1. AIP, 2010. p. 359-369.
- [53] Kostyukov, I., et al. "Electron self-injection in multidimensional relativistic-plasma wake fields." Physical review letters 103.17 (2009): 175003.
- [54] Oz, E., et al. "Ionization-induced electron trapping in ultrarelativistic plasma wakes." Physical review letters 98.8 (2007): 084801.
- [55] de la Ossa, A. Martinez, et al. "Optimizing density down-ramp injection for beam-driven plasma wakefield accelerators." Physical Review Accelerators and Beams 20.9 (2017): 091301.
- [56] Pukhov, Alexander. "Particle-in-cell codes for plasma-based particle acceleration." arXiv preprint arXiv:1510.01071 (2015).
- [57] Birdsall,C.K. and Langdon,A.B. Plasma Physics via computer simulation, Taylor and Francis, 1985.
- [58] Hockney, Roger W., and James W. Eastwood. Computer simulation using particles. crc Press, 1988.
- [59] Klimontovich, Iu I. "Kinetic theory of nonideal gas and nonideal plasma." Moscow Izdatel Nauka (1975).

- [60] Lapenta,G. Particle In Cell Method, A brief description of the PIC Method, online available lectures.
- [61] Dawson, John M. "Particle simulation of plasmas." *Reviews of modern physics* 55.2 (1983): 403.
- [62] Villasenor, John, and Oscar Buneman. "Rigorous charge conservation for local electromagnetic field solvers." *Computer Physics Communications* 69.2-3 (1992): 306-316.
- [63] Yee, Kane S., and Jei S. Chen. "The finite-difference time-domain (FDTD) and the finite-volume time-domain (FVTD) methods in solving Maxwell's equations." *IEEE Transactions on Antennas and Propagation* 45.3 (1997): 354-363.
- [64] Boris, J. P., & Shanny, R. A. (1971). Proceedings of the Conference on the Numerical Simulation of Plasmas (4th) Held at the Naval Research Laboratory, Washington, DC on 2, 3 November 1970. NAVAL RESEARCH LAB WASHINGTON DC.
- [65] Esirkepov, T. Zh. "Exact charge conservation scheme for particle-in-cell simulation with an arbitrary form-factor." *Computer Physics Communications* 135.2 (2001): 144-153.
- [66] Ammosov, M. V., Nikolai B. Delone, and Vladimir P. Krainov. "Tunnelling ionization of complex atoms and of atomic ions in an alternating electromagnetic field." *Journal of Experimental and Theoretical Physics* 64.6 (1986): 1191-1194.
- [67] Augst, Steeve, et al. "Laser ionization of noble gases by Coulomb-barrier suppression." *JOSA B* 8.4 (1991): 858-867.

- [68] Krainov, Vladimir P. "Ionization rates and energy and angular distributions at the barrier-suppression ionization of complex atoms and atomic ions." *JOSA B* 14.2 (1997): 425-431.
- [69] de la Ossa, A. Martinez, et al. "High-quality electron beams from beam-driven plasma accelerators by Wakefield-induced ionization injection." *Physical review letters* 111.24 (2013): 245003.
- [70] de la Ossa, A. Martinez, et al. "High-quality electron beams from field-induced ionization injection in the strong blow-out regime of beam-driven plasma accelerators." *Nuclear Instruments and Methods in Physics Research Section A: Accelerators, Spectrometers, Detectors and Associated Equipment* 740 (2014): 231-235.
- [71] Martinez de la Ossa, Alberto, et al. "Wakefield-induced ionization injection in beam-driven plasma accelerators." *Physics of plasmas* 22.9 (2015): 093107.
- [72] Bauer, D., and P. Mulser. "Exact field ionization rates in the barrier-suppression regime from numerical time-dependent Schrödinger-equation calculations." *Physical Review A* 59.1 (1999): 569.
- [73] Garten, M. (2013). Comparing field ionization models in simulations of laser-matter interaction (Doctoral dissertation, Ph. D. thesis, TU Dresden).
- [74] Bruhwiler, David L., et al. "Particle-in-cell simulations of tunneling ionization effects in plasma-based accelerators." *Physics of Plasmas* 10.5 (2003): 2022-2030.
- [75] Kirby, Neil, et al. "Transverse emittance and current of multi-GeV trapped electrons in a plasma wakefield accelerator." *Physical Review Special Topics-Accelerators and Beams* 12.5 (2009): 051302.

- [76] Thomas, Alexander George Roy. "Scalings for radiation from plasma bubbles." *Physics of Plasmas* 17.5 (2010): 056708.
- [77] Ju, J. (2013). Electron acceleration and betatron radiation driven by laser Wake-Field inside dielectric capillary tubes (Doctoral dissertation, Université Paris Sud-Paris XI).
- [78] Glinec, Y. (2006). Propagation d'une impulsion laser ultra-intense dans un plasma sous-dense: Génération de faisceaux d'électrons quasi-monoénergétiques et développement d'applications (Doctoral dissertation, Ecole Polytechnique X).
- [80] Thaury, Cédric, et al. "Shock assisted ionization injection in laser-plasma accelerators." *Scientific reports* 5 (2015).
- [81] Lehe, R., et al. "Numerical growth of emittance in simulations of laser-wakefield acceleration." *Physical Review Special Topics-Accelerators and Beams* 16.2 (2013): 021301.
- [82] Lehe, Remi, et al. "Elimination of numerical Cherenkov instability in flowing-plasma particle-in-cell simulations by using Galilean coordinates." *Physical Review E* 94.5 (2016): 053305.
- [83] Godfrey, Brendan B. "Numerical Cherenkov instabilities in electromagnetic particle codes." *Journal of Computational Physics* 15.4 (1974): 504-521.
- [84] Jackson, John David. "Classical electrodynamics." (1999): 841-842.
- [85] Sahai, A. A. (2015). Phase-mixing self-injection into plasma-Wake-Field acceleration structures driven in a rising density gradient (Doctoral dissertation, Indiana University).